AD-A273 731

AFIT/GAE/ENY/93D-6

DTIC
S ELECTE
DEC 16 1993
A

INVESTIGATION OF TENSION-COMPRESSION FATIGUE
BEHAVIOR OF A CROSS-PLY METAL MATRIX
COMPOSITE AT ROOM AND ELEVATED TEMPERATURES

THESIS

Elizabeth A. Boyum
Captain, USAF

AFIT/GAE/ENY/93D-6

93-30429

AFIT/GAE/ENY/93D-6

INVESTIGATION OF TENSION-COMPRESSION FATIGUE BEHAVIOR OF A CROSS-PLY METAL MATRIX COMPOSITE AT ROOM AND ELEVATED TEMPERATURES

THESIS

Presented to the Faculty of the Graduate School of Engineering

of the Air Force Institute of Technology

Air University

In Partial Fulfillment of the

Requirements for the Degree of

Master of Science in Aeronautical Engineering

Elizabeth A. Boyum, B.S.E.M.

Captain, USAF

December 1993

Accesion For

NTIS CRA&I		✓
DTIC TAB		
Unannou ced		
Justification		

By ....
Distribution /

Availability Codes

Dist	Avail and/or Special
A-1	

Table of Contents

List of Figures

List of Tables

Abstract

The apparent lack of techniques for performing tension-compression fatigue of MMCs has resulted in a significant gap in the full characterization of the damage mechanisms associated with this promising new class of engineering materials. This research, the first load-controlled fully-reversed fatigue testing to be performed on a MMC, seeks to extend the existing knowledge of fatigue damage mechanisms to include the tension-compression loading condition required for full characterization of the MMC damage mechanisms. To accomplish this, the deformation mechanisms in a $[0/90]_{2s}$ SCS-6/Ti-15-3 metal matrix composite were investigated under tension-tension fatigue at room temperature, and tension-compression fatigue at both room temperature and 427°C. Stress and strain data was taken to evaluate the macro-mechanic behavior of the material. Additionally, microscopy and fractography were performed to characterize the damage on a r...ro-mechanic level.

Several milestones were overcome just to perform the tension-compression fatigue tests, and thus are significant contributions to the future of tension-compression testing. First, a dogbone specimen was designed with a 58 percent area reduction in the gage length and consistently produced the desired gage length failures. Additionally, a buckling guide was designed for use in the tension-compression fatigue tests which successfully prevented excessive specimen buckling while also allowing the specimen to strain in an unrestricted manner. Although several buckling guide designs have been used successfully in monotonic testing, the AFIT buckling Guide is the first of its type to be used in fatigue testing.

On a maximum applied stress basis, the room temperature tension-tension specimens had longer fatigue lives than the room temperature tension-compression specimens. The room and high temperature tension-compression fatigue lives were nearly

identical in the fiber-dominated high stress region of the SN curve. However, the increased ductility and diffused plasticity of the titanium matrix at 427°C delayed the onset and severity of matrix cracking, and thus increased the fatigue lives in the matrix dominated region of the SN curve. In all cases, matrix damage initiated at reaction zone cracks which nucleated both matrix plasticity and matrix cracking.

INVESTIGATION OF TENSION-COMPRESSION FATIGUE BEHAVIOR OF A CROSS-PLY METAL MATRIX COMPOSITE AT ROOM AND ELEVATED TEMPERATURES

I. Introduction

The performance requirements of the next generation of aircraft demand materials that are lightweight and have high stiffness and strength characteristics at the elevated temperatures to which they will be subjected. The monotonic metals that have been used for these applications in the past do not meet these increased strength and stiffness requirements. However, Metal Matrix Composites (MMCs), metal alloys reinforced with high strength and stiffness fibers, have been found to meet these requirements.

MMCs have the advantages of high strength, elastic modulus, toughness and impact properties. They have a low sensitivity to temperature changes and thermal shock, and have shown a high surface durability and sensitivity to surface flaws (50:3). These advantages make them attractive for use in the demanding environments mentioned above. One particular MMC, a titanium alloy matrix reinforced with silicon carbide fibers (SCS-6/Ti-15-3) is a good model for these applications. This MMC system is analyzed in the current research.

However, before structures can be designed using MMCs, their deformation and failure mechanisms in the environments to which they will be subjected must be fully characterized. Although a significant amount of research has been conducted for this material in monotonic tension and compression loading (25, 28, 29, 37), and a smaller amount on the tension-tension fatigue loading (21, 34), there is an extreme lack of research in the area of tension-compression fatigue loading. The reason for this lack of

research is that most MMCs are fabricated in thin sheets, the form most likely to be used in aircraft applications. These thin composites, when placed under compressive loading, are susceptible to premature failure due to buckling. Thus, to perform compressive fatigue testing on this material, some type of guide is needed which prevents the specimen from buckling, but which does not impart additional strength to the specimen. Although several guides of this type have been reported for use in static loading (29:49), none exist for use in the fatigue loading case.

This lack of testing techniques has resulted in a severe lack of information about the behavior of MMCs in a loading condition of great practical importance. For example, the wing skins of aircraft, due to the bending of the wing, are subjected to tension-compression fatigue, the leading edges of which can experience very high temperatures. Components of the wing have also been known to undergo tension-compression fatigue. Rich, Pinkert, and Christian reported that the wing upper spar cap of the F-15 fighter aircraft developed fatigue cracks during flight due to tension-compression loading (19:243). Additionally, most published metals fatigue data is based on fully-reversed loading (6:9). Thus, it is necessary to obtain the same type of fatigue data for MMCs. This is the focus of this study.

This research investigates the behavior of the $[0/90]_{2s}$ cross-ply laminate of SCS-6/Ti-15-3 MMC in tension-compression fatigue loading at both room temperature and an isothermal elevated temperature of 427° C. To accomplish this, fatigue tests were performed under three loading conditions: tension-compression at room temperature (TC RT), tension-compression at 427° C (TC HT), and tension-tension at room temperature (TT RT). The TT RT tests enabled conclusions to be made on the effects of tension-compression fatigue based on comparisons between the TC RT and TT RT loading conditions. All fatigue tests were performed in load control at a loading frequency of 10 Hertz (Hz), which is common in the literature. The tension-tension tests had a load

ratio, R, of 0.1, while the tension-compression tests had a load ratio of -1. These load-time relationships are shown in Figs. 1 and 2.

As previously mentioned, premature failure due to buckling is a concern when conducting compression testing. For this reason, an Euler buckling analysis (Appendix A) was performed to determine the buckling length of various length specimens. A 2.54 cm (1 in.) gage length specimen length was chosen, which was two to six times less than the Euler buckling critical lengths for the stress levels required during testing. No buckling
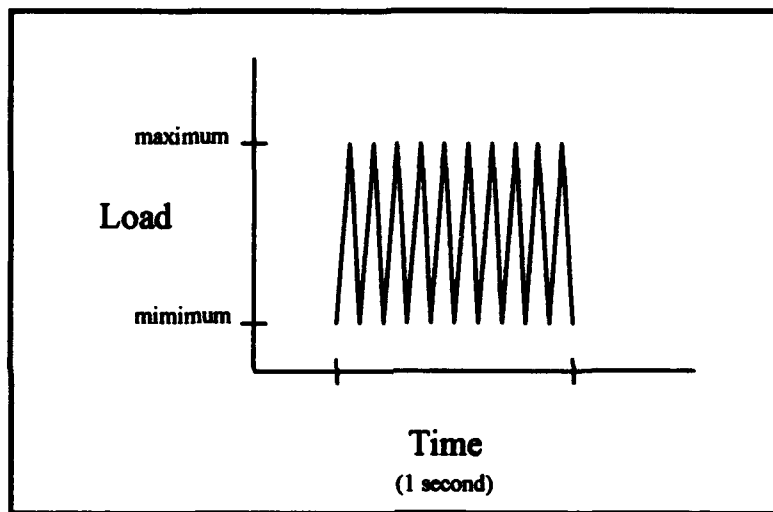
Figure 1. Tension-Tension Load-Time Relationship, R = 0.1
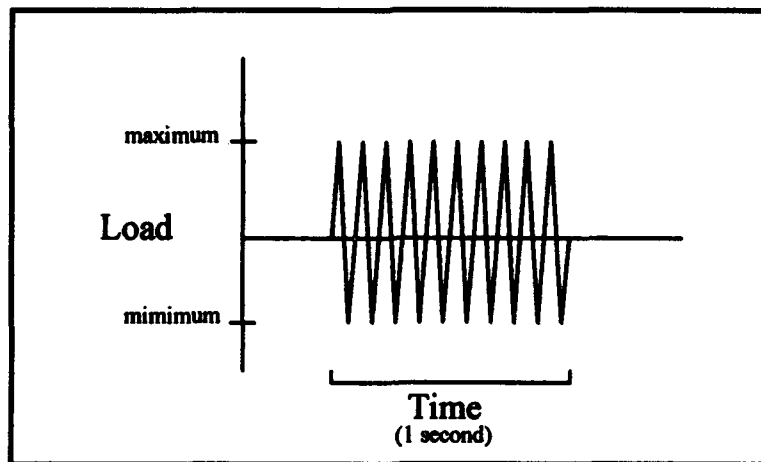
Figure 2. Tension-Compression Load-Time Relationship, R = -1

was observed during all tests in this study when this gage length was employed at room temperature.

This 2.54 cm gage length, however, did not provide sufficient room between the test stand load transducer and cross-head for the quartz heat lamps which were needed to heat the specimens for the elevated temperature tests. Thus, a heat nozzle attachment was designed which funneled the radiant heat down to a 1.905 cm (3/4 in.) outlet, which required a nominal specimen gage length increase to 4.125 cm (1 5/8 in.). Initial elevated temperature tests revealed that, although the static strength and modulus of the material decreased at 427° C, the tension-compression fatigue life actually increased. Additionally, the two TC HT specimens which were tested using the heat nozzles failed outside the heat zone. Microscopic evaluation revealed that within the very localized heat zone (Fig. 3) caused by the nozzles, no matrix cracking existed. However, matrix cracking began just outside the heat zone, and became worse with increased distance. It was within these highly cracked regions of the specimen that the first two failures occurred. It was evident that the increased temperature caused the matrix to become more ductile, drastically reducing the matrix damage which at some stress levels dominated specimen failure.
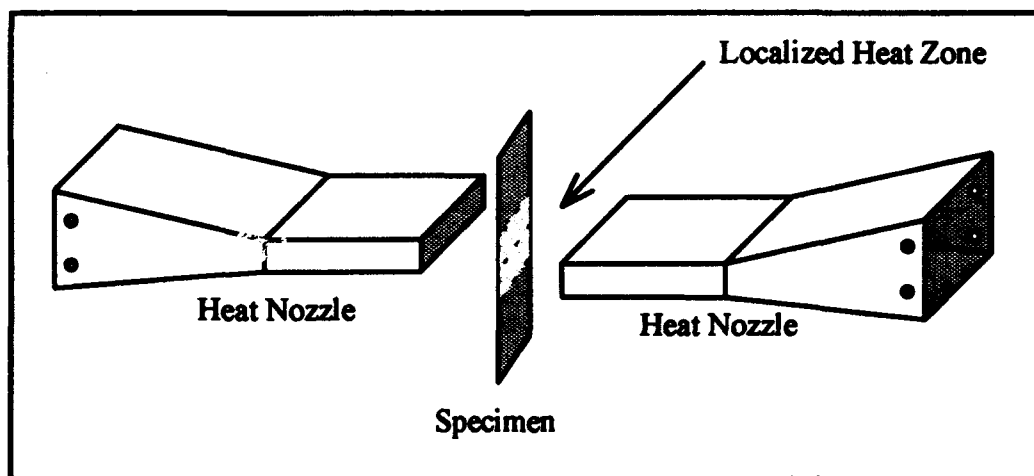
Figure 3. Localized Heat Zone on Specimen

The inability of the heat nozzles to heat the entire specimen caused a thermal gradient on the specimen which caused failure outside the region of interest. Thus, the next logical step was to heat the entire specimen, in which the thermal gradient would be eliminated, and the specimen failure would then characterize that of the elevated temperature. However, the equipment needed for this type of a test was not available. Thus, a less localized heat zone was needed which would heat as much of the specimen as possible. To accommodate the full vertical length of the heat lamps which would provide this extended heat zone, the test stand grips had to be further apart. This required a much longer specimen, which would surely buckle under the compressive loads.

To avoid premature specimen failure due to both the matrix cracking caused by the temperature gradient and the buckling caused by the required increased gage length, a new specimen geometry and buckling guide were developed. A dogbone specimen geometry was designed with the expectation that a reduced area in the heated gage length would induce the failure to occur there. Since it was not known how much stronger the material was at elevated temperature, a drastic area reduction was desired to ensure heat zone failure. The heat lamps were then used without nozzles, increasing the heat zone area, which further increased the possibility for failure in the gage section. Thus, the dogbone design was selected with a 58 percent width reduction in the center gage length. This design involved tradeoffs between maximum width reduction and maximum radius of curvature at the shoulder of the dogbone, since small shoulder radii could cause failure due to the localized high shear stress (53:1). A unique buckling guide was also designed for specific use in fatigue loading with the dogbone specimens. Use of the dogbone specimens in conjunction with the buckling guide was successful, resulting in consistent heat zone failures. Additionally, the buckling guide was used at room temperature to validate the fact that buckling did not occur during the TC RT tests which were performed without a buckling guide. The fatigue lives for these tests with and without the buckling

5

guide were in agreement, indicating that buckling did not cause failure in the TC RT tests. Both the dogbone specimen and buckling guide designs are discussed in more detail in Chapter 3.

Six specimens were tested at five different stress levels in tension-compression at room temperature, and seven specimens at four different load levels in tension-compression at 427° C. Five specimens were tested at five different load levels in tension-tension at room temperature. During testing, damage progression was monitored via the acetate edge replica. This technique allowed for a physical record to be taken of the specimen edge at various cycle counts. Replicas were taken either at a minimum of once a logarithmic decade, or any time when significant damage was suspected due to an increase in strain or a decrease in specimen stiffness.

Following testing, microscopic evaluation of the edge replicas, the specimen edge, and the fracture surface provided insight into the nature and cause of the failure. Selected specimens were sectioned to determine the deformation mechanisms active within the specimen. These sectioned specimens were also chemically etched, which enabled observation of plastic deformation. This analysis, coupled with the stiffness and strain data taken during the fatigue test, aided in the understanding of the deformation mechanisms of the MMC at each stress leve. Conclusions were then made on the dominant deformation mechanisms for each loading case and for each stress level within a loading case. The applied stress (S) and fatigue life (N) curves were developed for all three loading cases. The following chapters provide the details of this study.

II. Previous Works

Introduction

The previous works which are pertinent to the current research include monotonic loading in tension and compression, tension-tension and tension-compression fatigue, all at both room and elevated temperatures. A brief background of these previous studies is presented here, divided into room temperature testing and elevated temperature testing portions, each with an emphasis on the response and damage mechanisms which characterize the material in the different loading conditions. This is done in an effort to correlate the current research to that of previous works when applicable.

Room Temperature Testing

Majumdar and Newaz investigated the inelastic tensile deformation of both $[0]_8$ and $[90]_8$ laminates of SCS-6/Ti-15-3, MMC (28:1-65). The 0.34 fiber volume laminates were consolidated at a temperature of 815° C and were not subsequently heat treated. Testing consisted of load controlled monotonic tension tests to failure. An in-depth examination of the deformation mechanisms revealed that the inelastic deformation of MMCs can be separated into two types: damage and plasticity. Damage consists of fiber and matrix cracking, fiber-matrix reaction zone cracking, and debonding at the fiber-matrix interface. Plasticity occurs in the matrix and includes slip band formation and changed dislocation densities.

Deformation was then broken down into a three stage deformation behavior. The first stage consists of the fully elastic response of the laminate. The second stage, however, is damage dominated, characterized by fiber-matrix debonding, reaction-zone cracks, and micro-yielding of the matrix. Stage III is characterized by plasticity, largely

concentrated in intense shear bands between the fibers which lead to shear crack initiation and finally, fracture.

Micro-mechanic investigation resulted in a characterization of the damage mechanisms for each of the laminates tested. Nonlinear deformation began in the 0° laminate at a strain of approximately 0.55 percent, and was caused primarily by matrix plasticity. Deformation in the 90° laminate began at approximately 0.4 percent and included fiber-matrix debonding, matrix cracking, reaction zone cracking, and matrix plasticity.

Plasticity was found to nucleate in the small region surrounding the fibers, where the effective residual stress is slightly less than the yield stress of the matrix, thus making it more susceptible to deformation. Plasticity was observed in the form of concentrated slip bands, which generally began at reaction zone cracks in both the 0° and 90° fiber-matrix interface. Two basic types of slip bands were detected: triangle slip bands which occur first, followed by intense shear bands which zigzag between alternate fibers in adjacent plies. In the 90° laminate, final fracture occurred along the latter.

Majumdar and Newaz also investigated the inelastic compressive deformation and the fatigue response of SCS-6/Ti-15-3 at room temperature (29:1-17). Their research was focused on determining how cracks initiate in regime II (the fatigue life stage which follows the high-stress low-life regime) of Talreja's Concept of Fatigue Life (49), on whether the persistent slip bands which precede failure in monolithic metals exist also in MMCs, and on determining the role of reaction zone cracks under compressive loading.

Compression tests of the 0° specimens revealed that, although the elastic modulus was identical in tension and compression, the onset of inelastic deformation occurs at a higher stress magnitude in compression than in tension. This is due to the residual tensile stress which exists in the fiber from initial fabrication. Extensive slip band activity was

observed, and there was a virtual absence of the reaction zone cracks which occurred so frequently in the previous tension tests.

The compression tests of the 90° specimens resulted in a two stage deformation response. This did not include the longitudinal fiber-matrix debond stage found in the monotonic tension tests Transverse debonding, however, did occur at very high strain levels. Reaction zone cracks were found on the top and bottom of the fibers (along the load line), in comparison to the sides of the fibers where they were found in tension.

Fatigue tests were performed in load-control tension-tension with a stress ratio, R, of 0.1. Specimens were of varying fiber volume, ranging from 0.15 to 0.45, and had a dogbone geometry with a shoulder radius of 355.6 mm. The fatigue life results of all fiber volume fraction specimens fell together, indicating that just as the fatigue life of monolithic metals is strain-range controlled through inelastic plastic deformation, so is the fatigue life of the 0° laminate. The formation of channel type dislocation structures were observed in the fatigued composite. These dislocation structures, which are characteristic of persistent slip bands (PSBs) in body centered cubic metals, indicate that classical fatigue mechanisms operate in the matrix of the fatigued MMC (29:49). Thus, the authors concluded that regime II fatigue life is dominated by matrix fatigue.

The fatigue cracks were observed to nucleate in several different ways. Some cracks initiated at cracked fibers, most of which were cracked in the as fabricated condition. A more prevalent nucleation site for fatigue cracks, however, was the reaction zone crack. Most of the cracks grew along crystallographic planes, and tended to propagate along slip bands. Cracks also initiated at Molybdenum weave sites when the strain-range was above 0.3 percent.

Fiber-matrix debonding was found to be negligible under monotonic loading (28), however, it existed under the fatigue loading condition. Most debonds initiated at

9

reaction zone cracks and grew under continued fatigue cycles. The authors theorized that the matrix plasticity ahead of an approaching matrix crack can cause these reaction zone cracks.

Johnson also investigated tension-tension fatigue of SCS-6/Ti-15-3 at room temperature (21). The fatigue tests were conducted under load control with a stress ratio of 0.1. Specimens of various lay-ups, including $[0/90]_{2s}$ were tested. Failure modes of the MMC were found to be either matrix dominated, fiber dominated, due to self-similar damage growth, or due to fiber-matrix interfacial failures. Maximum stresses ranging from 500 to 800 MPa resulted in specimen fatigue lives ranging from approximately 40,000 to 5,000 cycles. Johnson noted that since the titanium matrix is so strong, it is capable of creating a very large stress concentration in a fiber ahead of a matrix crack.

Johnson, Lubowinski, and Highsmith (22) later continued the above work, with the exception that the specimens were heat treated for sixteen hours at 482° C. The fatigue tests were performed in load control at a frequency of 10 Hz. They found that the heat treatment increased the yield strength, ultimate strength, and stiffness of the matrix. They also found that a chemical reaction occurs between the fiber and the matrix. This results in a "...somewhat thick, brittle reaction zone, most likely made up of titanium carbides and titanium silicates, formed during composite fabrication" (22:210). Cracks in this brittle reaction zone were found to nucleate matrix plasticity and cracks.

Lerch investigated matrix plasticity in SiC/Ti-15-3 composites subjected to monotonic tension loads at room temperature (25). He presented an experimental method for revealing matrix plasticity in the form of slip bands. Specimens were post heat treated for 24 hours at 427° C, then etched with a 3 percent aqueous solution of ammonium bifluoride etchant. This heat treatment causes the alpha phase particles of the matrix to

precipitate along grain boundaries and slip bands. The chemical etchant attacks these alpha particles, thus revealing the slip bands which resulted from the tensile loading.

The heaviest concentrations of slip bands occurred in areas of high stress and strain. These areas included the tips of the matrix cracks and the areas around both the 0° and 90° fibers, near the fiber-matrix interface. Lerch concluded that slip bands will be observed once the local stress is larger than the yield strength of the matrix (25:3), and that matrix flow can occur before fiber-matrix debonding occurs.

Elevated Temperature Testing

Newaz and Majumdar investigated the mechanical response of SCS-6/Ti-15-3 at both room and elevated temperatures (37). Their goal was "...to develop a comprehensive rationale explaining the response of these composites in relation to the actual deformation mechanisms..." (37:2). This was to be done at room temperature, 538° C, and 650 ° C. Monotonic tension tests were performed on various non-heat treated $[0]_8$, $[90]_8$, $[\pm 45]_{2s}$, and $[0/90]_{2s}$ laminates.

At elevated temperatures, the $[0]_8$ laminate deformation characteristics remained the same. Although the yield strength and strain decreased, and the onset of non-linearity occurred earlier at the higher temperatures, matrix plasticity remained as the primary deformation mechanism. The $[90]_8$ laminate exhibited a three stage behavior at 538° C, as was seen at room temperature. However, the knee in the stress strain curve which separates stage I from stage II is not evident at 650° C. This is attributed to the increased temperature totally relieving the compressive residual stress which exists around the fibers due to initial processing. Thus, debonding initiates soon after the load is applied, thus producing no knee in the data. At both temperatures, the matrix was observed to have enhanced ductility and a lower flow stress.

A micro-structural analysis showed that the $[0]_8$ laminate inelastic deformation is dominated by slip band formation/matrix plasticity both at room and elevated temperatures. The reaction zone cracks form prior to plasticity, and play a major role in nucleating plasticity in the matrix. This plasticity is characterized by diffused slip at elevated temperatures versus the more planar slip observed at room temperature.

At room and elevated temperatures, the $[90]_8$ laminate inelastic deformation is dominated by both damage and plasticity, in the form of fiber-matrix debonding and slip band formation in the matrix, respectively. However, the elevated temperature plasticity was, as in the $[0]_8$ laminate, more diffused than planar. The $[0/90]_{2s}$ laminate resulted in a combination of the above deformation characteristics.

Pollock and Johnson investigated the characterization of unnotched SCS-6/Ti-15-3 at 650° C. This temperature was chosen because it is the highest expected operating temperature for this material system, and because the matrix exhibited a time-dependent deformation at this temperature. The authors performed thermal creep tests to determine at what temperature the matrix deformation begins to become time dependent. At 480° C, this time-dependency was not observed as it was at 650° C. Specimens of various ply orientations were loaded in both monotonic tension and in fatigue.

The monotonic tension tests at room temperature showed that the elastic modulus was 15 to 22 percent lower than at room temperature. Additionally, the strengths and strain to failure were lower for all the lay-ups. Since the fiber strength is not effected by temperatures below 1100° C, these reductions were due to changes in the matrix. A major difference between the room and elevated temperature monotonic tension response is that the knee in the stress strain curve was not seen at elevated temperatures.

The cyclic response of the laminates revealed that the higher the number of 0° plies, the more fatigue resistant the material. For all laminates, at the higher stress levels (and hence, shorter fatigue lives), damage was initiated in the fiber. However, for the lower

12

stress levels, the damage initiated in the matrix. Pollock and Johnson also tested the unreinforced matrix and found that the intersection of the laminate and matrix SN curves indicates the point at which fatigue failures are fiber dominated or matrix dominated.

The microscopic evaluation revealed that at elevated temperatures, under both monotonic loading and fatigue loading, the unreiforced matrix material undergoes a ductile fracture. This fracture is characterized by matrix necking which created a ridge at the failure surface. This ridge was dimpled, which further indicates the ductile fracture.

The failure surfaces of the composite also reflected the ductile failure. Ductile void coalescence formed around the ends of broken fibers at elevated temperatures. The matrix necked between the fibers, causing the matrix to pull away from the fibers, thus forming ridges. Dimples on the fracture surface also indicated ductile failure.

In general, the fracture surfaces of the fatigued specimens showed similar regions as found in the monotonically loaded specimens. For laminates with off-axis plies, damage initiated with interfacial failure between matrix and fibers. The amount of matrix cracking was found to be dependent upon the applied stress range. For higher applied stresses, less matrix cracking was found than in the specimens subjected to lower stresses.

Mall and Portner (34) investigated tension-tension fatigue behavior in a cross-ply laminate of SCS-6/Ti-15-3 Metal Matrix Composite at 427° C. The fatigue tests were load controlled with a stress ratio (R) of 0.1. Tests were performed at both 0.2 and 2 Hz. The goal of this research was to examine the initiation and progression of damage in the material at high temperature. A $[0/90]_{2s}$ laminate with a volume fraction of 0.38 was used. The damage progression was monitored by use of the acetate replica. Damage was quantified in terms of a damage parameter based on the initial and instantaneous moduli.

The two frequency groups tested resulted in different strains at failure. This indicated that different modes of failure were operative. The specimens tested at high frequency experienced matrix failure before fiber failure. They also experienced a strain

hardening of the matrix, rendering it more brittle. Thus, the specimens were more susceptible to the brittle cleavage fracture which dominated fracture at high frequencies. The specimens tested at low frequency, however, fiber failure preceded matrix failure. The low frequency specimens showed a primary failure mechanism of ductile void coalescence.

At both frequencies, the transverse matrix cracking initiated at the fiber-matrix interfaces for specimens cycled at lower stress levels. At the higher stress levels, however, transverse matrix cracks initiated at cracked fibers. No evidence of ply delamination was found.

As can be noted from the above discussion, a significant amount of research has been conducted for monotonic and tension-tension fatigue of MMCs, SCS-6/Ti-15-3 in particular, and extremely little has been published in the area of tension-compression fatigue. The limited number of studies which are available in this area are conducted under strain controlled tension-compression fatigue; no work has been published for load controlled tension-compression fatigue for SCS-6/Ti-15-3.

Verilli and Gabb (51) of NASA Lewis Research Center researched the high temperature fatigue behavior of a tungsten/copper composite. Fully reversed (R = -1), strain controlled fatigue tests were performed at 260° C and 560° C in an environmental chamber, or vacuum. These tests were compared to previously generated zero-tension fatigue tests with a stress ratio, R = 0.05. Dogbone specimens with a shoulder radius of curvature of 368.3 mm and 63.5 mm were used for the fully-reversed and zero-tension tests, respectively. The larger radius of curvature for the fully-reversed tests was used to prevent the likelihood of buckling and of failure at the specimen shoulders. The specimens were not tested to failure into two pieces, but a failure criterion of a 25 percent in reduction of tensile stress from the highest stress experienced during the test was adopted.

14

The material system tested is "ductile/ductile" in nature; both the Tungsten fibers and the Copper matrix are ductile. This results in an extremely strong fiber matrix interface. This is in direct opposition to the "brittle/ductile" nature of the SiC/Ti metal matrix composite system which has a very weak fiber-matrix interface. This difference plays a major role in the fatigue response of the MMC systems.

The authors found that, on a strain range basis, the fatigue life of the tension-tension specimens was two orders of magnitude less than that of the fully-reversed specimens. They concluded that the tensile mean stresses and strains which develop during tension-tension testing are detrimental to the fatigue life of the composite. This theory is well documented for monolithic metals. Fuchs and Banantine independently reported that on a stress range basis, "tensile mean stresses are detrimental to, and compressive mean stresses are beneficial to the fatigue life of a metal" (13:69, 6:17). This is illustrated in Fig. 4.
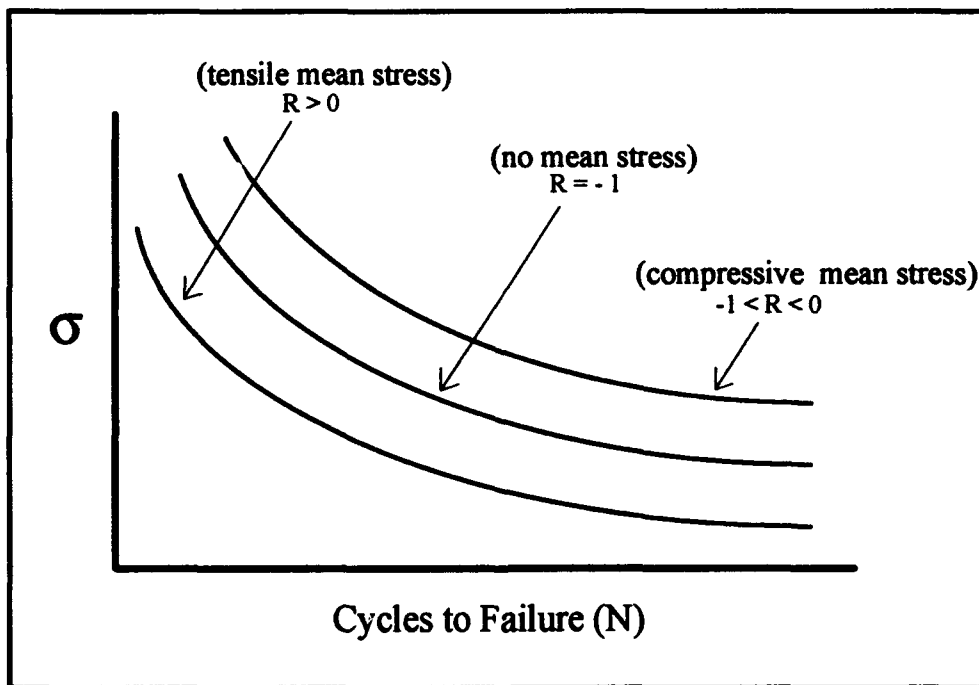
Figure 4. Effect of Mean Stress on Fatigue Life

15

For both the tension-tension and fully-reversed tests, the matrix failed primarily by formation of cavities at grain boundaries. Fiber cracking was never prevalent, and matrix crack bridging occurred. When the matrix cracks grew long enough so that the fibers carried most of the load, the fibers necked up to 70 percent for the tension-tension specimens, but only 1 to 14 percent for the fully-reversed specimens.

Lerch and Halford (26) investigated the fully reversed fatigue response of an SCS-6/Ti-15-3 [±30]$_s$ laminate. The dogbone specimens were heat treated at 700° C for 24 hours in a vacuum and had a shoulder radius of 370 mm. The fully-reversed fatigue tests were performed in strain-control, with a strain rate of 0.001/second. These tests were compared to previously generated load controlled zero-tension, or tension-tension fatigue data with a stress ratio, R, of 0.05. Both sets of tests were performed at an isothermal temperature of 427° C.

The authors found that, on a strain range basis, the fully-reversed fatigue lives were two orders of magnitude longer than the tension-tension fatigue lives. The fully-reversed fatigue lives were orders of magnitude less than that of the unreinforced matrix, while the lives tension-tension specimens were only five times shorter than the unreinforced matrix.

On a stress range basis, the tension-tension fatigue lives were several orders of magnitude shorter than the fully-reversed fatigue lives. The authors attributed this difference to the tensile mean stresses which occur in the tension-tension case. Thus, the Modified Goodman Equation was used to "correct" the delta stress for the tension-tension case to values which are more comparable to the fully-reversed case which has no mean stresses. The corrected delta stresses revealed that the tension-tension fatigue lives were one order of magnitude greater than their uncorrected lives, yet they were still shorter than the fully-reversed fatigue lives. Both tension-tension and fully-reversed fatigue lives were shorter than the unreinforced matrix on a stress range basis.

16

On a maximum stress basis, both fatigue life curves fall together. The maximum stress for the strain controlled fully-reversed case is the peak cyclic stress at half life. In both cases, the fatigue life is less than that of the unreinforced matrix.

Microscopic inspection revealed differences in the damage mechanisms for the tension-tension and fully-reversed cases. The tension-tension specimens were covered with short matrix cracks, less than 1 mm in length. These cracks were primarily matrix cracks which circumvented the fibers and had large crack opening displacements (COD). Extensive fiber-matrix debonding was observed, and the matrix slivers between the fibers occasionally necked. Almost every fiber was cracked.

The fully reversed specimens, however, had long, isolated matrix cracks, approximately 3 mm in length. As in the tension-tension c , the matrix cracks circumvented the fibers, but they had small CODs. Some interfacial debonding occurred, but no necking in the matrix slivers was observed. In contrast to the extensive fiber cracking found in the tension-tension specimens, no fiber cracking was found.

Thus, it is evident that much work has been done in examining and characterizing the behavior of SCS-6/Ti-15-3 under monotonic loading in tension and compression and in tension-tension fatigue loading. However, research is extremely limited in the area of tension-compression fatigue of this, and other, MMCs. No research to date has been reported for load-controlled tension-compression fatigue of SCS-6/Ti-15-3 at room or elevated temperatures. Thus, the current research is necessary to fully characterize the effect of tension-compression fatigue both at room and elevated temperatures.

III. Experimental Set-up and Procedure

Material

The material investigated in this research is SCS-6/Ti-15-3, a continuous fiber reinforced cross ply metal matrix composite (MMC) with an orientation of $[0/90]_{2s}$, a layup capable of sustaining combined loads. Silicon carbide fibers, SCS-6, are embedded in a titanium alloy matrix (Fig. 5). The silicon carbide fibers (Fig. 6) compose 35 percent of the volume of the laminate, or a volume fraction of 0.35. The mean fiber diameter is 142 microns (μm) which is composed of 3 different regions. The inner core of the fiber is a 38.4 μm diameter pure carbon filament. Surrounding this core is a 48.4 μm layer of bulk silicon carbide that is formed on the carbon core through a process of chemical vapor deposition. The remaining 3.5 microns is composed of alternating layers of silicon and carbon, the outermost of which is a carbon rich layer that enhances the surface strength of the fiber and improves the bonding with the surrounding matrix (36). Ti-15-3, a shortened designation for Ti-15V-3Cr-3Al-3Sn, is a new metastable beta strip alloy used where cold formability and high strength are desired (42:1). The alloy was developed primarily for the Air Force with the goal of lowering airframe costs while offering higher performance through improved mechanical properties. By weight, the alloy is composed of 75 percent Titanium, 15 percent Vanadium, 3 percent Aluminum, Chromium, and Tin. An EDAX (Electro-Dispersive Analytical X-ray) analysis was performed on the panel by Baker (4) that confirmed this manufacturer-advertised composition.

Material Preparation

The panel used in this research was fabricated by Textron Specialty Materials Inc., who holds the a patent on the Hot ISO static Pressing (HIP) method used. In this method, the laminate is layed up in the appropriate order and directionality of fiber and matrix.

18

Transverse Section

Longitudinal Section
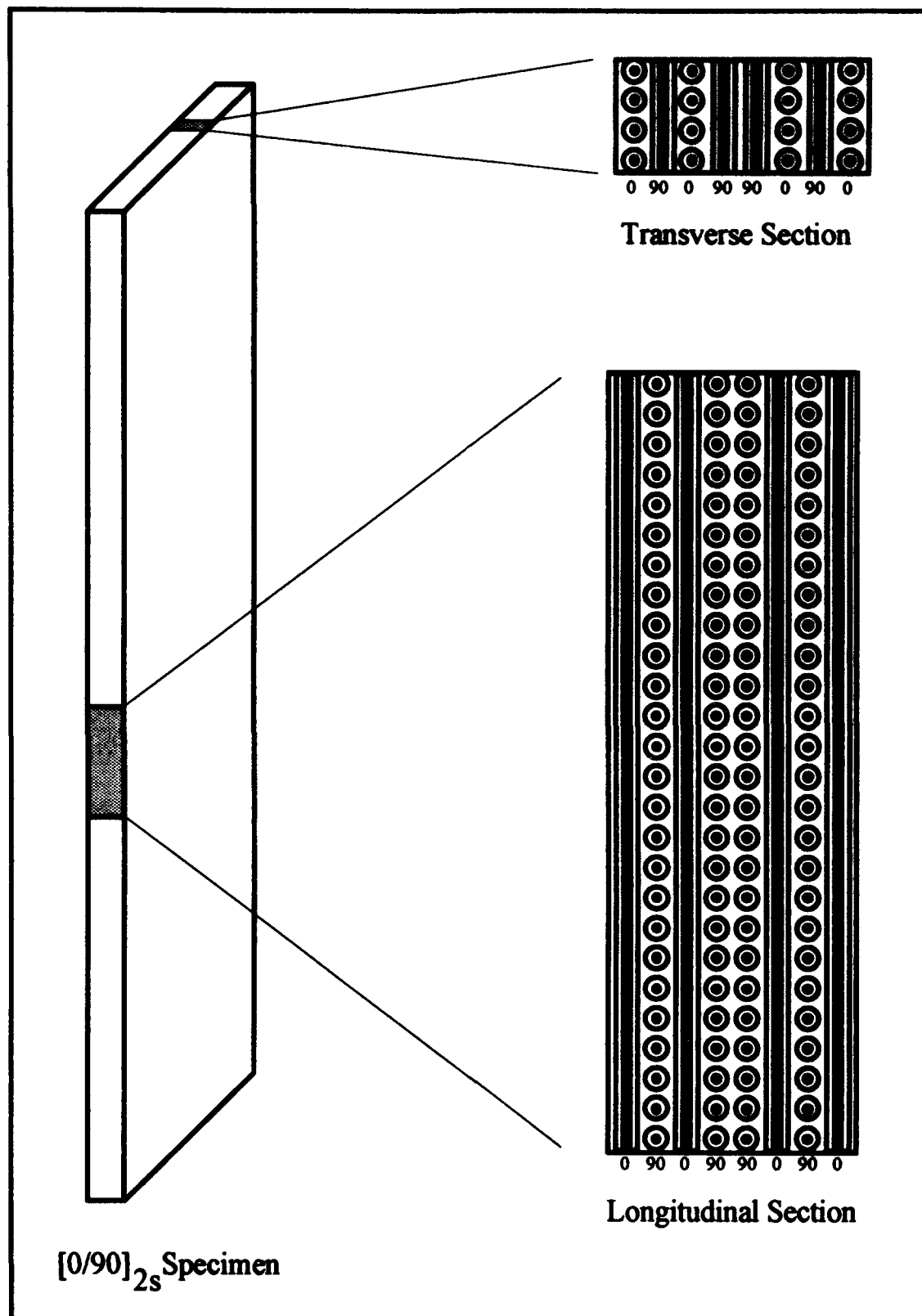
$[0/90]_{2s}$ Specimen

Figure 5. $[0/90]_{2s}$ Specimen and Sections

19
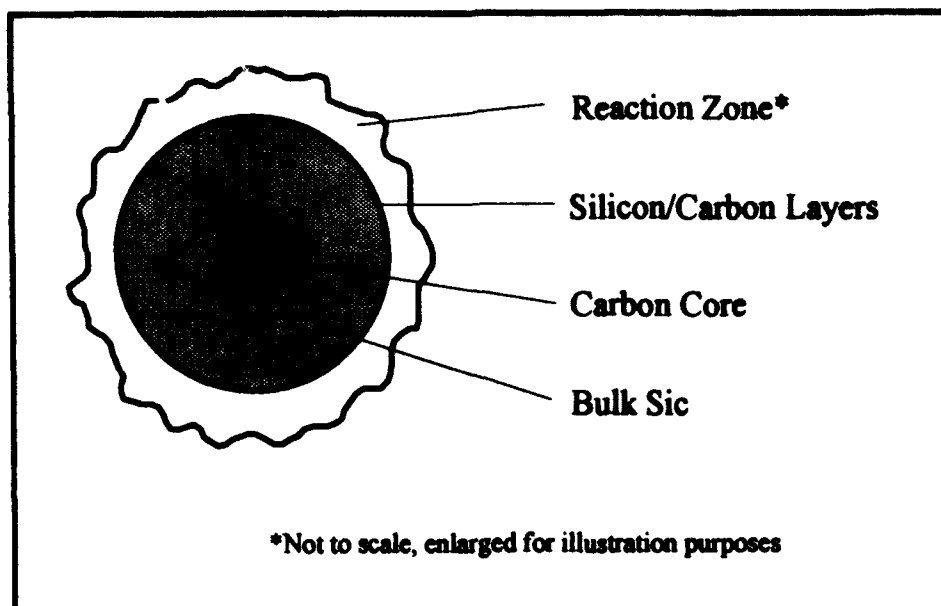
Figure 6. SCS-6 Fiber

The fiber layers are held together with small molybdenum fibers (molly weaves), that are woven through, and perpendicular to the SCS-6 fibers. The matrix layers are thin, cold-rolled sheets of titanium foil, similar to the commercially available aluminum foil. Once the layers are assembled, they are heated to a temperature of approximately 815° C and held at a pressure of 35 MPa. This extreme heat and pressure environment causes the matrix to liquefy and flow into the fiber layers, thus consolidating the layers into one laminate. The HIP process results in a superior consolidation of the fibers and matrix.

Test Apparatus

Both the room and elevated temperature tests were performed on a servo-hydraulic test stand (Material Test System 808) equipped with a 9979.0 kg (22,000 lb) load cell. The fatigue test profile was provided to the test stand from a Zenith 248 computer via a program called LOADTEST, developed by Sanders (44), an AFIT doctoral candidate. The test profile included the maximum stress to be achieved during the test, the stress ratio, R, the maximum range of the load and strain, the specimen area, load frequency, and

temperature. The above specifications were then sent to the micro-profiler which in turn drives the load transducer. The test apparatus is shown in Fig. 7.

Also included in LOADTEST is a data acquisition system. At user specified cycle intervals (Data Acquisition Cycles, or DACs), data is recorded. This data is written to a file that is named the cycle number followed by ".dat." For example, 1.dat would include the cycle number, the temperature during cycle 1, and approximately 500 pairs of stress and strain data taken during the cycle. Additionally, a file called "minmax.dat" is produced, which includes the cycle number, maximum and minimum loads and strains , the specimen temperature and the material stiffness achieved during the cycle.

For the high temperature tests, two parabolic lamps were attached to the test stand. Chilled water was circulated through the lamps, the upper and lower grips, and the copper tubing which was wrapped around the load cell to protect the equipment from the high temperatures.

Strain was measured with a 1.27 cm (0.5 in.) gage length, high temperature quartz rod extensometer (MTS model 632.50b-04) placed on the specimen edge. The rods were replaced after every one to two tests due to breakage during specimen failure or merely dulling of the tips during testing. Each set of rods was calibrated before use to ensure that accurate strain data was taken within the projected strain range. To achieve superior resolution, the extensometer calibration for the tension-tension tests spanned over only positive strain values, as opposed to the tension-compression extensometer calibration, which also spanned over negative strain values. The extensometer unit was cooled by chilled air for the high temperature tests.
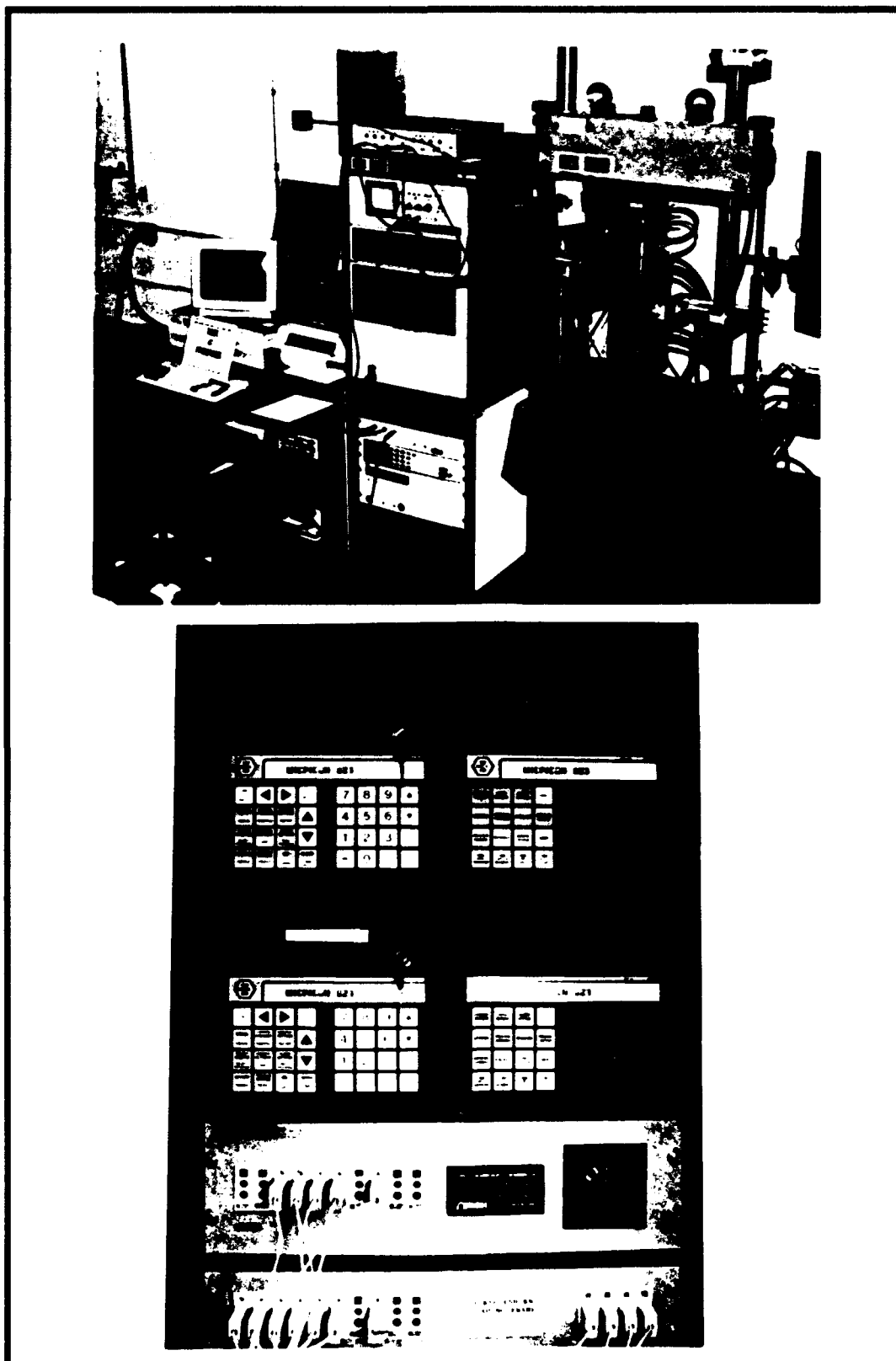
Figure 7. Test Apparatus

Dogbone Specimen Design

As elaborated in Chapter 1, it was evident that use of the dogbone specimen was necessary to avoid temperature gradient failures. Thus, a geometry had to be determined. This design involved tradeoffs between obtaining a maximum width reduction in the gage length versus a maximum radius of curvature at the specimen shoulder (Fig. 8). Due to localized stress concentrations caused by the high shear stress near the end of the transition contour between the gage section and tabbed region, dogbone specimens frequently fail at the specimen shoulder (54:1). Thus, a large radius of curvature is desirable to prevent this failure. This in turn increases the necessary specimen length, which increases the chance of premature failure due to buckling. The specimen length constraint, coupled with the desire to obtain a large reduction in specimen width at the center, while maintaining a large radius of curvature, resulted in a design loop. Appendix B includes the graphs used to determine the specimen geometry.

The results of several studies were considered in choosing the final specimen design. Worthem showed, through his Finite Element Analysis, that for a 15.2 cm (6 in.) long dogbone specimen with a 3.18 cm (1.25 in.) tab length, a 41.9 cm shoulder radius results in the lowest stress values in the transition region (54:1). Lerch and Halford (26)

reduced width = 0.508 cm (0.2 in)   specimen width = 1.27 cm (0.5 in)

shoulder
radius = 35.0 cm (13.7 in)

specimen length = 15.24 cm (6.0 in)
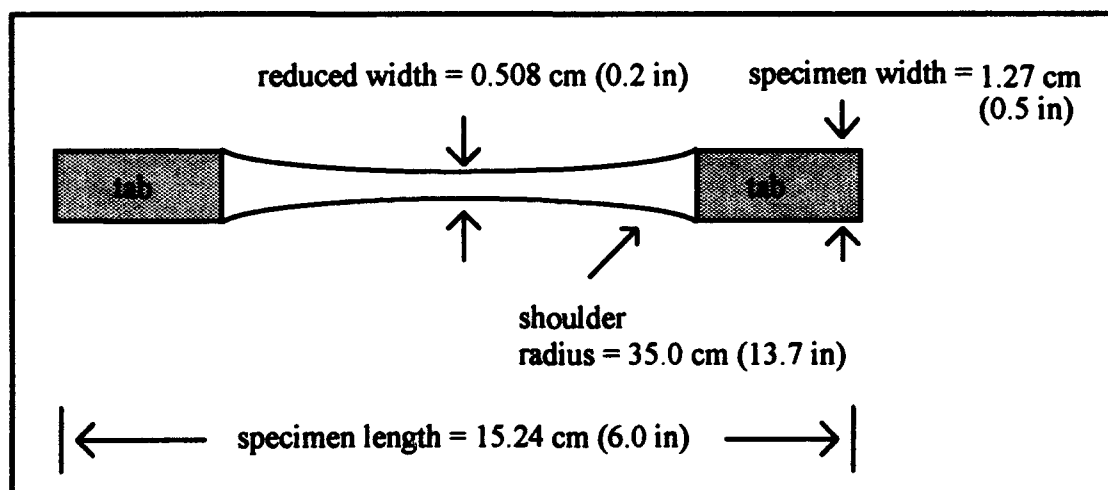
Figure 8. Dogbone Specimen Geometry

23

successfully used a 37.0 cm radius for their fully-reversed fatigue investigation of the $[\pm 30]_{4s}$ SCS-6/Ti-15-3 laminate. Verilli and Gabb (51) used a 36.8 cm radius for their fully-reversed fatigue tests of a $[0]_{32}$ Tungsten/Copper laminate. Thus, the final dogbone specimen design for the current work, as shown in Fig. 8, incorporates a similar radius of 35.0 cm.

Buckling Guide Design

Two buckling guide designs were considered and fabricated for use before the final buckling guide (the AFIT buckling guide) was designed and built. Both the Lockheed (1:63) and Battelle (29:49) buckling guides, designed for static compression tests only, had considerable drawbacks for use in fatigue testing.

The Lockheed buckling guide continually resulted in failure just outside the flange (Fig. 9). In this design, the guides themselves do not expand or contract during the fatigue loading. However, the specimen, which is bolted between the guides, undergoes considerable tensile and compressive strains during loading. This results in friction at the flange/specimen interface, which ultimately causes failure.

The Battelle buckling guide, Fig. 10, has been used successfully in static compression tests (29:49). However, this design has serious drawbacks for use in fatigue testing. The guide is not designed to be in contact with the specimen at all during testing. While this is conceivable for static tests, a 10 Hz frequency fatigue load would certainly cause the guide to come in contact with the specimen, causing friction. More importantly, the guides are in direct contact with the cooled grips. As a result, an even heat distribution along the specimen would be difficult, if not impossible, to obtain. This is unacceptable due to the temperature gradient problems discussed in Chapter 1.
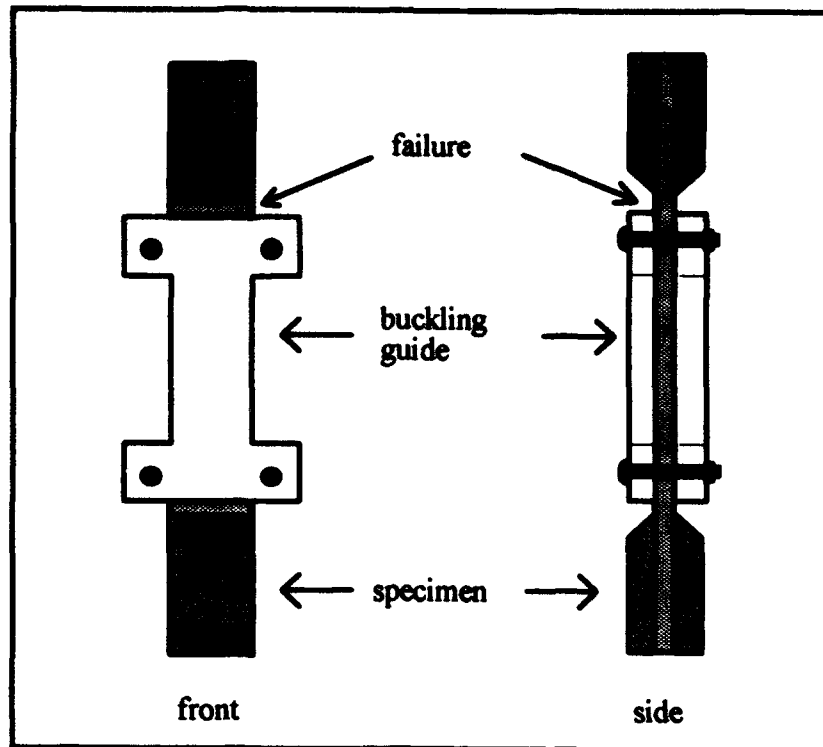
Figure 9. Lockheed Buckling Guide
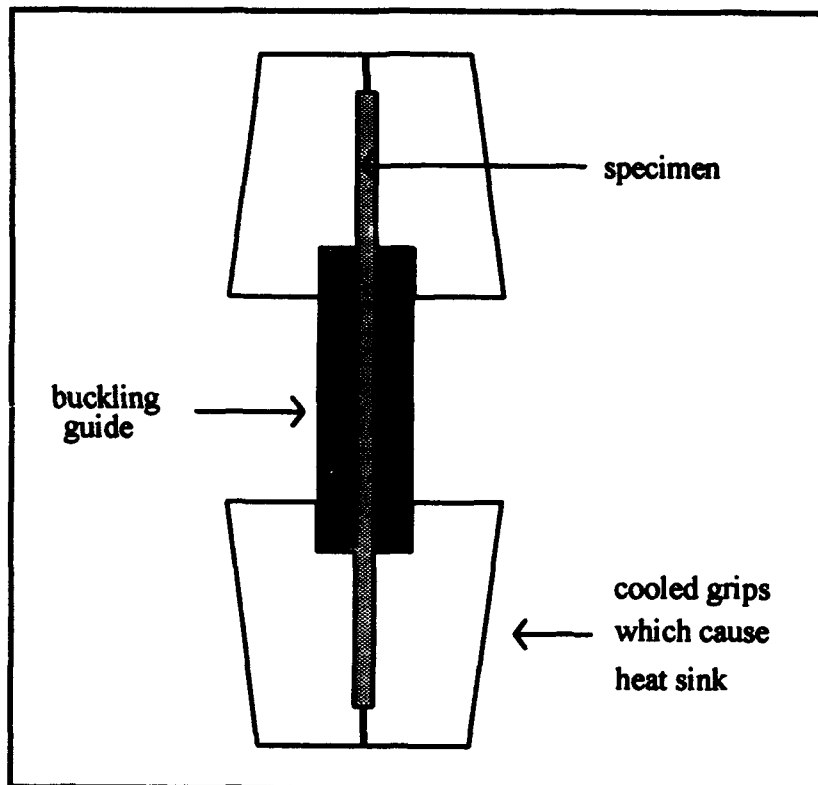
Figure 10. Battelle Buckling Guide

25

With the above drawbacks in mind, the AFIT buckling guide, Fig. 11, was designed for use with dogbone specimens. This design incorporates a unique arrangement which allows sliding between two portions of the guide. This sliding mechanism allows the guide to expand and contract with the specimen, decreasing the friction problems experienced with the previous guides. The two top pieces of the guide have a fork in the lower portion where they join with the sliding mechanism. A countersunk, flathead bolt protrudes from the sliding mechanism and when capped with a steel locknut and washer, permits axial sliding of the guide forks, while the specimen undergoes axial strain. The sliding mechanism locknut and washer restrict excessive out of plane movement of the guide fork, and hence, restrict excessive specimen buckling. Finally, when the specimen fails, the guide forks easily separate from the sliding mechanism, preventing damage to the guides.

The sliding mechanism bolts onto the lower portion of the specimen so that a minimal length of the specimen is left between the mechanism and the lower grips. The mechanism does not touch or rest on the cooled grips, however, as this would cause an undesired heat sink. Thermocouple grooves, 0.65 cm (0.25 in.) apart, are included so that the specimen temperature can be monitored during testing. Additionally, a minimal buckling guide width in the center region allows replicas to be taken on one side of the 0.508 cm (0.2 in.) width specimen, and extensometer rods to be placed on the other side of the specimen.
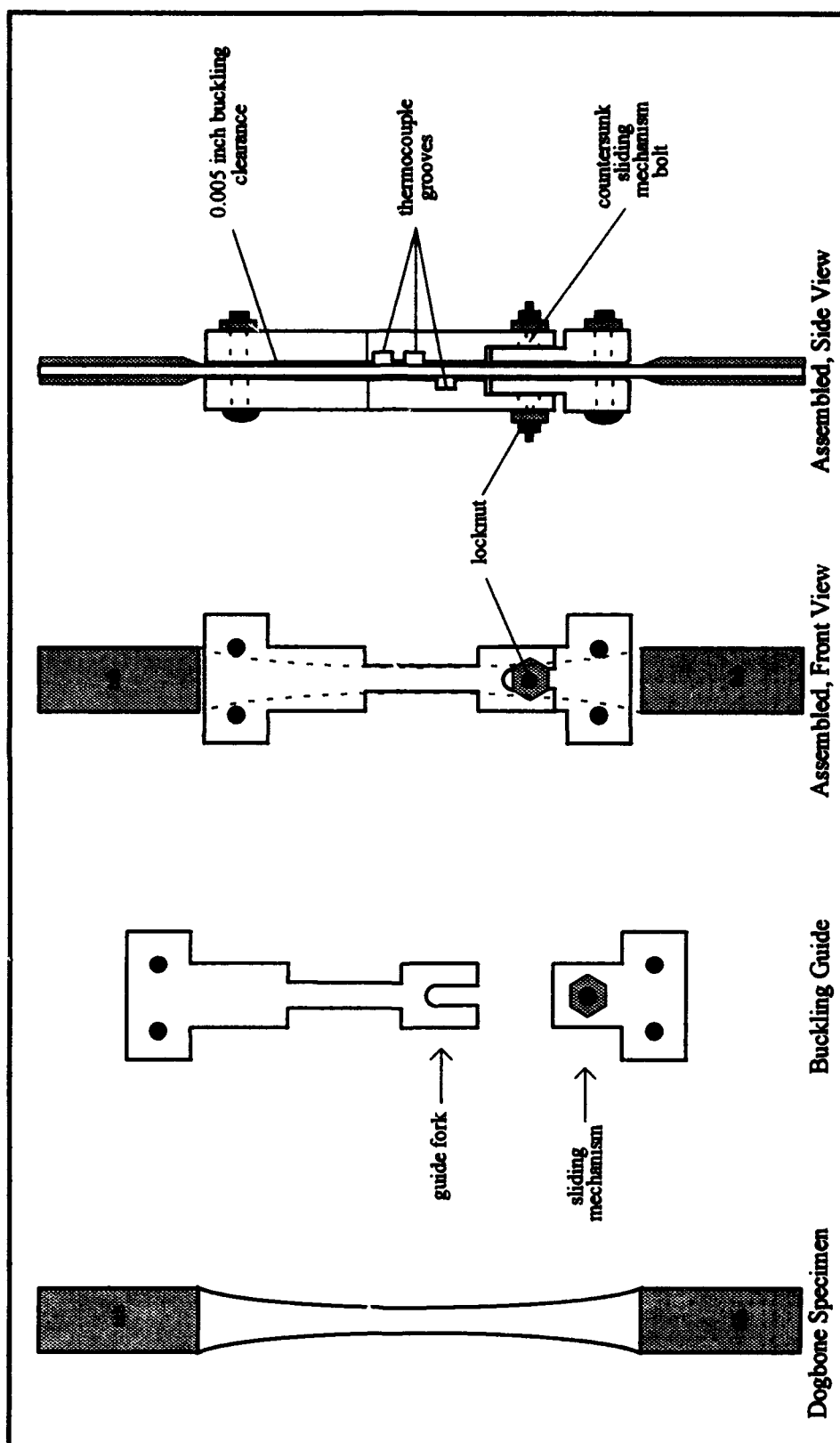
Figure 11. AFIT Buckling Guide

Room Temperature Tests/Procedure

    Specimen Preparation. Room temperature specimens were cut by technicians of the AFIT Model Shop with a diamond encrusted blade which was necessary to cut the extremely hard Silicon Carbide fibers. An oil coolant system was also used to prevent damage to the composite by way of burning. Each specimen was initially cut to a length of 15.24 cm (6 in.) and width of 1.27 (0.5 in.). The final specimens were later cut to a final length of three inches after polishing.

    These six inch strips were then heat treated at the WL/MD to stabilize the alpha phase of the matrix. Specimens were wrapped in Tantalum foil to protect from oxidation or impurities during the heat treat process. The wrapped specimens were then placed in a 700°C vacuum oven (approximately 1 x E6 Torrs) for 24 hours.

    Following heat treatment, the specimen edges were then polished at the WL/MD Metals Laboratory. The polishing was performed for two reasons. Surface flaws due to cutting needed to be removed to avoid stress concentrations. Additionally, one edge was needed to be finely polished to facilitate edge replication.

    The polishing process has been developed through the experience of previous thesis students and Metals Lab personnel. The specimens were placed in a polishing fixture which allowed for polishing on the Beuhler Maximet automatic polisher. The first stage of the polishing procedure, grinding, served to flatten specimen edges and to remove any surface pits. A number eight Metlap platen and 45 μm diamond slurry were used for the grinding process. A 15 μm slurry followed, which reduced the size of the scratches. The second stage of polishing was final polishing, which consisted of using 45, 15, and 9 μm slurrys on respective Perfmats. Significant progress was made during this stage, but scratches still existed The third stage of polishing removed any remaining scratches. Nylon mats were used with 3 and 1 micron slurries. Care must be taken to avoid ripping

the mat with the very sharp edges of the specimen. The final stage of polishing resulted in a mirror finish. This step used a neoprene mat in conjunction with a chemical solution of Mastermet, Hydrogen Peroxide, and distilled water. Following this stage, it was extremely important to immediately rinse and steam clean the specimen. Mastermet, if allowed to dry, will stain the edge of the specimen, and can then be removed only by repolishing.

Once the 15.24 cm (6 in.) strips were polished, they were cut into 7.62 cm (3 in.) length specimens using the slow speed diamond saw. Fiberglass tabs were then applied using epoxy which was cured for one hour at 67.2° C (153° F) in the Aero Lab oven.

The last stage of specimen preparation was edge examination. A very accurate analysis of existing edge damage was necessary to avoid mistaking this damage for that which occurred during the fatigue tests. To this end, a detailed picture was drawn of the gage section which included any fiber breaks or other damage. This picture was then used to record the damage as it occurred during the fatigue test. This damage was monitored through the Acetate edge replica.

Acetate Replicas. To obtain an accurate picture of the damage as it progressed throughout the life of the specimen, the tests was put on hold periodically to allow for acetate replication. This process allowed for examination of the specimen edge without removing it from the test stand. This was beneficial since existing cracks, fiber breaks, and other damage which open up slightly when under a load, may close when the load is relieved, thus making the damage less detectable.

The replicas were taken at tensile and compressive loads ranging from 30 to 50 percent of the maximum test load. Once the load was set, the specimen was wetted with Acetone, and a piece of acetyl cellulose was pressed against the specimen edge for 50 to 60 seconds. This allowed for the acetate to melt into the cracks and crevices, leaving an

imprint of the specimen edge. The acetate replica was then pressed between two glass plates and placed in a 67.2° C (153° F) oven for one half hour. This flattened the replica, which made it easier to focus on during examination and photography.

Test Procedures. The specimen was placed into the test fixture with the 0° fibers running parallel to the load direction. With the test stand in displacement control, the specimen was first gripped in the upper grip, then the alignment was verified using a level. At this point, the extensometer was also checked to make sure it sat on the specimen without slipping. Once proper alignment was achieved, the lower head was moved into position. The test stand was then placed into load control, and the grips in the lower head were quickly gripped onto the specimen. It is imperative that this is done quickly, as the lower head floats while in load control.

The grip pressure is based on pounds per square inch of the grip surface. Thus, it is important to adjust the pressure accordingly if one changes specimen widths, or area in the grips. It was found that 6.2 to 6.9 MPa (900 to 1000 psi) grip pressure was sufficient for a 1.27 cm (0.5 in.) width specimen with approximately 1 inch length in the grips. However, when the specimen width was changed to 0.635 cm (0.25 in.) for the tension-tension tests, the grip pressure was adjusted to half the pressure.

Once the specimen was placed in the test stand, the extensometer was placed on the non-replica, or right, edge of the specimen. The rods were adjusted so that the distance between the quartz rod tips was exactly 1.27 cm (0.5 in.), resulting in an initial strain reading of zero. Any deviation from zero strain was recorded so that the strain data could be adjusted accordingly.

Once the extensometer was zeroed, the testing began. The initial cycle was performed using a program called STATIC, developed by Aero Lab Technician Mark Derriso. This program allowed for manual loading of the specimen to the desired

maximum and minimum load. Replicas were taken just after the observed knee in the stress strain curve to document the debonding that occurs. The loading was then continued to the minimum load and back to zero. The initial modulus was obtained from this data.

Following the initial cycle, the fatigue test began. The specimen was subjected to a 10 Hz triangular load sequence as shown previously in Figs. 1 and 2. The test was stopped at least every decade of the test to take replicas. This also allowed for 50 to 100 cycles to be run at 1 Hz. This was necessary since hysteresis loops obtained from 10 Hz data were severely aliased due to a sampling rate mismatch between the analog to digital board and the load transducer.

Prior to testing, load, strain, and displacement limits were set on the micro profiler. If these limits were exceeded, the hydraulics cut off, and the test was terminated. This ensured that if the extensometer slipped out of it's calibrated range, or if there were unacceptable load spikes, the test would not proceed. More importantly, if the displacement limits were exceeded due to specimen failure, the test stopped, the lower head floated downward; the failed specimen was not damaged due to continuation of the test.

Elevated Temperature Tests/Procedure

Specimen Preparation. The initial high temperature test specimens were prepared in the same manner as the room temperature specimens, with two exceptions. The specimen length was four inches, one inch longer than the room temperature, due to the increased gage length needed to facilitate use of the heat lamps and reduction nozzles. Aluminum tabs were used instead of the fiberglass epoxy tabs which would not withstand the high temperatures. However, the dogbone specimens which were used with the buckling guide fixture were polished differently than the room temperature specimens.

31

The dogbone specimens were cut at the AFIT Model Shop using a diamond encrusted circular bit. The specimen geometry was input to a Computer Aided Design (CAD) software package, which interfaced with the numerically controlled cutting machine. The program specified an initial roughcut of the specimen, followed by a slow feed rate final cut. Due to the extreme hardness of the silicon carbide fibers in conjunction with the titanium matrix, the fabrication of one dogbone used an entire bit. Care had to be taken to adjust the level of the bit due to the wearing-off of the diamond. This wear detracted from obtaining a precision cut

The other cutting options for the dogbone specimens were Electronic Dispersive Machining (EDM), and water-jet cutting. The EDM method was not chosen because it has been found to degrade the fatigue properties of metal matrix composites (10:225). The waterjet method has been found to cause the least damage to the material; however, it was cost-prohibitive for this research.

After the dogbone specimens were cut, they needed to be polished. The failures that often occur in the shoulder of the dogbone specimen can be initiated by burrs or edge defects near this region. These defects cause stress concentrations to occur in an already highly stressed region, but can be removed through the polishing process. Additionally, the observations of damage progression via edge replicas is impossible without a finely polished surface. Polishing of dogbone specimens is rarely performed due to the irregular geometry, which prohibits any type of automated polishing techniques. For these reasons, a hand polishing technique was developed.

To avoid the rounding of specimen edges which occurs during hand polishing, the SCS-6/Ti-15-3 specimens were sandwiched between two "dummy" MMC dogbone specimens with the same geometry. The four specimens were glued together and allowed to set overnight.

The first, or grinding, stage of polishing was performed using a hand polishing tool similar to a dental tool. A diamond grinding pad was attached to the tool and the specimen was ground until all surfaces were even. Care was taken during grinding to douse the specimens with water often to avoid burning. The process continued with hand grinding using an artist's eraser wrapped with 240, 360, and then 400 grit silicon carbide grinding paper. This process further evened the surfaces and removed the larger scratches imposed by the diamond pad. The specimens were then split apart and reglued so that the opposite side was as close to even as possible. The first side was used for the extensometer, and the second side was ground as above, then finely polished for replica taking.

The second, or polishing stage, was also performed with the dental tool, but with a nylon pad. The specimens were successively wet with 45, 15, 6, 3, and 1 μm diamond slurrys in conjunction with the appropriate diamond paste. Next, a neoprene pad was used with the dental tool in conjunction with Mastermet. Again, care was taken to rinse and steam clean the specimens immediately following this step, to avoid staining. Once the specimens were polished, they were examined for existing damage and a picture was drawn in the same manner as for the room temperature specimens.

The dogbone polishing process is more labor-intensive and time-consuming than the automated polishing technique used for the rectangular specimens. As a result of the time invested, however, the replicas taken from these specimens were of similar quality as those obtained from rectangular specimens.

Test Procedure. Before placing the specimen into the buckling guide, the two type K chromel-alumel thermocoupies were tack welded to the face of the specimen, each 0.635 cm (0.25 in.) away from the center. These provided temperature information to the Micricon 825, which controlled the heat lamps. A third thermocouple, welded to the

33

center of the specimen, provided LOADTEST with the temperature information. Once these thermocouples were applied, the two long pieces of the buckling guides were carefully placed on either side of the specimen, matching the thermocouple grooves with the thermocouples. Care was taken to mount the specimen with its straight heat zone region parallel to the edges of the guides and to the load direction. Once the specimen was correctly placed, the top screws were tightened, ensuring that the polished side of the specimen protruded slightly from the buckling guide. This allowed edge replicas to be taken.

Before attaching the sliding mechanisms, the locknuts were tightened an appropriate amount, and the countersunk bolt head was then tightened into position to avoid friction with the specimen during testing. To reduce friction between the buckling guide components, powdered graphite was applied to the clean, dry, sliding mechanism. The two sliding mechanisms were then slid into place. Once it was verified that the locknut was tight enough to counter any out of plane displacement caused by buckling of the specimen, yet allowed the guide forks to slide easily, the sliding mechanisms were bolted into place.

The specimen was then mounted into the test fixture in the same manner as the room temperature specimens. The extensometer was placed on the specimen and zeroed (Fig. 12). The LOADTEST program was then initiated. The specimen was initially brought up to 427° C, and the thermal strain was recorded. The initial 100 cycles were run at 1 Hz to obtain hysteresis and modulus data and also to ensure that excessive buckling, or out of plane movement was not occurring. This was visually checked and hysteresis loops were also plotted. If the compression portion of the loop was cusped, denoting the buckling effect, the locknuts were tightened, further restricting the movement. The effect of excessive buckling on the hysteresis loops is shown in Fig. 13.
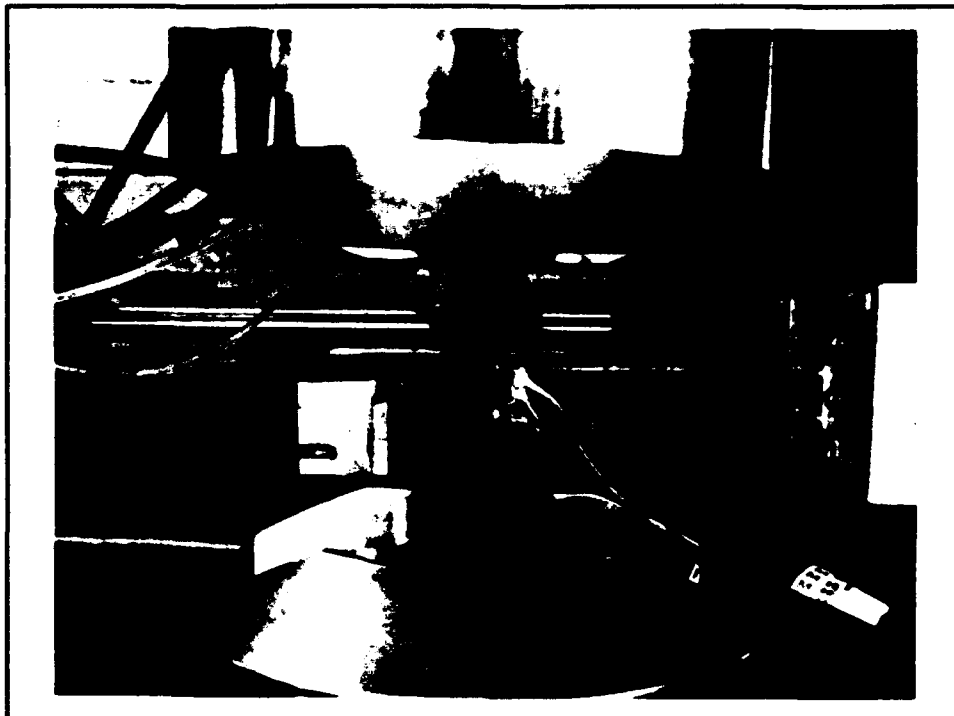
Figure 12. Specimen and Buckling Guide Mounted in Test Stand
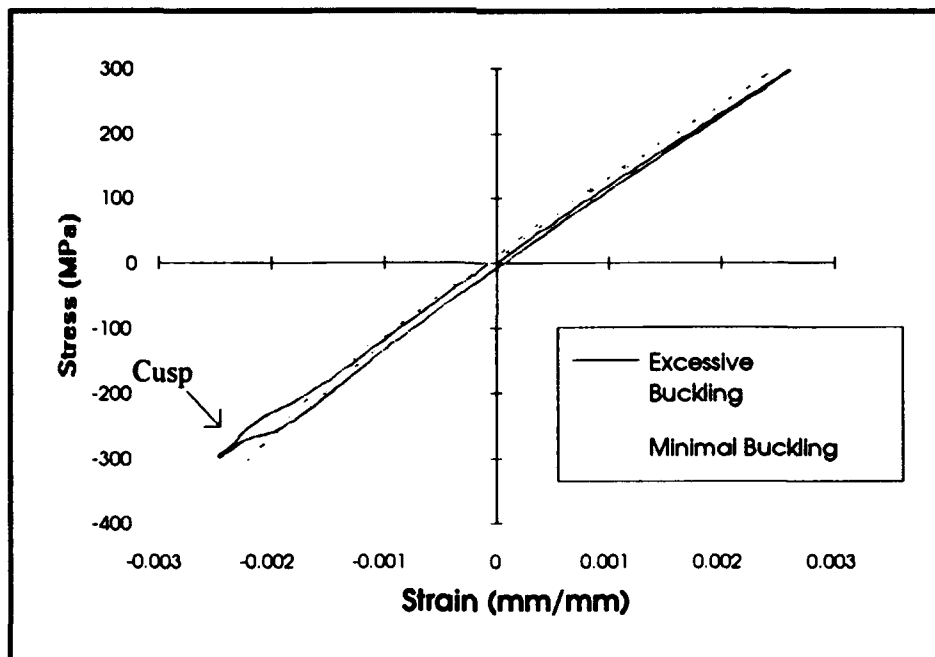
Figure 13. Effect of Excessive Buckling On The Hysteresis Loop

The remaining cycles to failure were run at 10 Hz, interspersed with periodic 1 Hz segments to obtain hysteresis and modulus data. The testing was periodically stopped, and the specimen cooled, to take replicas. The specimen cooling, replica taking, and specimen reheating procedure took approximately one hour, so it was performed only when significant changes in strain or modulus had occurred.

Post-Failure Analysis

Following failure, pictures were taken of the entire specimen to keep a record of the overall location of the failure. The edge replicas were examined to determine the onset of deformation and damage; this was recorded on the previously hand drawn picture of the specimen edge. The polished edge was then examined and fiber/matrix damage recorded on the same drawing. This allowed for a clear picture of damage progression in the specimen. Damage of significance or particular interest was also photographed.

Once all pictures were taken, the specimen was sectioned. In general, each specimen was cut so that one longitudinal and one transverse section resulted. The sectioned section configuration is illustrated in Fig. 5. The fracture surface sections were observed in the Scanning Electron Microscope (SEM). This aided in the characterization of the failure. The remaining sections were post heat treated at 427° C to aid in the observation of slip bands (25:1).

The sections were then mounted in Buehler Konductimet, a black conductive mounting compound, using the Simplimet mounting press in the Aero Lab. The Konductimet surrounds the sectioned piece, and allows for automated polishing. The section polishing procedure is similar to that of the specimen edges. The initial step is rough polishing with a 45 micron diamond slurry and a number 8 platen. This is followed by both 15 and 9 micron slurries with the number 8 platen. The sections are then polished on 45, 15, and 6 micron Perfmats. This is followed by 3 and 1 μm diamond slurries on a

nylon mat. The final polishing phase contained three steps. First, the sections were place on a Buehler Vibromet vibrating polisher with a one micron diamond slurry for 24 hours. The sections are then placed on a Vibromet with half micron diamond slurry for approximately eight hours. The final step is the Mastermet Vibromet, used for approximately 1 hour. The Mastermet is the aggressive chemical polish used on the pre-tested specimens. This step removes all scratches larger than 0.06 micron. Once polished, the sections were ready for micro-mechanical examination in the SEM.

Following final polishing, selected specimens were then etched. In this process, a three percent solution of Ammonium Fluoride and Hydrofluoric Acid (NH_4F+HF) is applied to the mounted specimen. This solution attacks the alpha phase precipitates which makes possible the observation of matrix plasticity and grain boundaries.

IV. Results

An investigation of the fatigue behavior of a material must include both
macromechanic and micromechanic examinations; in this study, they are used to
characterize the cyclic life and the associated deformation mechanisms for each fatigue
loading condition. This chapter describes, in detail, the fundamentals of macro-mechanic
and micro-mechanic evaluations as they apply to the cross-ply SCS-6/Ti-15-3 MMC.
These evaluations are then performed for each load case: TC RT, TT RT, and TC HT.

Fundamentals of the Macro-mechanic Evaluation

The macromechanic behavior of the composite consists of the fatigue life, stiffness
(Young's modulus) degradation, and strain response during cycling. The fatigue life of the
composite can be illustrated on the Wohler, or SN, diagram. This diagram is the basis of
the standard stress-life method for fatigue life characterization, in which either the
maximum applied stress or the applied stress range is plotted versus the number of fatigue
cycles to specimen failure. The SN curves for all materials, including metals, polymers,
and composites have a negative slope (2:297), meaning that as the applied stress
decreases, the number of cycles to failure increases. Factors which influence the exact
shape of the SN curve for composite materials include the matrix material, ply orientation,
volume fraction of reinforcement (fibers), interface properties, type of loading, mean
stress, frequency, and environment. Three of these factors vary within the loading cases
investigated in the current work. The type of loading differs from tension-compression
to tension-tension (Figs. 1 and 2). The mean stress also varies from zero for the
tension-compression case to a positive value for the tension-tension case (Fig. 4). Finally,
the temperature environment is clearly different for the high temperature loading case as
compared to the room temperature loading cases.

Many researchers have attempted to divide the SN curve into different portions in which certain failure mechanisms play dominant roles. Majumdar and Lerch, following Talreja's approach (49), have suggested that the fatigue life, or SN curve, of a MMC can be broken up into three regimes: Regime 1,2, and 3 (30:7). Specifically, for the unidirectional SCS-6/Ti-15-3 laminate they tested in tension-tension fatigue at a R-ratio of 0.1, they stated that Regime 1 failure occurs solely by overload of the fibers. Regime 2 failure occurs primarily due to matrix cracking, and Regime 3 consists of fatigue lives upward of 1 million cycles in which matrix cracks simply do not initiate, and if they do, they are quickly arrested. The authors found that the transition between Regimes 1 and 2, and also between Regimes 2 and 3, are complex, consisting of mixed mode failures.

In the current work, an additional regime of the SN curve will be defined due to the variances in the fatigue behavior of the cross-ply laminate examined in this study, and unidirectional laminates of previous studies. The onset and type of deformation differs between the two primarily due to the presence of 90° fibers in the cross-ply laminate. These 90° fibers initiate matrix cracks much earlier in the cross-ply fatigue life than do the 0° fibers in the unidirectional laminate fatigue life. For this reason, a significant portion of the cross-ply SN curve is occupied by the mixed-mode transition between Regimes 1 and 2. This portion will be referred to in the current work as Regime 2a. Regimes 1, 2 and 3 will remain as Majumdar and Lerch have defined. Talreja's concept of the regimes of the SN curve, as adapted by Majumdar and Lerch, in addition to the concept adopted used in this study for the cross-ply laminate, are illustrated in Figs. 14 and 15.

These type of fatigue diagrams are generally used when a significant amount of testing has been accomplished so that the exact location of transition from one regime of the SN curve to the next is known. Since, in the current work, this amount of research
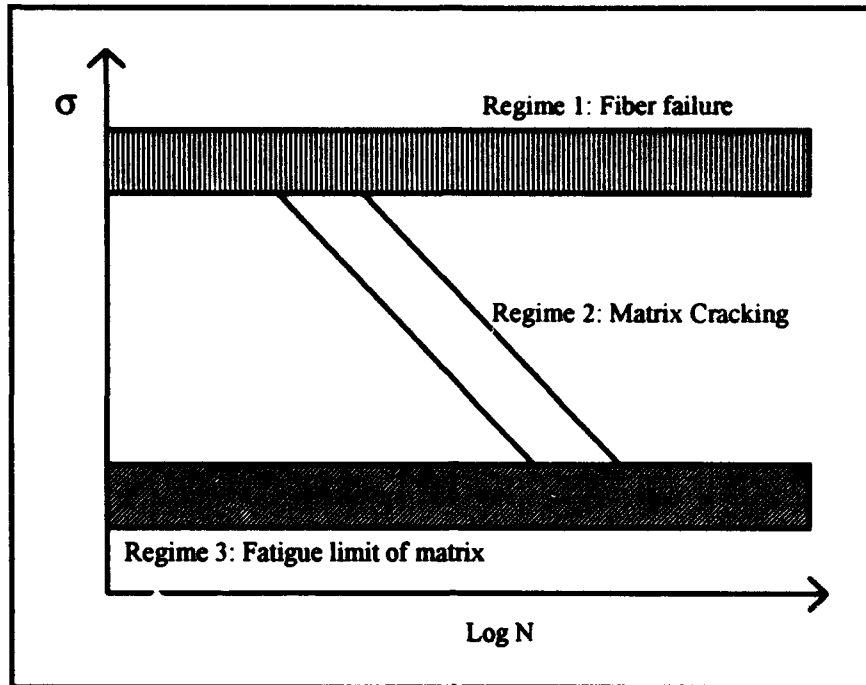
Figure 14. Talreja's Model for Regimes of the Unidirectional Laminate SN Curve
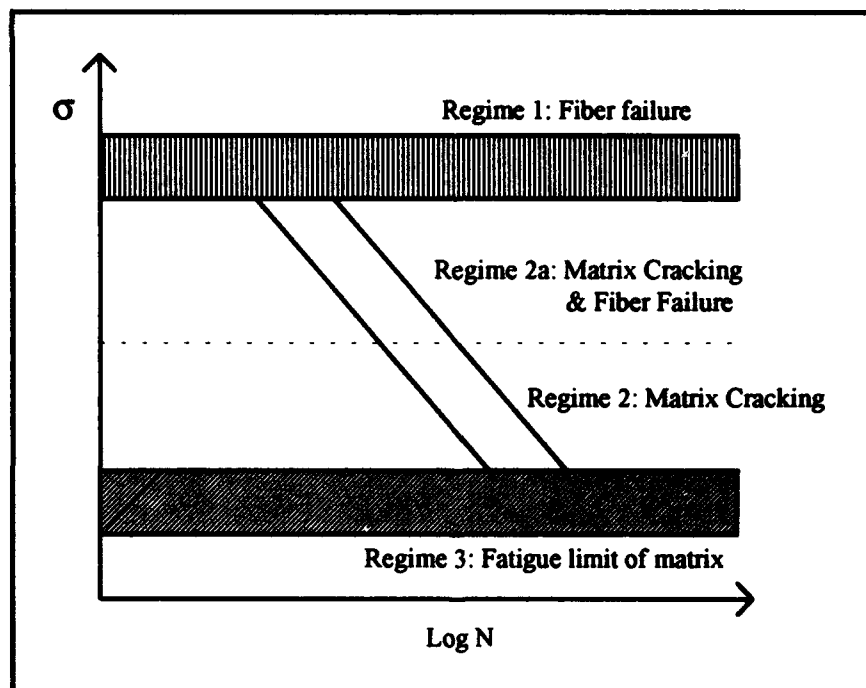
Figure 15. Regimes of SN Curve for Cross-Ply Laminate Adopted in Current Work

was not feasible, a different method of demarcation between the regimes is used which merely *separates* the tests which are performed into their respective regimes. It is stressed that the lines which are drawn to separate the regimes are qualitative in nature and not quantitative, and thus are not tied to specific values of fatigue life. Figures 16 and 17 illustrate this method for both the classic unidirectional and the current cross-ply cases.

In addition to the fatigue life approach, the macroscopic evaluation of a fatigued specimen can also be based on modulus reduction. The stiffness, or modulus of a material is the ratio of the applied stress to the resulting strain:

$$E = \frac{\sigma}{\varepsilon} \qquad (1)$$

Since the stress remains constant during load-controlled fatigue tests, the modulus changes only with a change in strain. This change in strain is caused by deformation within the material, and thus a drop in modulus almost always indicates damage initiation or progression.

In fatigue tests of cross-ply laminates, the modus undergoes a change within the first cycle if the load is high enough to debond the 90° fibers. Once the debond has occurred, the cross-ply contribution to the composite is reduced, in turn reducing the stiffness. This change is evidenced by a "knee" in the stress-strain curve which separates the initial and secondary moduli. The stress-strain curve for subsequent cycles then becomes linear, with a modulus close to the secondary modulus of the virgin material (2:295). If the applied load is high enough, a second knee will occur due to the onset of nonlinearity of the matrix. Modulus data in this work will be presented as a ratio of the instantaneous modulus to the initial modulus.
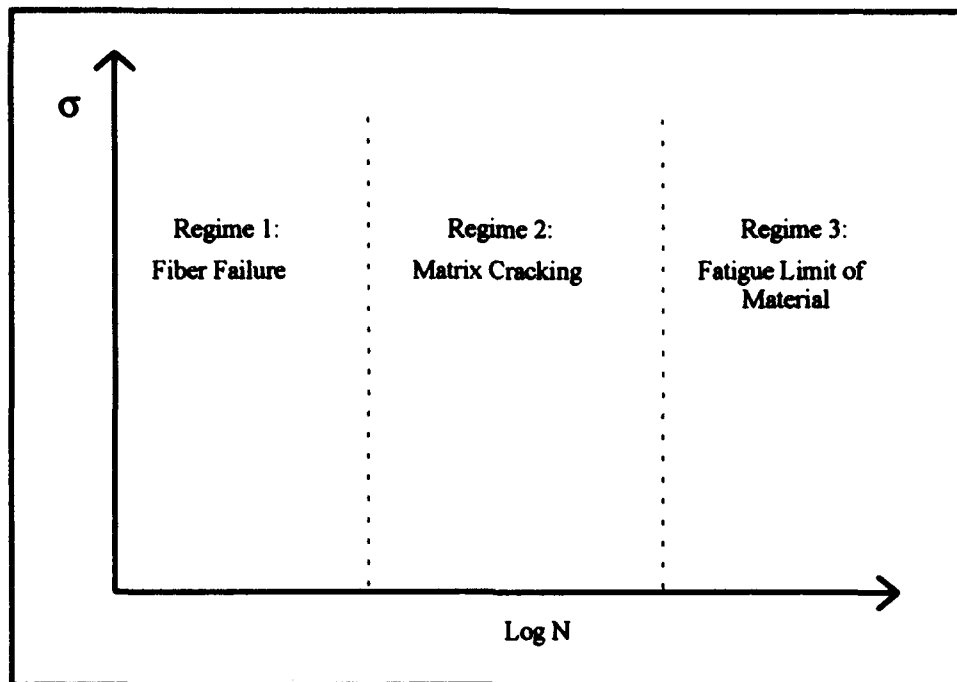
Figure 16. Talreja's Concept of the 0° Laminate SN Curve Used in Current Work
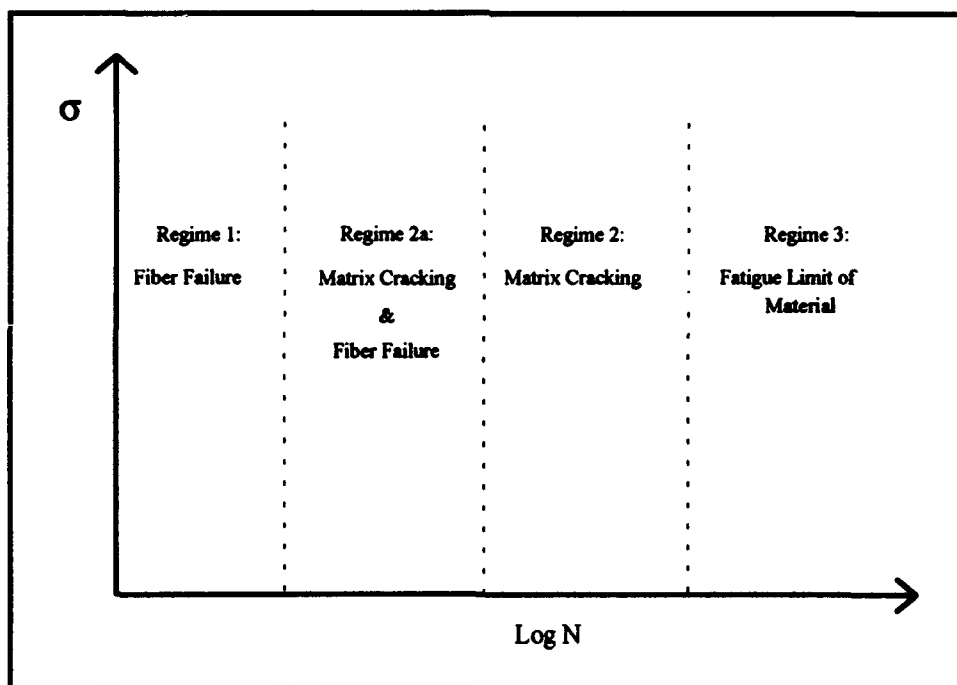
Figure 17. Regimes of SN Curve for the Cross-Ply Laminate

42

In addition to debonding, other deformation can contribute to a strain increase, or stiffness reduction. Matrix cracking, fiber breaking, and matrix plasticity all cause increased specimen elongation with applied load. Thus, as the specimen is fatigued, more and more damage begins to take place, and a modulus reduction eventually occurs. The percent of fatigue life at which this reduction begins, and the extent to which it falls varies with applied stress and loading condition.

Although the fatigue life, modulus degradation, and strain increases throughout the fatigue life of a material are strong *indicators* that damage has taken place within the specimen, the damage *mechanisms* remain unknown without performing a micromechanic investigation.

Fundamentals of the Micro-mechanic Evaluation

The micro-mechanic evaluation seeks to determine the *cause* of deformation initiation and the type of deformation *progression* throughout the life of the specimen. In this study, this information is obtained through the examination of acetate replicas of the specimen edges, sectioned specimens, and fracture surfaces, providing the background necessary to fully characterize the deformation mechanisms associated with fatigue of MMCs.

The deformation mechanisms which have been found in this research are divided into either damage or plasticity. Damage is defined as the formation of new and free surfaces within the specimen and consists of fiber and matrix cracking, fiber-matrix reaction zone cracking, and debonding of the fiber-matrix interface. Plasticity is defined as the processes involving dislocation nucleation and motion, and consists primarily of slip band formation. Each of these mechanisms will be explained and illustrated as a basis for the discussion which follows for each loading case.

43

The types of damage are illustrated in Fig. 18, and include fiber breaks, reaction zone cracks, matrix cracks, and debonding. *Fiber breaks* exist in both the 0° and 90° fibers. Some fibers are broken or damaged before testing as a result of machining or fabrication. More commonly, however, fiber breaks are due to tensile overload. This is caused by stress transfer to the 0° fibers from the damaged matrix. Occasionally, compressive loads may lead to *radial cracking* in 90° fibers. *Reaction zone cracks (rzcs)* are the most common form of damage initiation in this study. The fiber-matrix reaction zone is the area between the fiber and the matrix in which the two have chemically reacted during fabrication. It is made up of titanium carbides and titanium silicates, and is very
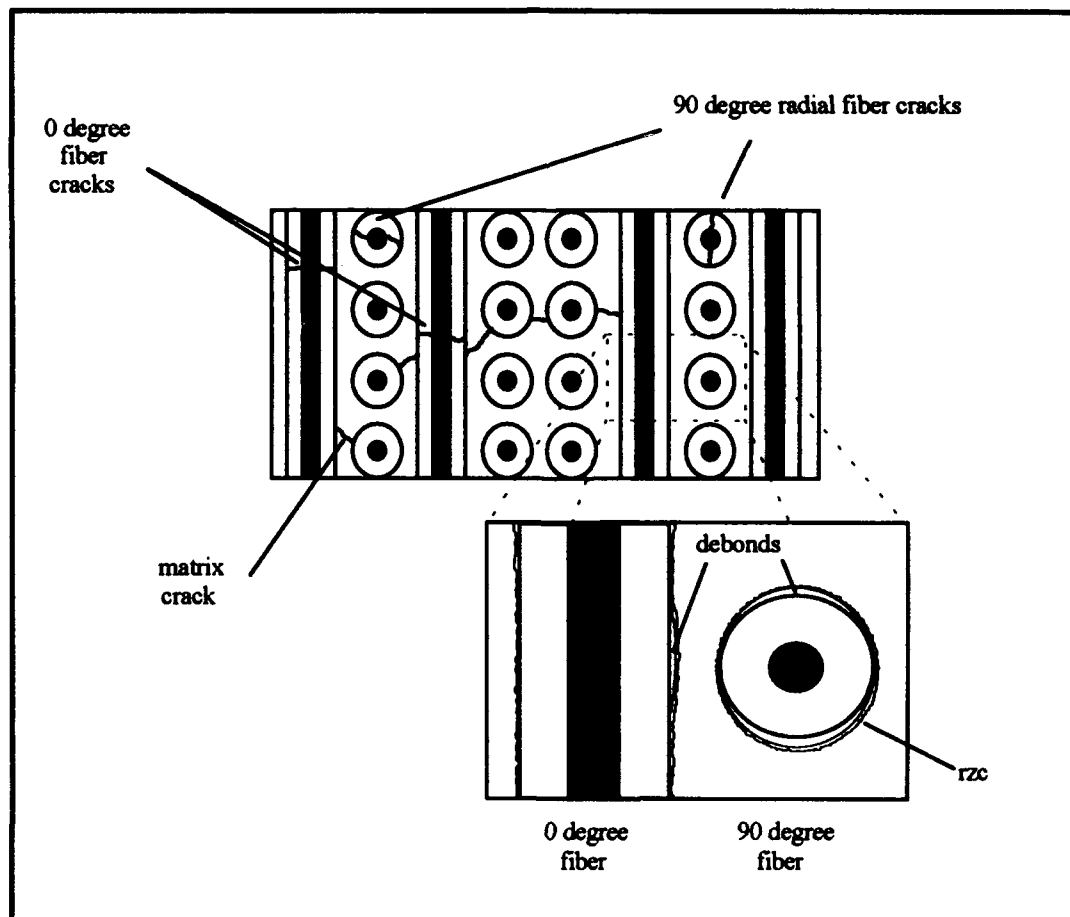
Figure 18. Typical Damage Mechanisms in the Cross-Ply Laminate

44

brittle (22:210, 23:712). As a result, this area is extremely prone to damage in the form of cracking. *Matrix cracking* in this composite system almost always nucleates at rzcs on the 90° fibers, although broken 0° fibers occasionally contribute to matrix cracks. Once initiated, these cracks grow under cyclic loading. *Debonding* is the separation of the fiber from the matrix, and occurs in both the 0° and 90° fibers, generally between the carbon rich outer layer of the fiber and the reaction zone.

Plasticity, or plastic deformation, of metals is caused by slip, or shear, deformation of metal atoms on specific crystallographic planes called *slip planes*. In order for this deformation to occur, a high density of crystalline imperfections which are known as dislocations must be present in the metal. These dislocations are created in extremely large numbers, approximately 10^6 cm/cm^3, as the metal solidifies, and also when the metal is deformed (47:275). Slip usually occurs on the closest packed planes of the metal crystal, and only occurs when the applied stress exceeds the yield stress of the metal. A close examination of slipped surfaces of metals reveals that slip occurs on many slip planes within a single *slip band*. A slip band is defined as a line marking on the surface of a metal due to slip caused by permanent deformation (47:314). Thus, the existence of slip bands in a material implies that plasticity has occurred.

The slip characteristics of a material strongly influence the microscopic mode of fatigue crack growth. In ductile solids such as the Ti-15-3 matrix used in this research, cyclic crack growth can be thought of as a process of intense localized deformation in slip bands near the crack tip, which in turn leads to the creation of new crack surfaces by shear decohesion. When the crack and the zone of plastic deformation surrounding the crack tip are confined to within a few grain diameters, crack growth occurs predominantly by single shear, in the direction of the primary slip system (48:195). Thus, the crack appears to grow along, or parallel to the slip bands. This is shown in Fig. 19, and has been termed Stage I crack growth by Forsyth (12:63).

45
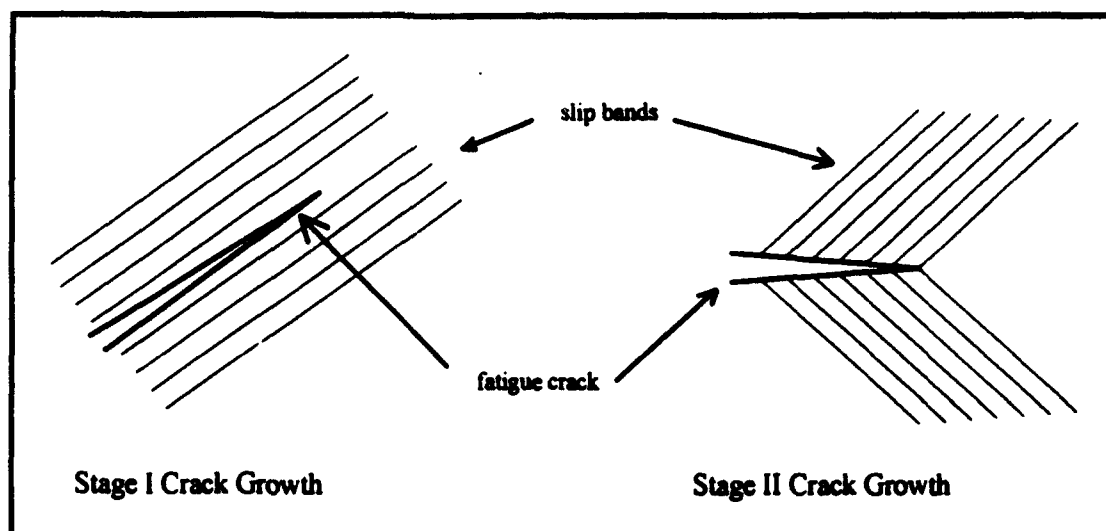
Figure 19. Forsyth's Model For Stage I and II Fatigue Crack Growth

If the crack tip stress intensity range, (ΔK), is increased, the plastic zone at the crack tip encompasses many grains, and results in simultaneous or alternating flow along two slip systems, resulting in a planar crack normal to the applied stress (48:197). Thus, the slip bands appear to emanate from the crack tip. This is shown in Fig. 20, and has been termed Stage II crack growth by Forsyth (12:64).

In monolithic materials, slip is a surface phenomenon and generally emanates from discontinuities on the specimen surface. However, the fibers of a MMC, the 90° fibers in particular, act as discontinuities within the specimen and are potent nucleation sites for slip. Figure 20 illustrates typical slip band nucleation at both 0° and 90° fibers.
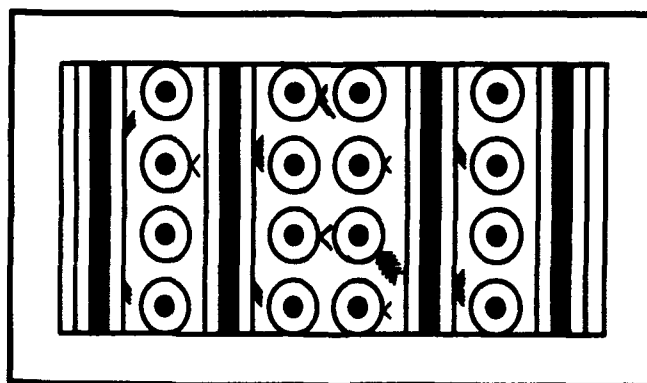
Figure 20. Typical Slip Band Nucleation in the Cross-Ply Laminate

46

Stage II crack growth in many engineering alloys leads to fatigue *striations;* the cyclic opening and closing of the crack develops a pattern of ripples on the fracture surface. Thus, these marks are indications of periodic crack advance and arrest. It is significant to note, however, that these striations are not always found on fatigue fracture surfaces, since "...fatigue cracks sometimes propagate without leaving striations on the fracture surface" (11: 39).

Fractography, or the examination of the fracture surface using very high magnification microscopes, has the potential of providing information on the cause of specimen failure, and/or the fatigue crack growth process. Two basic types of fracture surfaces are those characterized by brittle cleavage and ductile void coalescence.

Brittle cleavage is caused by direct separation along crystallographic planes due to a simple breaking of atomic bonds (8:40), which is generally associated with crack propagation through the material. The flat cleavage facets which are formed have a high reflectivity, which gives the fracture surface a bright shiny appearance. In contrast, a fracture surface formed by *ductile void coalescence* is generally very dull. This type of surface is generally formed by an overload in tension, during which the intermediate particles of sub-micron size lose coherence with the matrix, causing extreme plastic flow to occur in their vicinity, resulting the classic cup and cone type fracture (8:40). When the fracture surface is observed under high magnification, it is covered with dimples which represent the coalesced voids.

TC RT Macro-mechanic Evaluation

A rectangular specimen geometry was used in the TC RT tests. The majority of the specimens broke within the gage length, with some of the failures occurring closer to the tabs. The 175 MPa specimen, after failure, is shown in Fig. 21.

Figure 21. Rectangular Specimen Geometry Used for TC RT Tests

The fatigue life data is plotted on a maximum applied stress basis in Fig. 22, and the stress, strain, fatigue life, and modulus degradation, and dominant failure modes for the tension-compression tests conducted at room temperature are summarized in Table 1. The strain range referred to in Table 1 is defined as the difference between the maximum and minimum strain during the steady-state strain portion of the fatigue life (Fig. 23). Note that the *maximum* applied stress is plotted as the function of the fatigue life. For this fully-reversed tension-compression fatigue (R-ratio = -1), the stress *range* is twice the maximum applied stress. Thus, plotting the stress range versus cycles to failure results in shifting the fatigue life curve up and to the right. This is not of major consequence in this section, or when comparing fatigue data generated at the same R-ratio, however it will come into play when comparing data generated at different R-ratios, or different loading conditions.
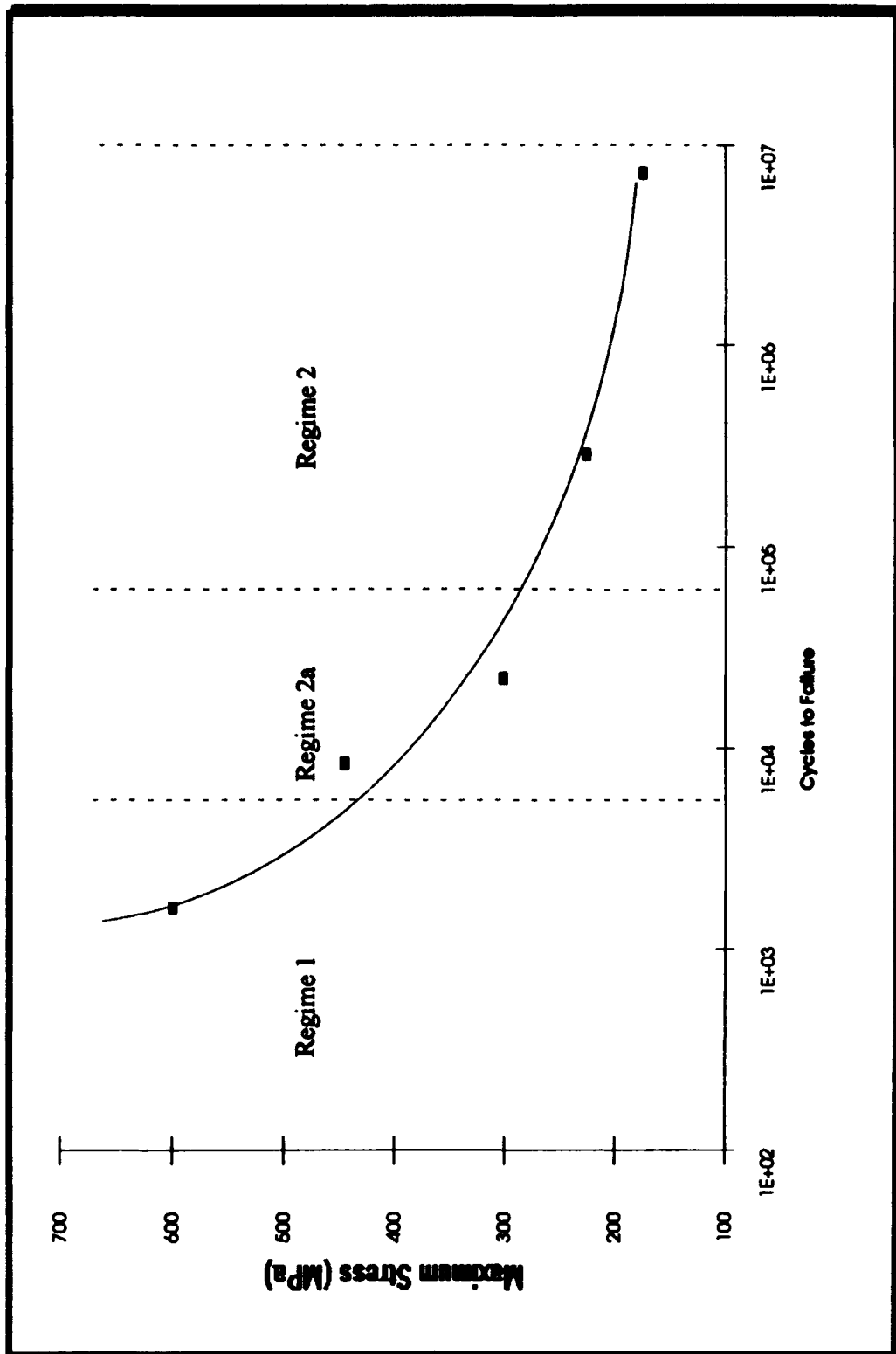
Figure 22. TC RT: SN Curve.

Table 1. TC RT: Macro-mechanic Results Summary

Max Stress (MPa)	Stress Range (MPa)	Max Strain (%)	Strain Range (%)	Regime of Failure	Cycles to Failure	Percent of Initial Strain at Failure $(\varepsilon_f/\varepsilon_i)*100$	Percent of Initial Modulus at Failure $(E_f/E)*100$	Dominant Failure Modes
175	350	0.603	0.267	2	7,287,536	381.65	47.8	mc (extensive), mp
225	450	0.502	0.329	2	287,096	288.51	50.8	mc (extensive), mp
300	600	0.465	0.465	2a	22,297	186.0	72.9	mc, mp (limited), ff (limited)
445	900	0.578	0.680	2a	8,296	167.05	84.2	mp (extensive), ff
600	1200	0.623	0.900	1	1,610	124.35	89.0	mp (extensive), ff (extensive) db: Longitudinal & transverse
* mc = matrix cracking, mp = matrix plasticity, ff = fiber failure, db = debond								
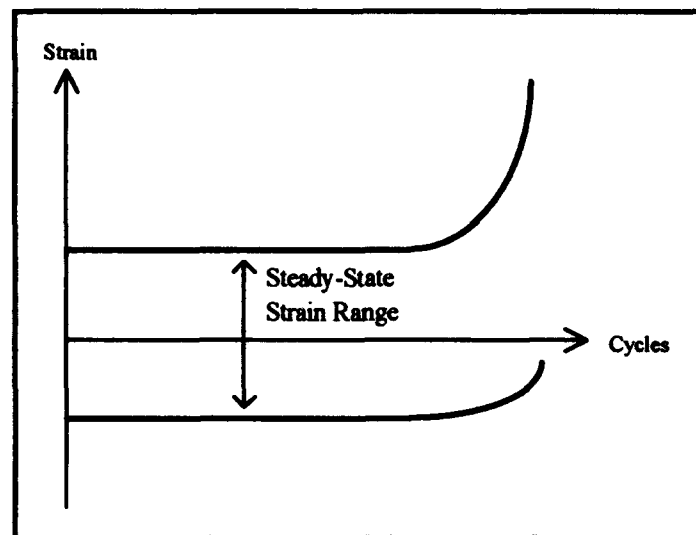
Figure 23. Steady-State Strain Range

The SN curve is divided into fatigue life regimes. Regime 1 includes the 600 MPa test which had a fiber-dominated failure. Regime 2a includes the next two tests, 445 and 300 MPa, which were mixed mode (fiber and matrix dominated) failures. Regime 2 consists of the 225 and 175 MPa tests; in which matrix cracking clearly dominated the failures and fiber cracking did not occur until just prior to specimen failure. No Regime 3

tests were observed. It is expected that if the applied stress is lowered sufficiently, a Regime 3 would exist for this material in which specimen failure would not occur.

The first cycle for four out of the five tests revealed a knee in the stress-strain curve at approximately 180 MPa due to the debonding of the 90° fibers. This value has also been reported as the knee of the static stress-strain curve by Baker (4:44). The initial and secondary moduli for the five tests are summarized in Table 2. The average stiffness reduction after the knee was 117.26 percent of the initial modulus, and the only specimen which did not display a knee was the lowest stress test, 175 MPa. This is expected, as the applied stress is lower than the knee. On the other end of the spectrum, the highest stress test, 600 MPa, underwent two changes in modulus, the second of which occurred at approximately 542 MPa and resulted in a 39.8 percent reduction from the initial modulus. This second knee corresponds to the onset of plasticity in the zero degree fibers. Newaz and Majumdar reported similar knees, at 200 and 650 MPa respectively (37).

Just as the reduction in stiffness during the first cycle indicates damage in the form of debonding, the reduction in stiffness during the remaining fatigue life of a specimen indicates deformation in the form of both damage and plasticity. As mentioned earlier, the stiffness degradation is a direct result of the strain increase, both of which depend on the

Table 2. TC RT: Initial, Secondary, and Third Moduli During First Cycle

Maximum Stress*	Initial Modulus,* (E_i)	Secondary Modulus (% reduction from E_i)	Third Modulus (% reduction from E_i)
175	125.4	N/A	N/A
225	129.6	107.9(16.7)	N/A
300	134.8	112.2(16.8)	N/A
445	135.4	117.9(12.4)	N/A
600	148.7	115.1(22.6)	89.5(39.8)
Average	134.8	113.3(17.3)	N/A
* All stresses are MPa, all Moduli are GPa			

51

applied stress. The normalized stiffness (E/E_i) and instantaneous percent strain are individually plotted versus cycles to failure in Figs. 24 and 25. Both the stiffness and percent strains are also plotted as a function of the normalized fatigue life (cycle/cycles to failure) in Figs. 26 and 27. These figures clearly indicate the point in the fatigue life at which drastic changes began to occur. Several observation can be made from these figures.

The history of the maximum and minimum strains during the fatigue life provides useful information about the MMC's response and damage mechanisms during the test (35:96). The magnitude of the difference between the two strains (the strain range) is an indication of the stiffness of the material. If the strain range remains constant, this indicates that no permanent damage, and thus, no appreciable change in stiffness, has occurred. Conversely, if the strain range continually increases, or "ratchets," this is an indication that damage is accumulating within the specimen in the form of fiber breaking, matrix cracking, or both. As the strains begin to increase with more cycles, more of the applied load is transferred to the fibers from the damaged matrix until this increased fiber stress causes the initiation and accumulation of fiber breakage leading to failure (35:97).

The number of cycles over which this strain increase and stiffness decrease takes place is dependent upon the magnitude of the applied load. It is generally understood that in the low cycle, high stress portion of the SN curve, fatigue failure is fiber-dominated. In this region, the rapid increase in strain, and the associated decrease in stiffness take only a few hundred cycles, a small portion of the total fatigue life. This type of behavior is seen, to varying degrees, in the 600, 445, and 300 MPa strain and stiffness responses. In all cases, the fiber failure does not initially translate to changes in stiffness until the final portion of the fatigue life. However, damage accumulation is more gradual at the two lower stress levels, and can be attributed to the matrix cracking within the 445 and 300 MPa specimens, which was not present in the 600 MPa specimen.
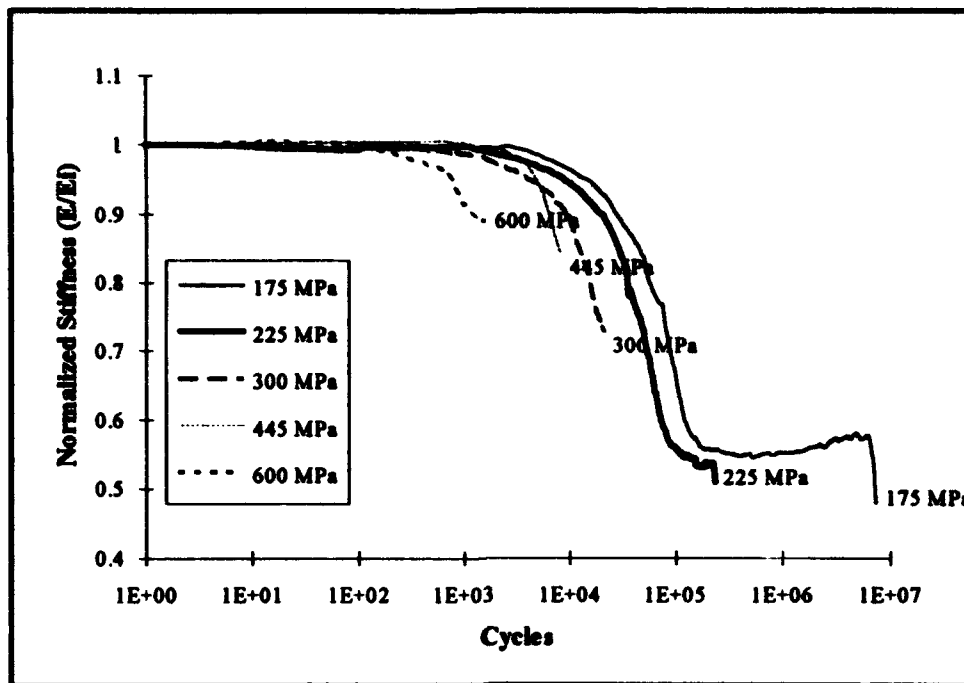
Figure 24. TC RT: Stiffness Reduction vs. Fatigue Cycles
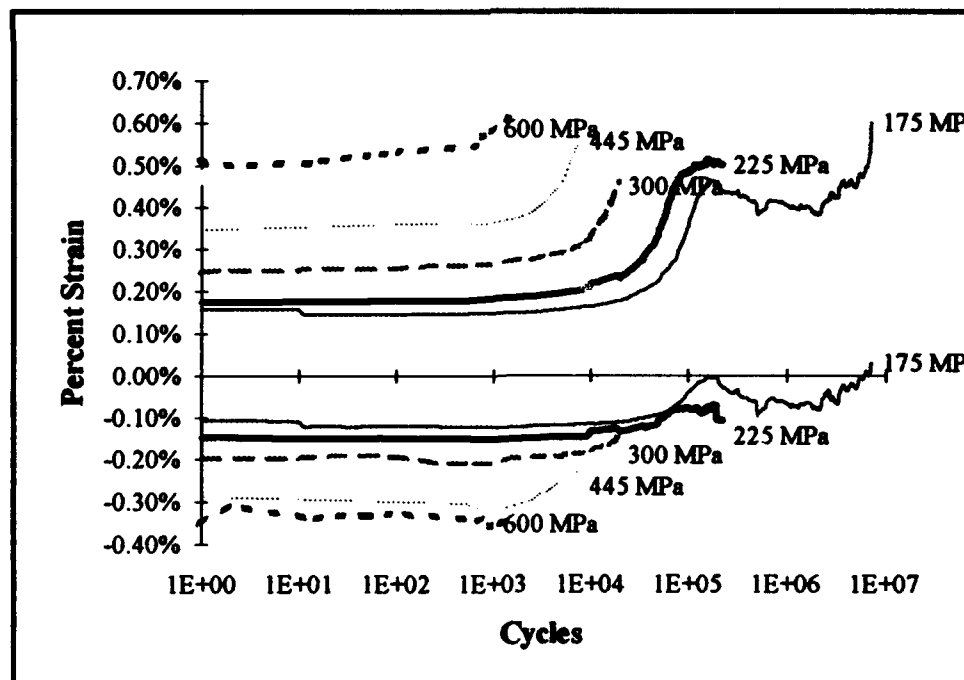
Figure 25. TC RT: Percent Strain vs. Fatigue Cycles
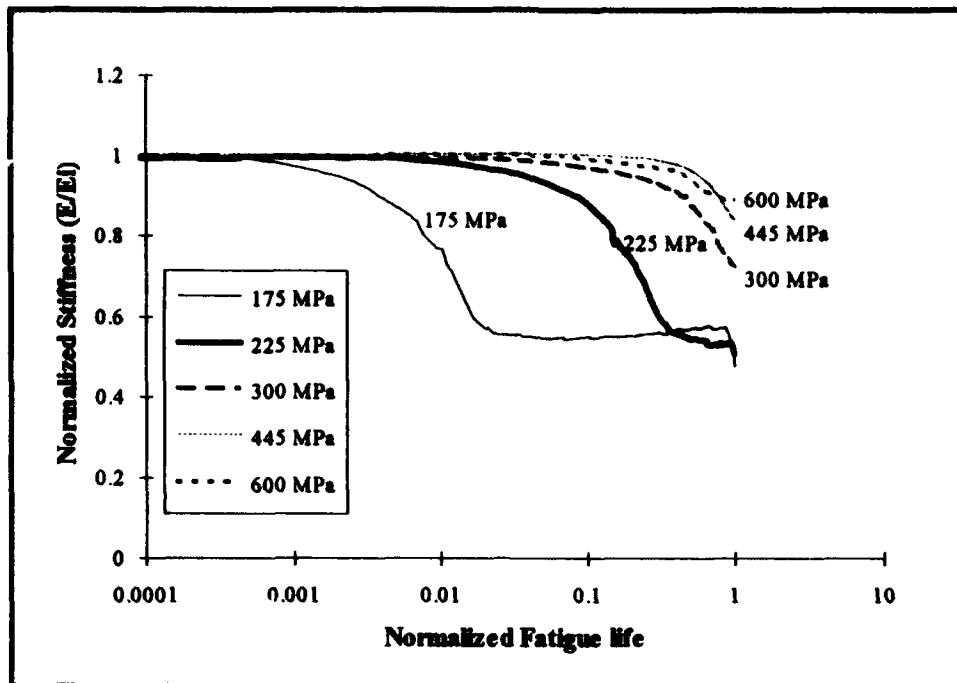
Figure 26. TC RT: Normalized Stiffness vs. Normalized Fatigue Life
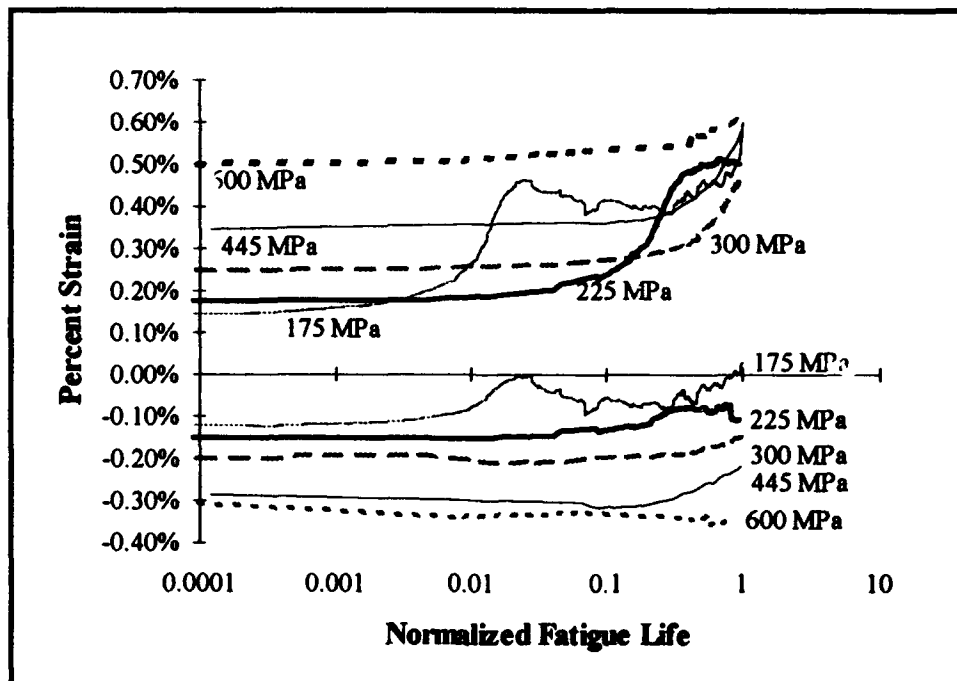
Figure 27. TC RT: Percent Strain vs. Normalized Fatigue Life

54

In contrast to the mixed-mode failure experienced by the 445 and 300 MPa specimens, the 225 and 175 MPa specimens appear to have experienced totally matrix-dominated failures. On a percent life basis, the decrease in stiffness, and the associated increase in strain, began much earlier for these tests. Additionally, the stiffness and strain in both tests stabilized, not changing appreciably for a significant portion of the respective fatigue lives, indicating that although significant matrix cracking had occurred, the applied stress was not large enough to fracture the fibers. The shorter stiffness and strain plateaus for the 225 case indicates that the applied stress was just high enough to cause fiber failure earlier in the specimen life than that for the 175 MPa applied stress. This behavior is similar to the Critical Damage State (CDS) introduced by Talreja for polymeric composites (49:176). He explains that matrix cracking in off axis plies increases with load cycles until a saturation state ensues, wherein a stable crack pattern develops. It is only when stress concentrations caused by the cracks become great enough to cause damage to the longitudinal fibers that failure occurs.

The similarity between the stiffness response for the two lowest stress cases is further illustrated by plotting a modified response for the 175 TC RT case (Fig. 28). The modification is made by removing the portion of the plateau in which no appreciable change occurred, from cycle 500,000 to failure. The similarity of the two stiffness responses indicates similar dominant damage mechanisms in both cases.
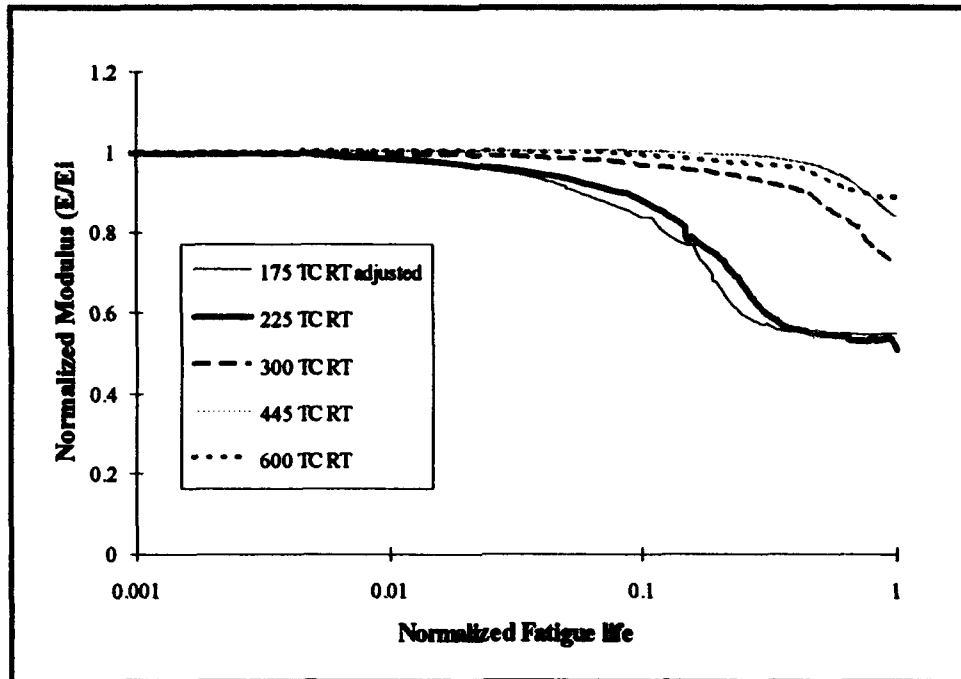
Figure 28. TC RT: Modified Stiffness Reduction vs. Fatigue Cycles

TC RT Micro-mechanic Evaluation

Regime 1 Test: 600 MPa. This highest stress level test was clearly a Regime 1 failure. With a very short fatigue life of 1,610 cycles, micro-mechanic deformation was dominated by fiber failure and matrix plasticity. The edge replica evaluation reflected that the 90° fibers debonded during the first cycle. Halfway through the cyclic life, numerous 0° fibers had also debonded and broken, and reaction zone cracks had formed on the 90° fibers, which then nucleated plasticity in the form of slip bands. Additionally, the 0° fiber breaks caused the very limited amount of matrix cracking. Figure 29 illustrates a longitudinally debonded, broken 0° fiber which has caused a matrix crack.

Examination of sectioned specimens reinforced the damage progression as seen in the edge replica evaluation. In addition, the post heat treatment, which was performed after testing and prior to sectioning, highlighted the areas and extent of plasticity *within* the specimen. This post heat treatment causes the very fine α phase of the matrix to
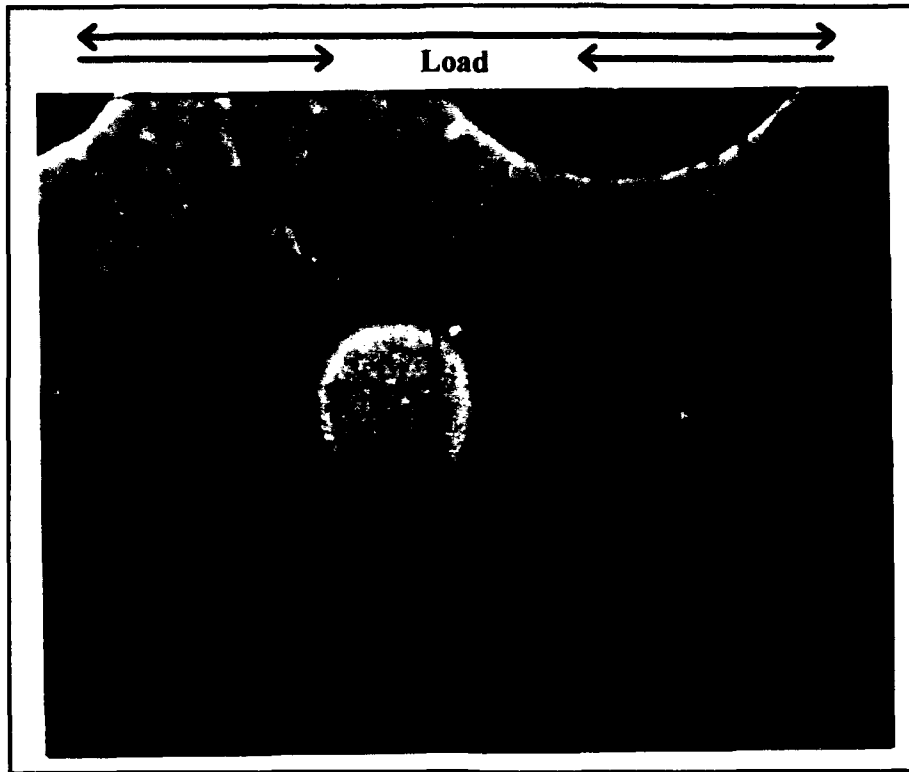
Figure 29. 600 TC RT: Debonded, Broken 0° Fiber Causes Matrix Cracking (200x)

precipitate in areas of dislocations. When etched, the α phase becomes white in color, while the beta phase becomes a dark brown. Thus, areas of plasticity become more evident.

The etched sectioned specimens revealed that damage initiated with debonding of the 90° fibers, followed by the formation of reaction zone cracks. These rzcs either nucleated slip bands, matrix cracks, or both. Figure 30 displays debonding and reaction zone cracks in both 0° and 90° fibers. Additionally, the 90° fiber rzcs have caused matrix cracks which are surrounded by slip bands, and the 0° rzcs have nucleated slip bands in the absence of matrix cracks.

Although slip bands predominately nucleated at rzcs, they were also observed within the large β grains very near the fracture surface. In general, slip bands form within a grain by dislocation movement along the preferred slip planes. These dislocations pile up at the
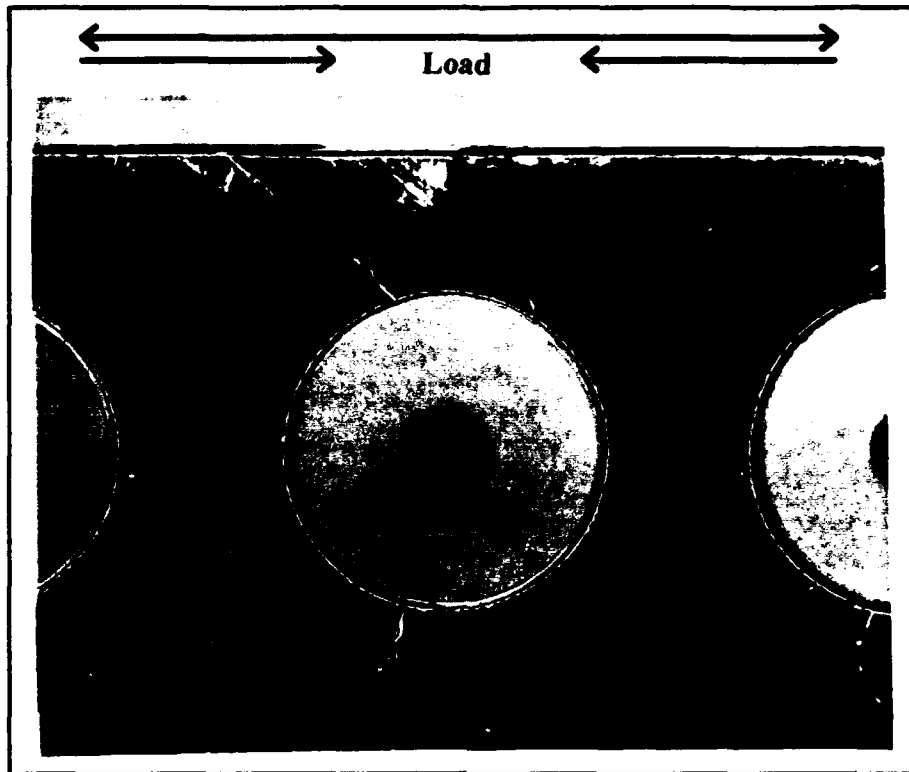
Figure 30. 600 TC RT: Debonded Fibers, RZCs, and Slip Bands (300x)

grain boundaries, and with increasing strain, can nucleate matrix cracking. The existence

of these intergranular slip bands in this test indicates that gross matrix plasticity occurred

within the matrix near the fracture surface, and was not isolated to the area directly

surrounding the fibers (Fig. 31). Majumdar (29) also reported bulk plasticity of the matrix

at a similar strain level in his unidirectional fatigue tests of SCS-6/Ti-15-3.

The etched sections also revealed an additional site of matrix plasticity. The

compressive loads caused a highly stressed area above and below the 90° fibers, resulting

in white regions above and below the 90° fibers (Fig. 32). This is a significant finding, as

it was not seen in the tension-tension specimens (see *TT RT Micro-mechanic Evaluation*
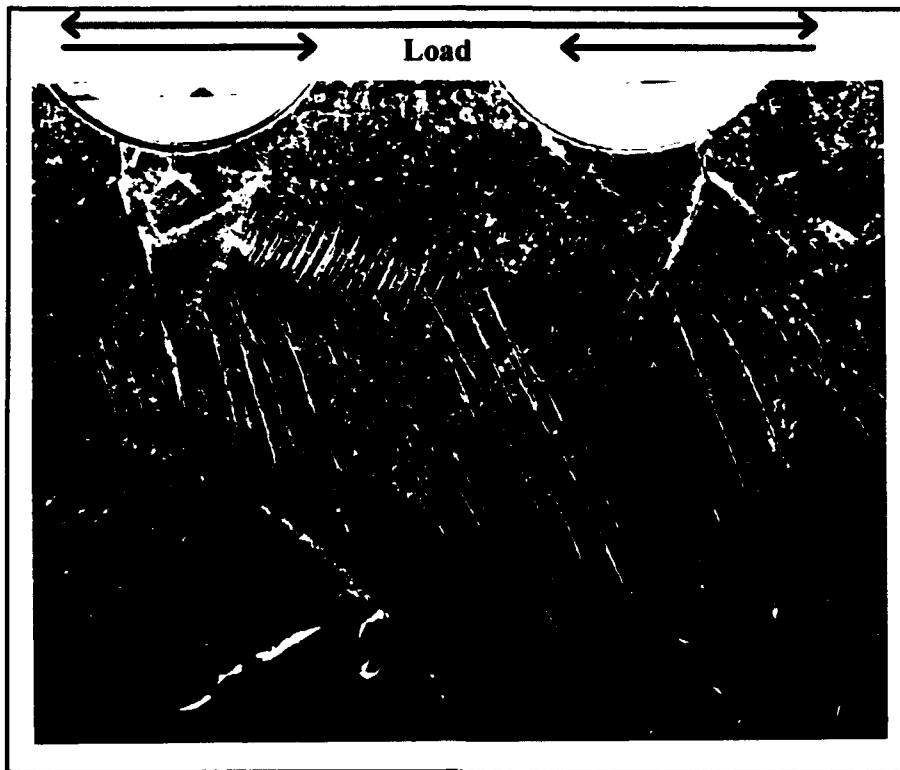
section).

Figure 31. 600 TC RT: Slip Bands Forming Within Beta Grains (300x)
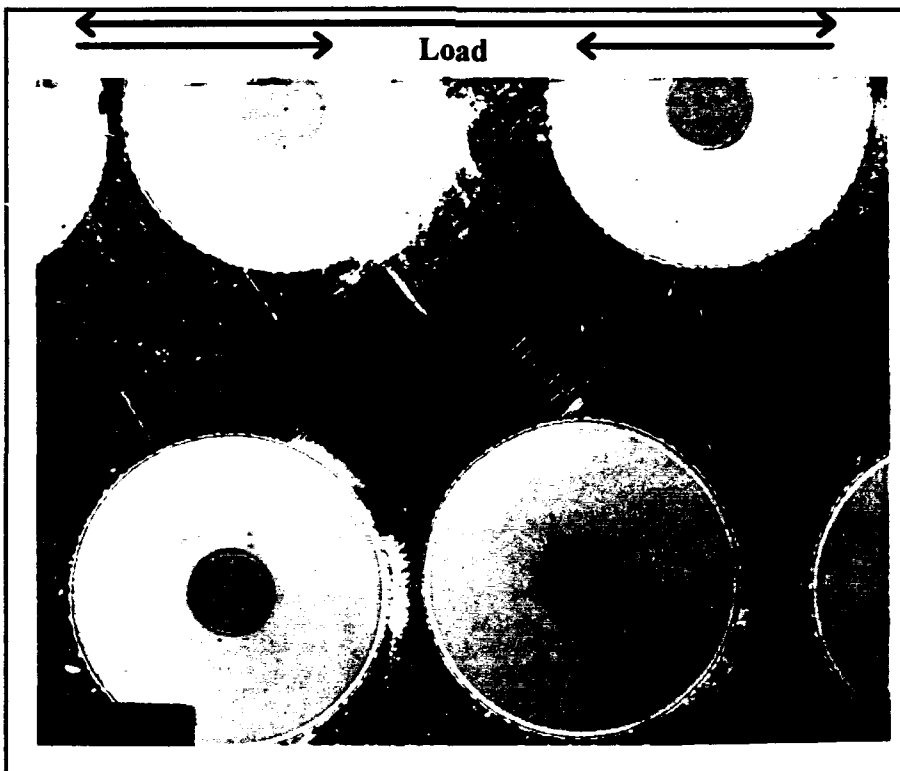
Figure 32. 600 TC RT: Matrix Plasticity Due to Compressive Load (300x)

The transverse section provided information which was not obtainable via the edge replica, which provided a longitudinal perspective. Almost all of the 0° fibers were debonded. Since the debonds were not due to impeding matrix cracks, it is evident that the very high compressive loads in this test caused the debonding.

Examination of the fracture surface revealed a combination of brittle cleavage and ductile void coalescence, the latter being more predominant. This highly dimpled surface (Fig. 33) is indicative of a fiber-dominated tensile overload type failure. Additionally, the fracture occurred on several different 90° layers within the specimen. This is due to the fact that the large amount of fiber failure which dominates Regime 1 occurs sporadically within the specimen, without regard to a certain plane. This is in direct contrast to a highly *matrix* dominated failure which usually occurs on the plane of the dominant matrix crack. The fracture surface also revealed that many of the 90° fibers were broken through the middle, indicating that the compressive loads caused radial fiber cracking.
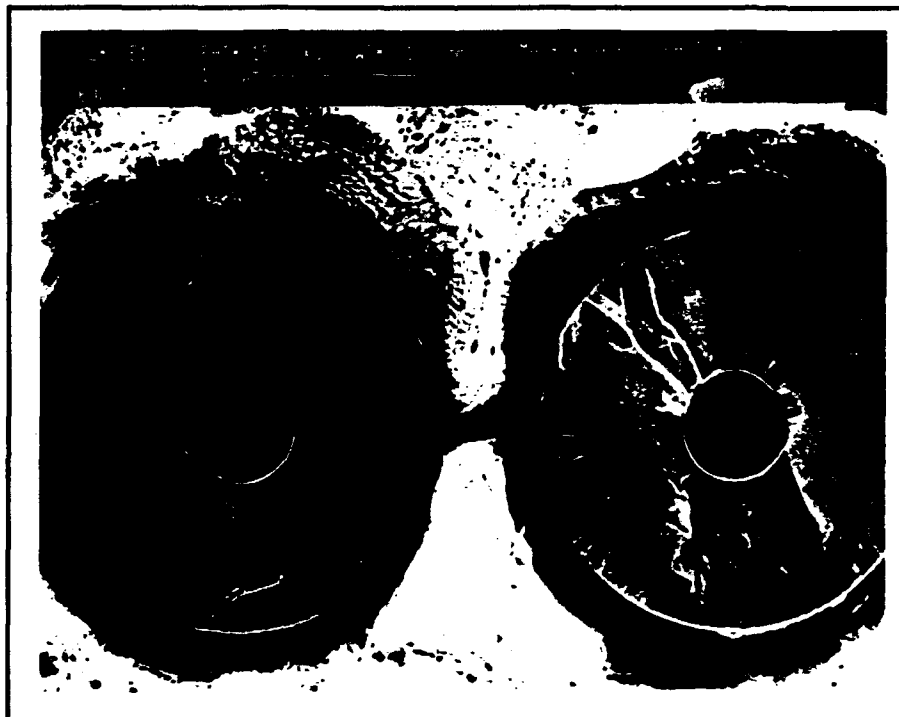
Figure 33. 600 TC RT: Fracture Surface (369x)

Regime 2a Tests: 445 and 300 MPa. Deformation in the Regime 2a tests displayed similar types of damage and plasticity as the Regime 1 test. However, because Regime 2a is a mixed damage mode regime, these tests were less fiber dominated and more matrix dominated. Thus, the extent of fiber-induced damage and matrix plasticity decreased, and the amount and length of the matrix cracks increased, as did the amount of matrix crack induced damage.

Edge replicas for the 300 MPa test revealed that at the point when the stiffness began to decrease (Fig. 26), matrix cracks formed. This occurred at approximately 1,000 cycles, or 4.5 percent of the fatigue life of the specimen. The cracks initiated at reaction zone cracks in both the 0° and 90° fibers (Fig. 34), although the 90° fiber rzcs were more prevalent. As the matrix cracks grew, the stiffness continued to decrease. At approximately 15,000 cycles, or 67.3 percent of the life, the matrix cracks which initiated at 90° fiber rzcs had grown all the way to a fiber in the next ply. As these cracks reached the next ply, they caused additional debonding of the 90° fibers and initial debonding of 0° fibers. They then grew around the fiber, not through it, and eventually grew to the next ply. This is referred to as *crack bridging*, and is illustrated in Fig. 35.

In this photomicrograph, the crack had initiated at a 90° fiber, progressed to the 0° fiber in the center, caused the debonding of the fiber/matrix interface, grew around the 0° fiber, and again grew into the matrix, continuing in this manner from ply to ply. The existence of crack bridging is significant, in that it has been found to cause the rate of crack growth to reach a steady-state value as a consequence of reductions in near-tip delta stress intensity factors (ΔK). This is induced by pressure on the crack faces by the bridging fibers (48:266). This apparent improvement in the resistance to fatigue crack growth is directly contrasted with the monotonically increasing fatigue crack growth in monolithic materials.

61
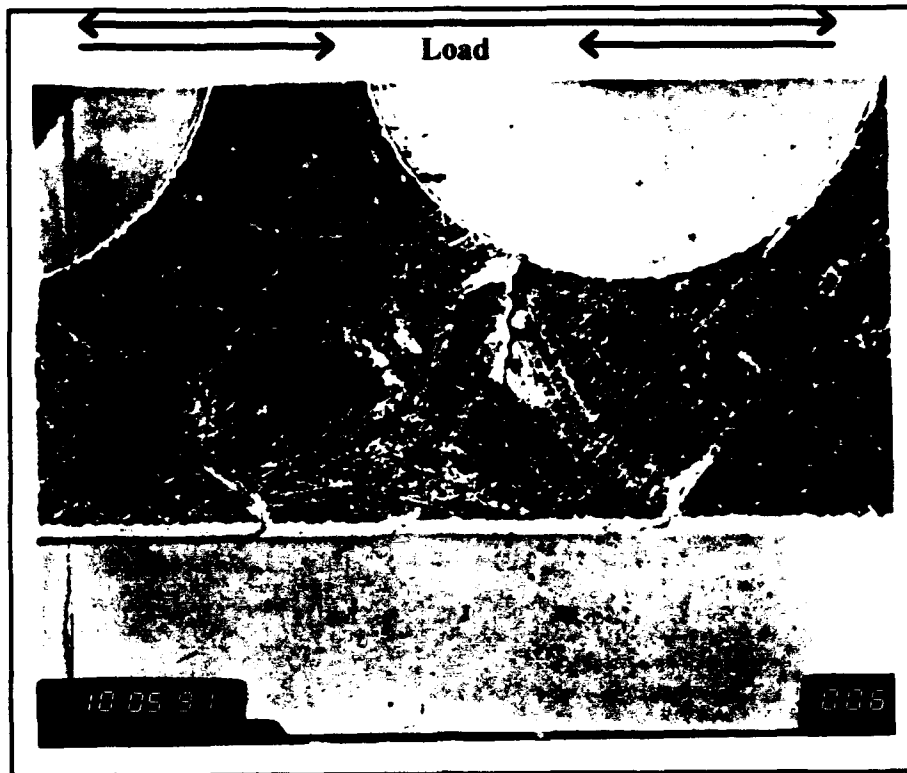
Figure 34. 445 TC RT: RZCs in Both 0° and 90° Fibers Initiate Matrix Cracks (500x)
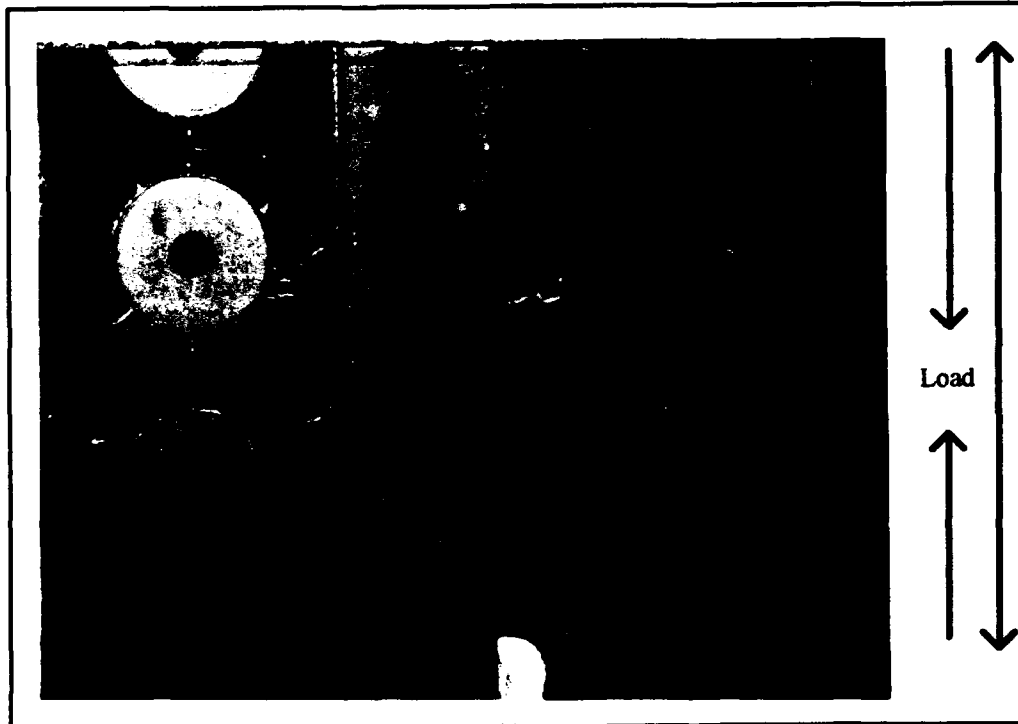
Figure 35. 300 TC RT: Crack Bridging Around a 0° Fiber (150x)

Matrix cracks continued to grow until specimen failure, which occurred in the area of many previously broken fibers. Some of the fiber breaks occurred within the first 1,000 cycles of the fatigue life, and then just before failure. This damage progression is expected to have been the same for the 445 MPa test; however, edge replicas were not taken.

The etched specimen sections revealed additional matrix crack induced damage which was not seen in the Regime 1 test. Matrix cracks were found to cause debonding in 0° fibers before they physically hit the fiber (Fig 36). This is due to the extremely high tensile stress ahead of the crack tip and the shear stress parallel to the fibers, which is caused by matrix plasticity ahead of the crack. This was also observed by Majumdar and Lerch in their unidirectional fatigue tests (30). Also shown in this picture is matrix plasticity in the form of slip bands formed by the mode 1 type fatigue crack (see *Fundamentals of Micromechanic Evaluation* section).
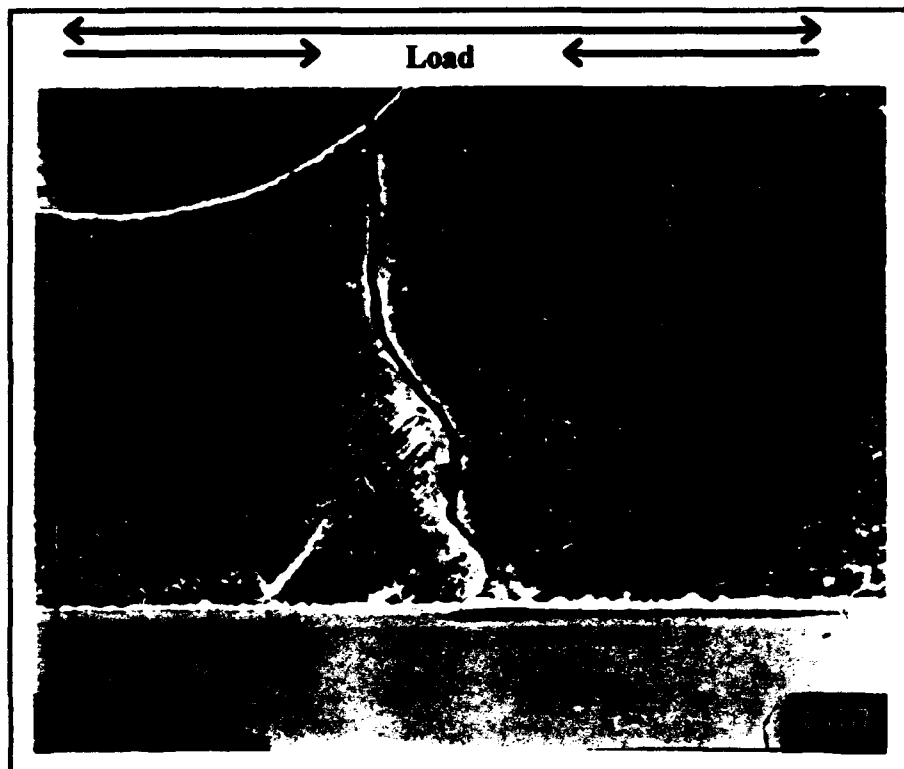
Figure 36. 445 TC RT: 0° Debond Caused by Incoming Matrix Crack (750x)

63

Fractographic analysis of the fracture surfaces also suggested a mixed mode failure, since both surfaces contained regions of brittle cleavage and ductile void coalescence. The 445 MPa fracture surface contained more of the fast fracture type of ductile void coalescence, while the 300 MPa contained less fast fracture and more brittle cleavage since matrix cracks were more prevalent in this lower stress test. Figure 37 illustrates this combination of failure modes, with a brittle cleavage area above the two 0° fibers, and a tensile overload region below it.

Further examination of the fracture surface of the 445 MPa test also revealed that micro-buckling of the fibers may have occurred. In general, when fibrous composites are subjected to compressive stresses, the fibers act as long columns, and can buckle due to the compressive loads well before, or in the absence of, overall buckling of the specimen. Additionally, if these fibers have debonded from the matrix, they lose a significant amount of the strength and support it initially imparted. Added to this is the fact that in this test,

Figure 37. 445 TC RT: Brittle Cleavage and Ductile Void Coalescence (300x)

as the specimen was fatigued, the matrix cracks grew and never fully closed, evidenced by the decreasing negative strain value throughout the life of the specimen (Fig 25). Thus, as the compressive load was applied to the specimen, the fibers in the vicinity of the dominant matrix crack were left unsupported, making buckling possible. Figure 38 shows several 0° fibers which have been forced into the surrounding matrix. It is possible that this was due to fiber micro-buckling. However, since micro-buckling of the 0° fibers was not observed on the longitudinal section, it may also be possible that the specimen merely failed during the compression portion of the fatigue cycle, which would cause the fibers to be pushed into the surrounding matrix.

Regime 2 Tests: 225 and 175 MPa. These lowest stress level tests were clearly Regime 2 failures. With long fatigue lives of 287,096 and 7,287,536 cycles respectively, micro-mechanic deformation was dominated by matrix cracking. Although there is a
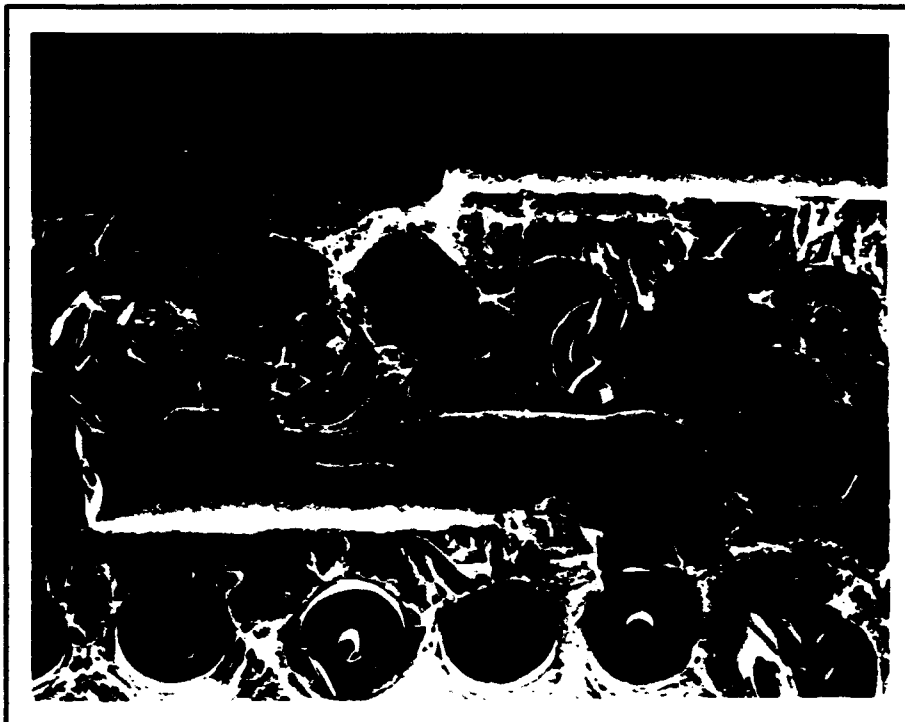
Figure 38. 445 TC RT: Micro-buckling of 0° Fibers (100x)

significant difference between these two fatigue lives, the micro-mechanic deformation mechanisms were very similar. The main difference is the duration of the stiffness and strain plateau experienced by both specimens. The 175 MPa specimen experienced the plateau for the last 97 percent of its fatigue life, while the 225 MPa specimen experienced it for the last 65 percent of its life (Figs 26 and 27). It is postulated that the higher stress level caused fiber failure earlier in the 225 MPa fatigue life, thus resulting in a shorter plateau than that experienced by the 175 MPa specimen.

Edge replica evaluation revealed that, as seen in all the tension-compression tests, matrix cracks began at 90° fiber rzcs. The matrix cracking began at 0.3 and 1.74 percent of the 175 and 225 MPa specimen fatigue lives, respectively, and continued to grow, bridging approximately five plies at 1.37 and 12 percent of the respective fatigue lives. By the beginning of the stiffness and strain plateaus, cracks in both specimens bridged an average of six to eight plies, with a few shorter cracks bridging only two to three plies. Additionally, during both the 175 and 225 MPa stiffness plateaus, the amount of matrix cracks did not appear to change. Thus, the extent of matrix cracking on the specimen edges shown in Fig. 39 was essentially the same for last 97 percent of the 175 MPa specimen life. No fiber breaks were observed due to these cracks; as seen in the Regime 2a tests, the 0° fibers were left intact in the wake of matrix cracks. A few 0° fibers failed in the initial 1,000 cycles of both tests; it is expected that these fibers were previously flawed, thus breaking under the applied stress.

Sectioned specimen evaluation revealed that the same deformation mechanisms observed on specimen edges occurred within the specimen. Additionally, matrix plasticity was seen in the form of slip bands. These slip bands formed in the vicinity of matrix cracks, as seen in both Regimes 1 and 2a, however, they were much finer and closer together in these Regime 2 specimens. Figure 40 shows these slip bands emanating from a 90° rzc induced matrix crack which has grown to the adjacent 0° fiber.
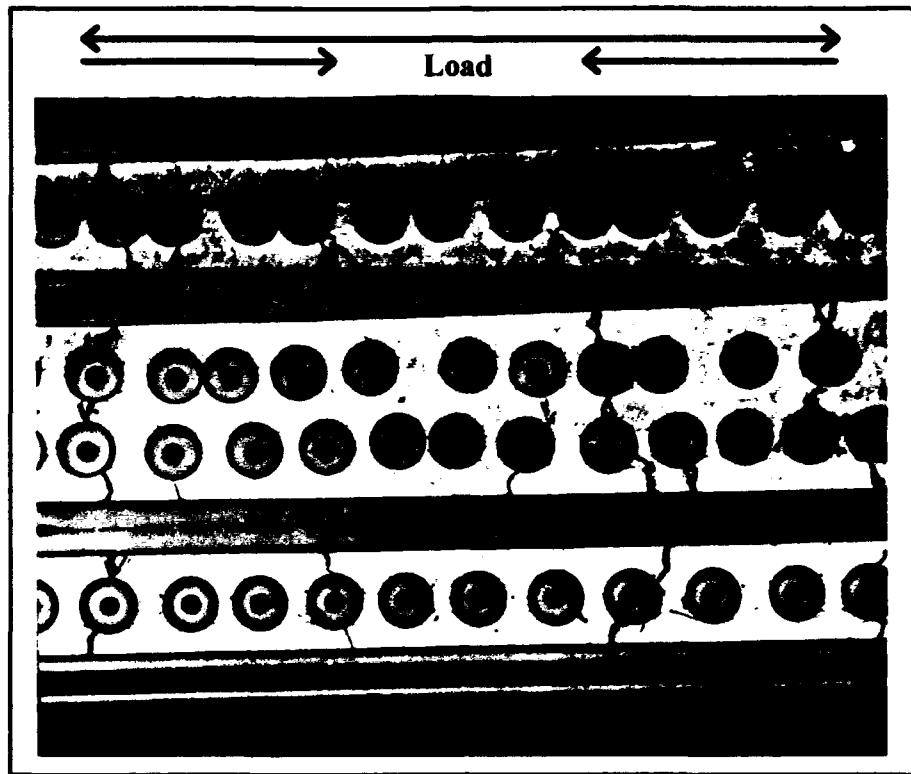
Figure 39. 175 TC RT: Specimen Edge After Failure (50x)
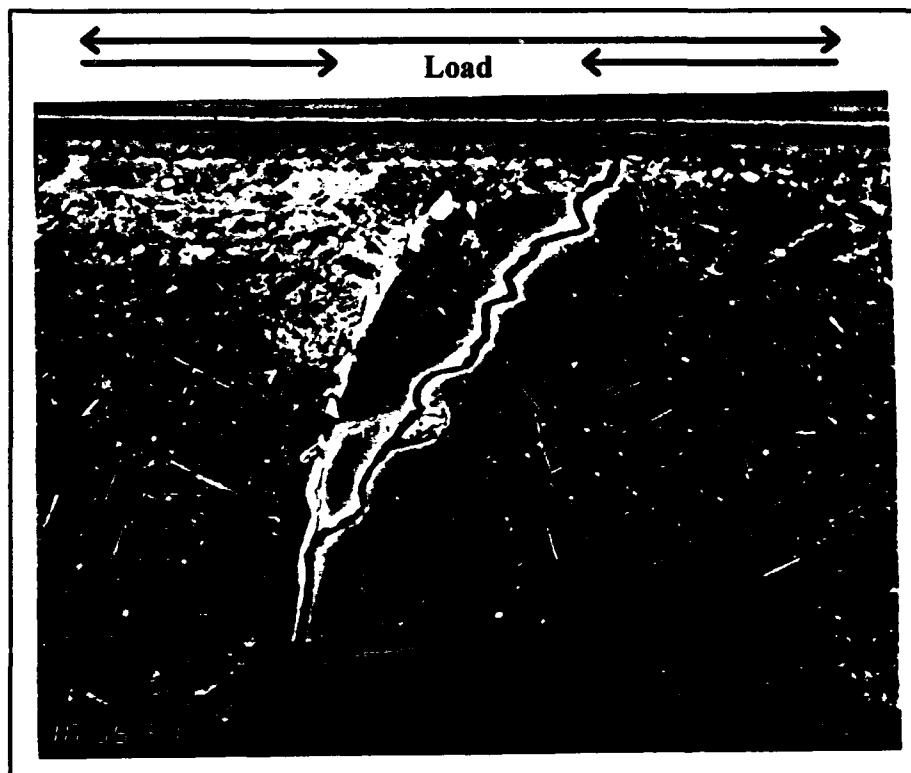
Figure 40. 175 TC RT: Slip Bands Emanating From a Matrix Crack (752x)

The fracture of both of these specimens occurred along a single 90° ply, with the brittle cleavage type surface indicative of a matrix-dominated failure. Additionally, the 90° fibers cleanly separated, indicating that they had debonded (Fig 41). The surfaces were flat, with fatigue striations emanating from the 90° fibers. These striations are caused by the continual opening and closing of the matrix cracks (see *Fundamentals of Micro-mechanic Evaluation* section). Of particular interest is the highly faceted and crystallographic morphology of the 175 MPa specimen fracture surface. Figure 42 shows that, although the fracture occurred along one 90° ply, matrix cracks and slip planes occurred at many different levels. The areas just above the two 90° fibers are fatigue striations resulting from two separate matrix cracks which propagated along two different planes. However, the middle region is much more crystallographic and results from separation along the slip planes that emerged from the numerous matrix cracks. Figure 43 is a close-up of the area between the two striation regions; one can see that this crystallographic surface morphology is merely a three dimensional result of two dimensional slip bands. Skelton has reported that materials which show planar slip behavior, like Ti-15-3, usually display this crystallographically faceted mode of propagation, particularly at low ΔK (46:205).

Additionally, this highly faceted surface has also been reported in titanium alloys by several other researchers (38-48). They reported that below some critical delta stress intensity factor (ΔK) level, a highly faceted fracture surface appearance developed, whereas, above this level, the fracture surface became much smoother overall and was covered with fatigue striations. In each case, it was believed that the fracture mechanism causing this faceted surface could be correlated to the development of a reversed plastic zone size equal to the grain size of the controlling phase in the alloy micro-structure.

The initial plastic zone is developed during loading by the application of a stress intensity factor K_1. When the direction of loading is reversed, this stress intensity factor is reduced by the value h_k; the reduced level corresponds to a stress intensity level of K_2.
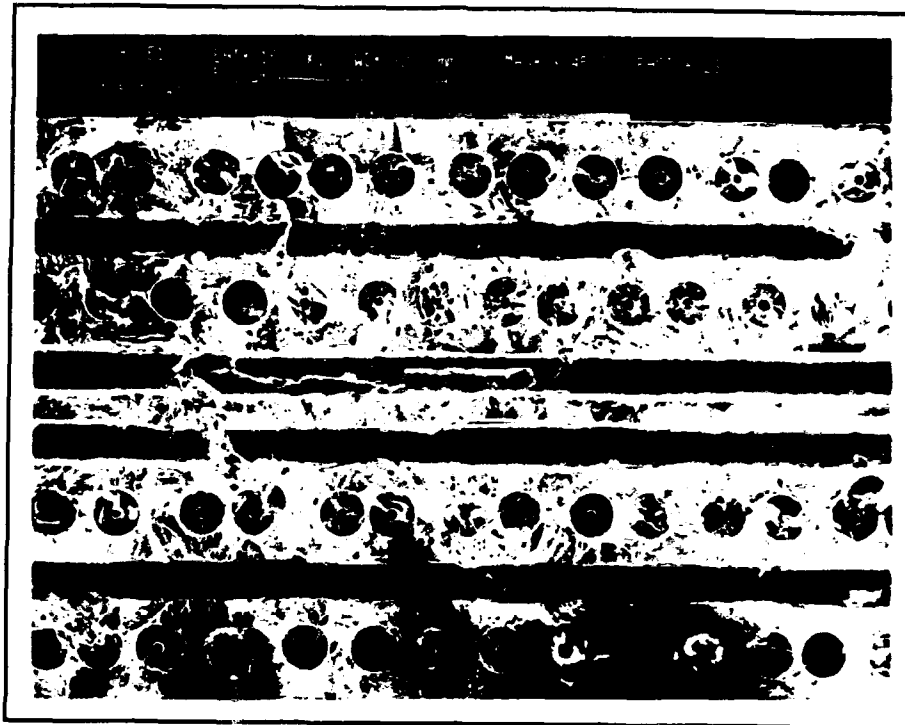
Figure 41. 175 TC RT: Fracture Surface (45x)

Figure 42. 175 TC RT: Striations and Crystallographic Facets (250x)

Figure 43.   175 TC RT: Close-up of Faceted Surface (750x)

Because the elastic stress distribution which was associated with K_I was truncated at the σ_{ys} by local yielding, the subtraction of an elastic stress distribution in going from K_1 to K_2 causes the final crack tip stress field to drop into compression. At K_2, a smaller plastic zone is formed in which the material experiences compressive yielding (16:533). These two plastic zones are illustrated in Fig. 44. Paris (38:104) quantified the resulting smaller plastic zone by replacing K with h_k, and σ_{ys} with $2\sigma_{ys}$ in Equation 2, resulting in Equation 3.

$$r_y \approx \frac{1}{2\pi} \frac{K^2}{\sigma_{ys}^2} \tag{2}$$

$$r_y = \frac{1}{8\pi} \left(\frac{h_k}{\sigma_{ys}} \right)^2 \tag{3}$$
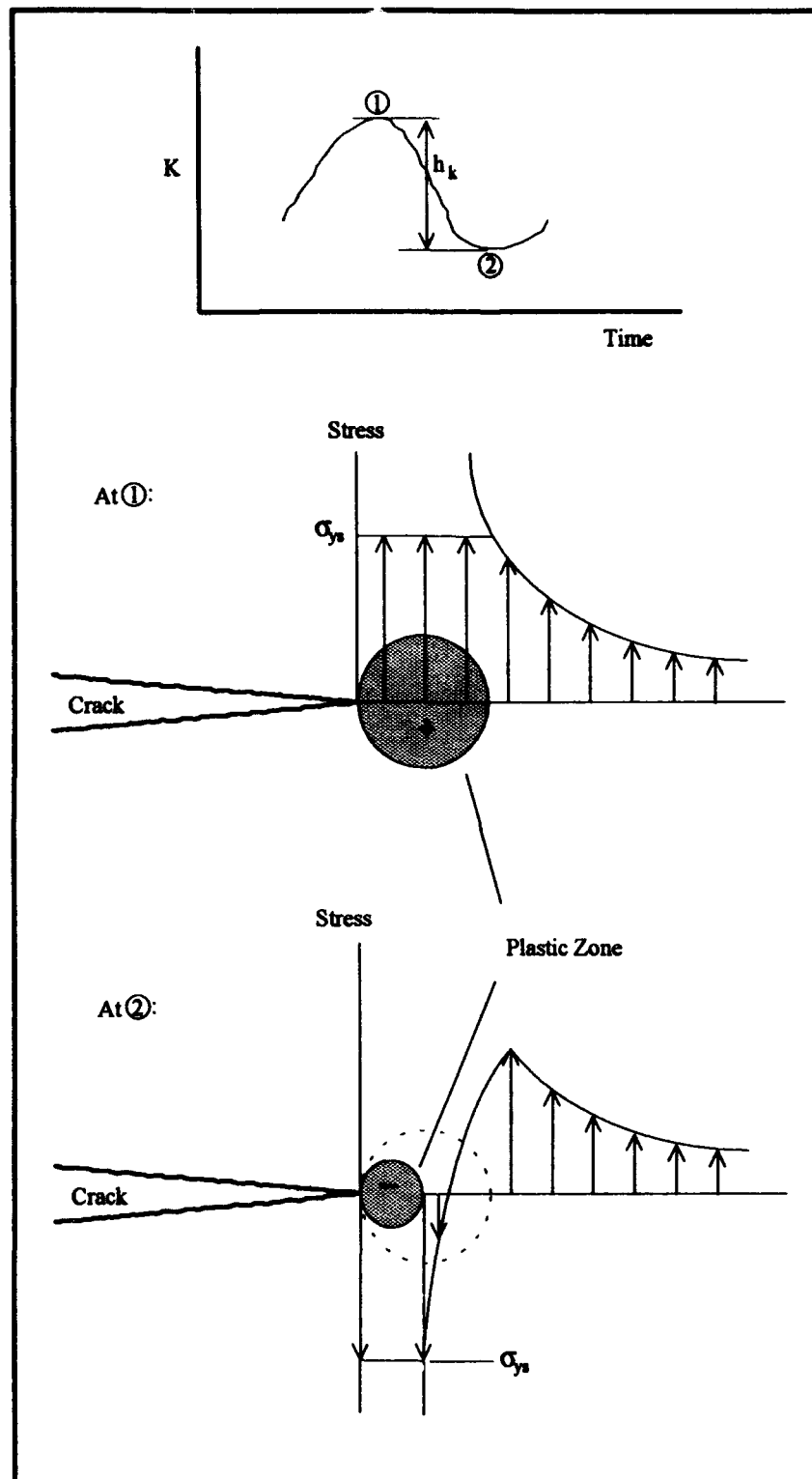
Figure 44. Reversed Plastic Zone Development

Suresh also reported the existence of a fatigue crack growth threshold which results in this highly crystallographic and faceted fracture surface (48:205). He refers McClintock (1963), who used the criterion that fatigue crack growth occurs when a critical value of local strain or accumulated damage over certain characteristic distance ahead of the crack tip reaches a critical value. Using an elastic-plastic analysis, McClintock stated that fatigue cracks may cease to advance when the extent of near-tip plasticity becomes comparable to some characteristic micro structural size scale.

The above discussion, coupled with the current research, may explain the apparent lack of fatigue crack growth during the last 97 percent of the 175 MPa specimen's fatigue life. Thus, it is postulated that the combination of striation and faceted/crystallographic regions on the fracture surface, and the stiffness and strain plateaus for this specimen support the conclusion that the critical value of crack tip stress intensity factor was reached in many different regions of the failed specimen.

In summary, the deformation mechanisms differed for the three observed regimes of the SN curve, although the general progression of deformation remained very similar. The Regime 1 test was fiber dominated and experienced extensive matrix plasticity. The Regime 2a tests were mixed mode failures characterized by both fiber and matrix dominated failure, and experienced less matrix plasticity than the Regime 1 test. The Regime 2 tests were highly matrix dominated and experienced less matrix plasticity than both the regime 1 and 2a tests.

TT RT Macro-mechanic Evaluation

A rectangular specimen geometry similar to that used for the TC RT tests was used for the TT RT tests (Fig. 21). The majority of the failures occurred within the gage length, with some failing closer to the tabs.

Stress, strain, fatigue life, modulus degradation, and dominant failure modes for the tension-tension tests are summarized in Table 3, and the fatigue life data is plotted on a maximum applied stress basis in Fig. 45. Note that for this tension-tension fatigue (R-ratio = 0.1), the *stress range (delta stress)* is 90 percent the maximum applied stress. Thus, plotting the stress range versus cycles to failure results in shifting the fatigue life curve down and to the left. This is not of major consequence in this section, or when comparing fatigue data generated at the same R-ratio, however it will come into play when comparing data generated at different R-ratios, or different loading conditions. The *strain range* found in Table 3 is defined as the magnitude of the difference between the maximum and minimum strains during the steady state strain portion of the fatigue life.

Table 3. TT RT: Macro-mechanic Results Summary

Max Stress (MPa)	Stress Range (MPa)	Max Strain (%)	Strain Range (%)	Regime of Failure	Cycles to Failure	Percent of Initial Strain at Failure $(\varepsilon_{fail}/\varepsilon_i)*100$	Percent of Initial Modulus at Failure $(E_f/E)*100$	Dominant Failure Modes
200	180	0.172	0.148	3	> 9.8 E6	$\cong 100$	$\cong 100$	mp (minor)
250	225	0.603	0.175	2	1,912,010	153.64	61.7	mc (extensive), mp
300	270	0.656	0.238	2	646,253	258	56.5	mc (extensive), mp (extensive)
450	405	0.559	0.326	2a	40,556	135	90.8	mc (some), mp (some), ff
600	540	0.581	0.430	1	4,419	121	90.6	mc (very short) mp (extensive), db: Longitudinal ff (extensive)
* mc = matrix cracking, mp = matrix plasticity, ff = fiber failure, db = debond								

73
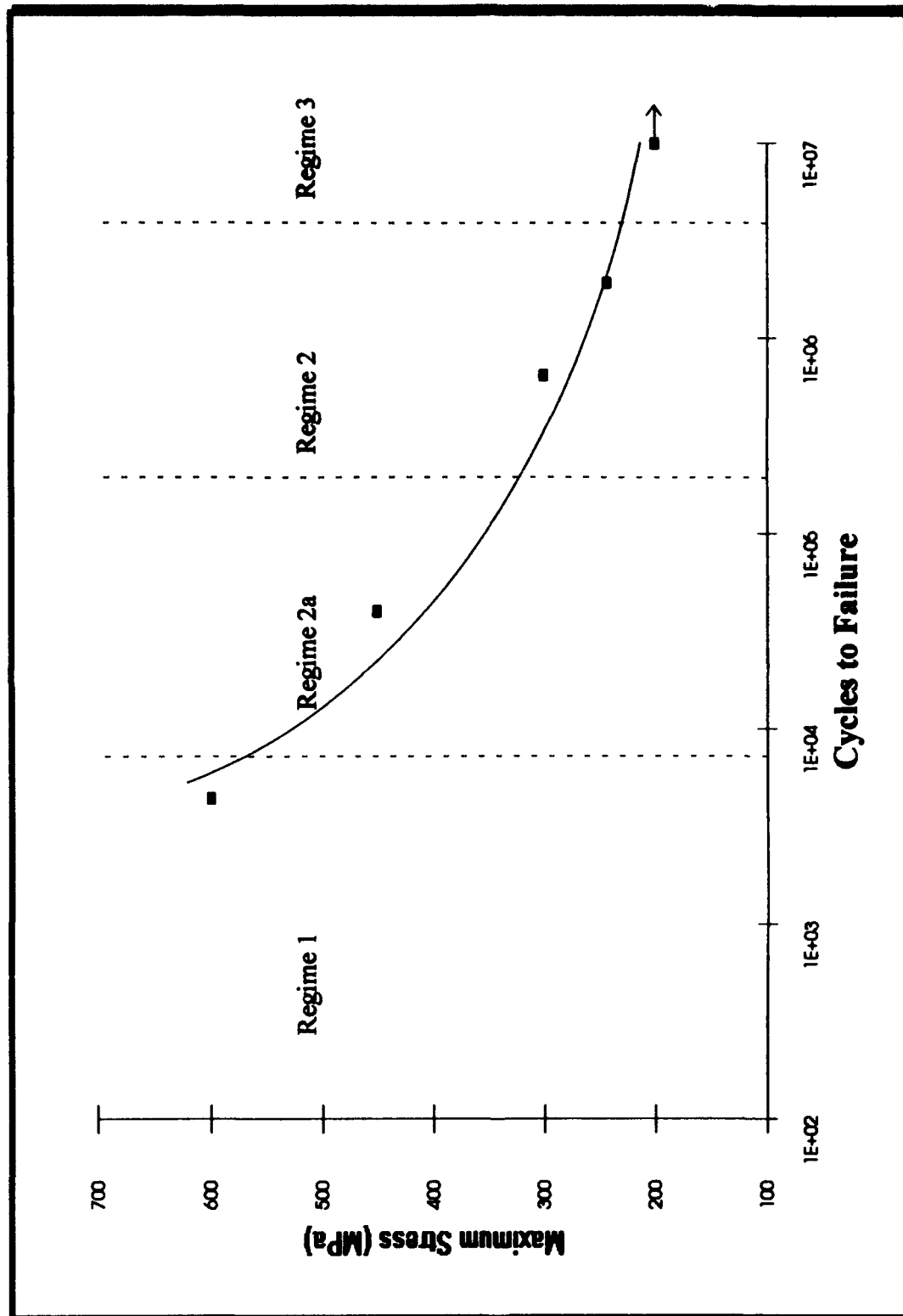
Figure 45. TT RT: SN Curve

74

In each test, the knee of the stress-strain curve was evident at approximately 180 MPa. The exact values for the initial, secondary, and third moduli, as applicable for each specimen, are found in Table 4. The average initial stiffness for the five tests was 130.99 GPa. Just as seen in the TC RT tests, the only specimen to reveal a third reduction in modulus was the 600 MPa specimen; this second knee occurred at 543 MPa, primarily due to onset of plasticity of the matrix.

As mentioned earlier, indicators of damage within the specimen include the changes in stiffness and strain throughout the fatigue life. For this reason, the normalized stiffness and percent strain are plotted versus cycles to failure and percent of fatigue life, in Figs. 46 through 49, respectively. These figures reveal four different shapes of both the stiffness and strain curves. The stiffness and strain curves for the 600 MPa specimen reveal that no "steady state" condition is evident for either parameter. The stiffness curve displays a continually increasing negative slope beginning at cycle 1, while the strain curve displays a continually increasing positive slope. In contrast, the stiffness and strain for the 450 MPa specimen appear to remain constant for the initial 90 percent of the fatigue life, the curves then take on the same slope characteristics as do the 600 MPa curves; the difference is the percent of specimen life at which the changes take place.

Table 4. TT RT: Initial, Secondary, and Third Moduli During First Cycle

Maximum Stress*	Initial Modulus (E_i)	Secondary Modulus (% reduction from E_i)	Third Modulus (% reduction from E_i)
200	114.05	108.30 (5.04)	N/A
250	133.10	117.07 (12.04)	N/A
300	125.57	110.9 (11.68)	N/A
450	137.76	117.79 (14.49)	N/A
600	144.30	117.85 (18.32)	105.74 (26.72)
Average	130.99	114.38 (12.32)	N/A
* All stresses are MPa, all Moduli are GPa			
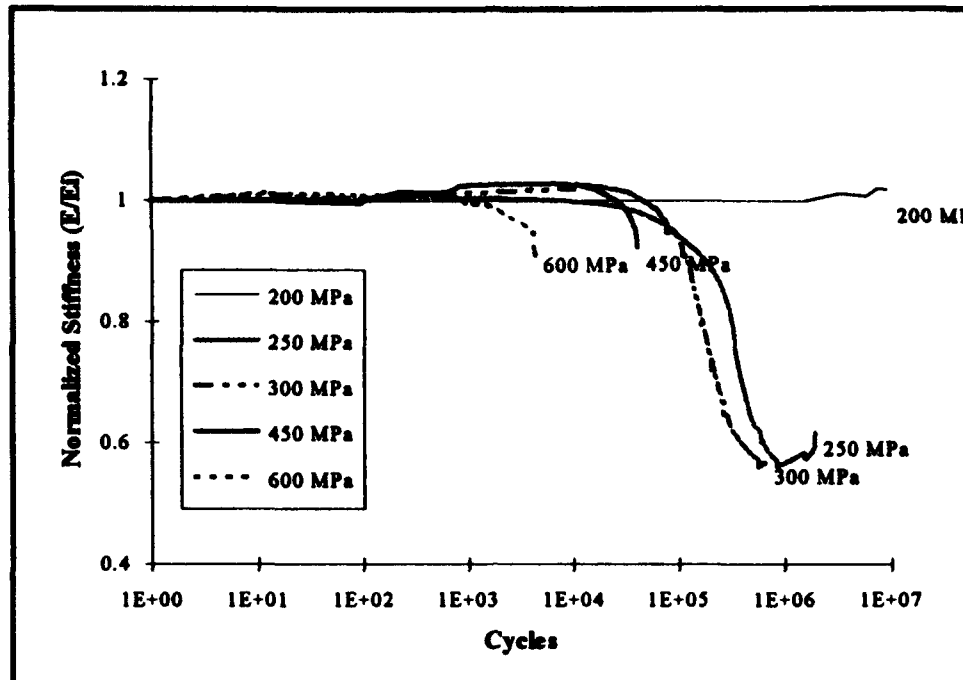
Figure 46. TT RT: Normalized Stiffness vs. Fatigue Cycles
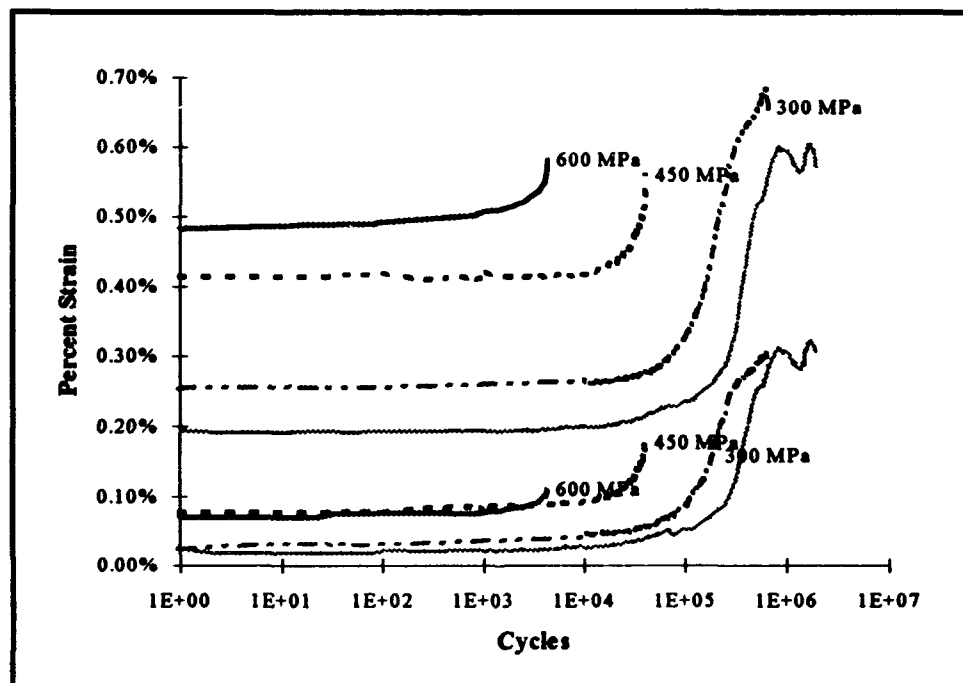
Figure 47. TT RT: Percent Strain vs. Fatigue Cycles

76
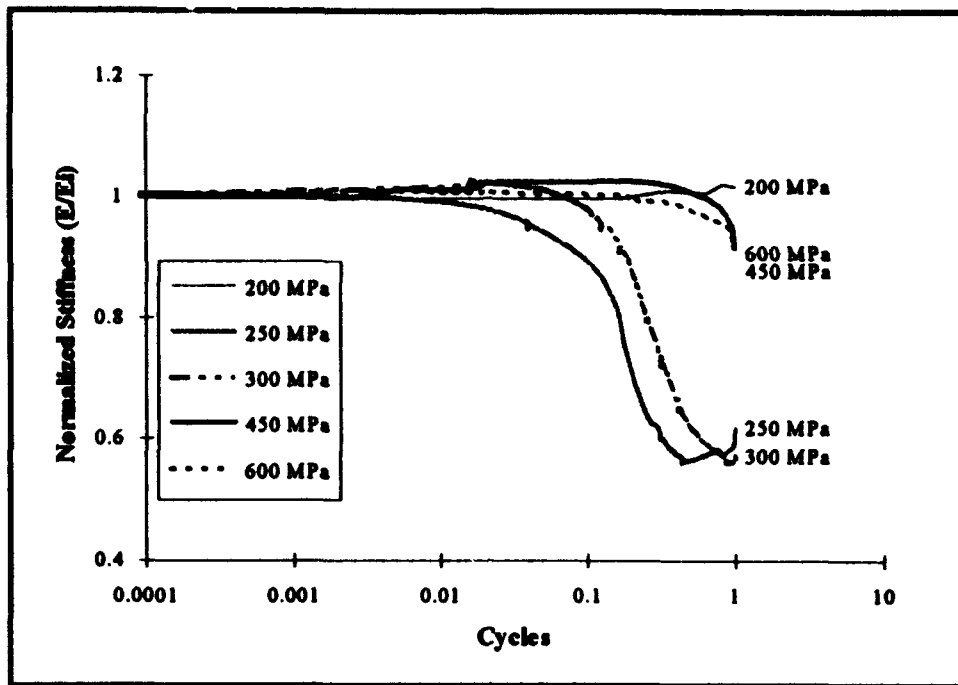
Figure 48. TT RT: Normalized Stiffness vs. Normalized Fatigue Life
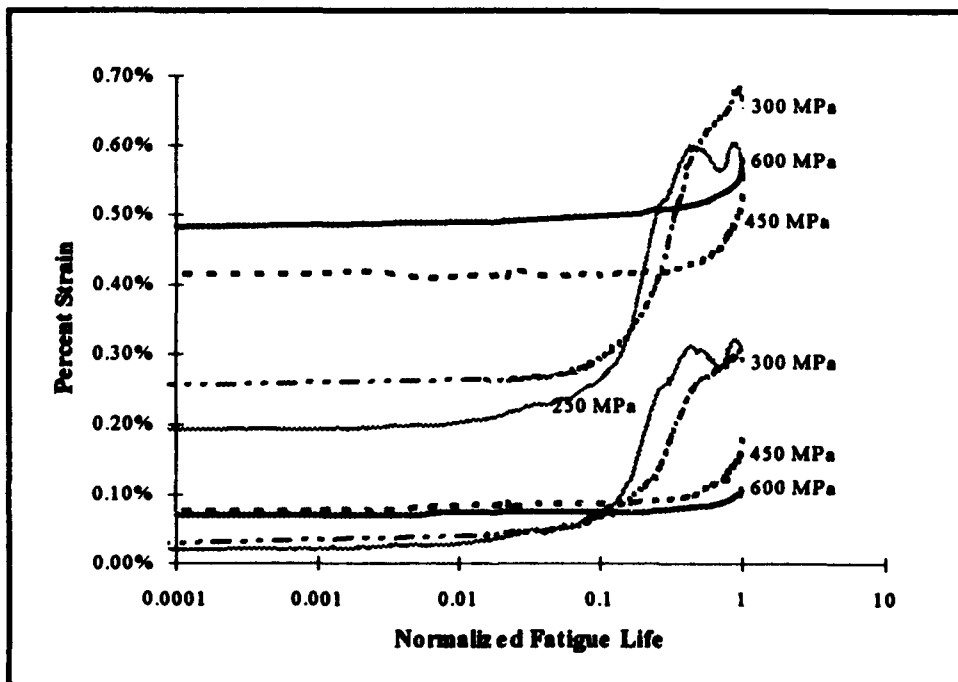
Figure 49. TT RT: Percent Strain vs. Normalized Fatigue Life

The 300 and 250 MPa specimens experienced this steady state stiffness and strain condition for the initial 1 and 0.5 percent of their fatigue lives, respectively. Beyond this, two major changes took place. In a manner similar to that of the 600 and 450 MPa specimens, the stiffness and strain began to decrease and increase, respectively. However, at 200,000 cycles (32 percent of the fatigue life), for the 300 MPa test the two curves experienced a point of inflection, meaning that the stiffness continued to decrease, but at a much slower rate. Thus, the curve began to level off just before failure. The strain curve behaved similarly, also appearing to level off. This point of inflection also occurred for the 250 MPa test at 400,000 cycles (20 percent of fatigue life). The strain curves for the 250 MPa specimen experienced a dip at approximately 1 million cycles. This is expected to be due to an eccentricity in the crack length.

The 200 MPa specimen behaved differently than any of the previously mentioned specimens. Although the modulus did experience a 5.3 percent reduction during the first fatigue cycle, it did not continue to decrease at any point throughout the fatigue life. In fact, during the last 90 percent of the fatigue life, the modulus actually increased by approximately 1.7 percent. Additionally, the strain decreased slightly. Of particular interest is that the test was stopped, before failure, at approximately 10 million cycles, or 11 days of testing. It was concluded that since no significant changes in either stiffness or strain had occurred, this stress level was below the endurance limit for this material in this loading condition.

In addition to the shape changes in the stiffness and strain curves, the quantitative amount of modulus decrease and maximum strain increase over the life of the specimen can aid in the characterization of the type of failure. The 600 MPa specimen experienced a 10 percent decrease in modulus, and a 21 percent increase in strain. Although the 450 MPa specimen experienced approximately the same amount of modulus degradation, it experienced a significant amount of additional strain increase (35 percent). This, coupled

with the fact that the stiffness of 600 MPa specimen decreased continually over the fatigue life, in contrast to the delayed stiffness decrease of the 450 MPa specimen, indicates that the damage mechanisms for the two tests are different.

The 300 MPa specimen experienced drastic changes in stiffness and strain. The specimen underwent a 43.5 percent increase in modulus, and a 158 percent increase in strain. These values, coupled with the large portion of the specimen life in which they occurred, indicate that the failure mode for the specimen was dominated by matrix cracking.

The above discussion, in conjunction with the micro-mechanical discussion to follow, provide the information necessary to separate the four fatigue tests into the respective regimes of the SN curve. As summarized in Table 3, Regime 1 consists of the 600 MPa test, Regime 2a consists of the 450 MPa test, Regime 2 consists of the 300 and 250 MPa tests, and Regime 3 consists of the 200 MPa test.

TT RT Micro-mechanic Evaluation

Regime 1 Test: 600 MPa. This highest stress level test was clearly a Regime 1 failure. With a short fatigue life of 4,419 cycles, micromechanic deformation was dominated by fiber failure and matrix plasticity, while minor matrix cracking did occur just before specimen failure.

The edge replica evaluation reflected that debonding occurred during the initial cycle. At cycle 1,000, or 23 percent of the fatigue life, matrix plasticity began at the 0° fiber-matrix interface, growing more extensive until specimen failure. Matrix cracking was not detected until cycle 4,000 (90 percent of the fatigue life). The matrix cracks that did occur were extremely short, and grew perpendicular to the loading direction.

Examination of longitudinally sectioned specimens also revealed that both fiber breaking and matrix plasticity were the dominant failure modes for this test. The sections

showed that many of the 0° fibers were broken, however, none of the observed fiber breaks appeared to cause matrix cracking. The matrix cracking that did exist, without exception, nucleated at rzcs, and coexisted with matrix plasticity. Figure 50 shows two 90° fibers in which rzcs have caused matrix cracks to form. In turn, these matrix cracks have nucleated slip within the matrix. Of particular interest in this picture is that the rzcs are seen to not only cause cracking within the matrix, but appear to be causing a more extensive debond of the 90° fibers. In contrast to the more common debonding which occurs between the reaction zone and the outer carbon silicon layers of the fiber, the rzcs are causing debonding on an additional layer, between the carbon/silicon layers coating and the bulk silicon carbide (see Fig. 6). Evidence of extensive amounts of rzcs on the fracture edge (Fig. 51) further emphasize that they play an important role on the initiation of deformation during fatigue loading.
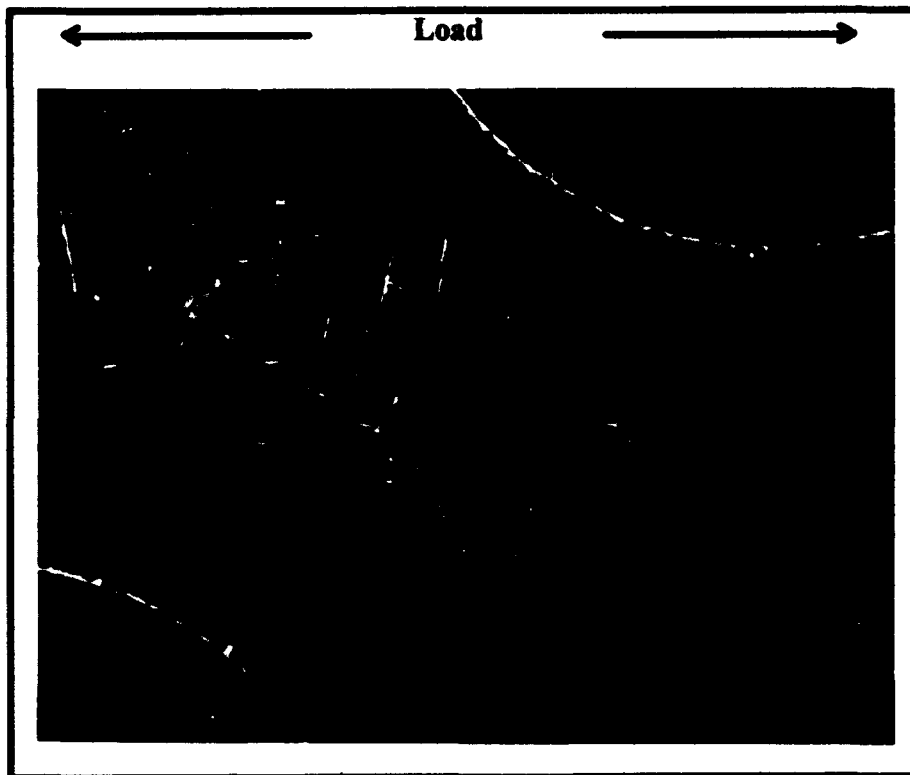
Figure 50. 600 TT RT: 90° RZCs Nucleate Matrix Damage and Plasticity (750x)

80

However, matrix plasticity often existed in the absence of matrix cracking, nucleating from both 90° and 0° fibers. Figure 52 shows a portion of a longitudinal section at the fracture surface, in which several types of deformation are evident. The 90° fibers are slightly debonded, and contain rzcs (the rzcs are more evident at higher magnification). The rzcs have nucleated slip bands, but as mentioned above, matrix cracking has not yet occurred. Both 0° fibers have debonded, and the matrix between these fibers and the 90° fiber between the two appears to have necked. Since, in general, debonding occurred on the top and bottom of the 90° fibers, the debonding on the *side* of the 90° fibers further away from the fracture surface, coupled with the debonding of the adjacent 0° fiber, is also evidence that the matrix necked under the tensile load.
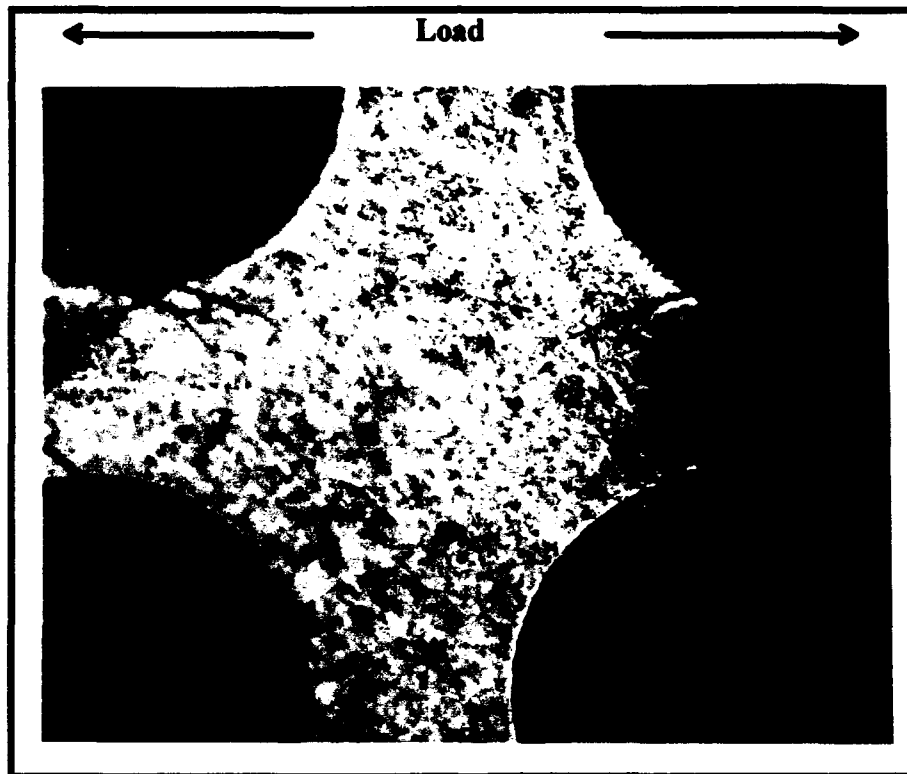
Figure 51. 600 TT RT: 90° RZCs On Fracture Edge (400x)

81
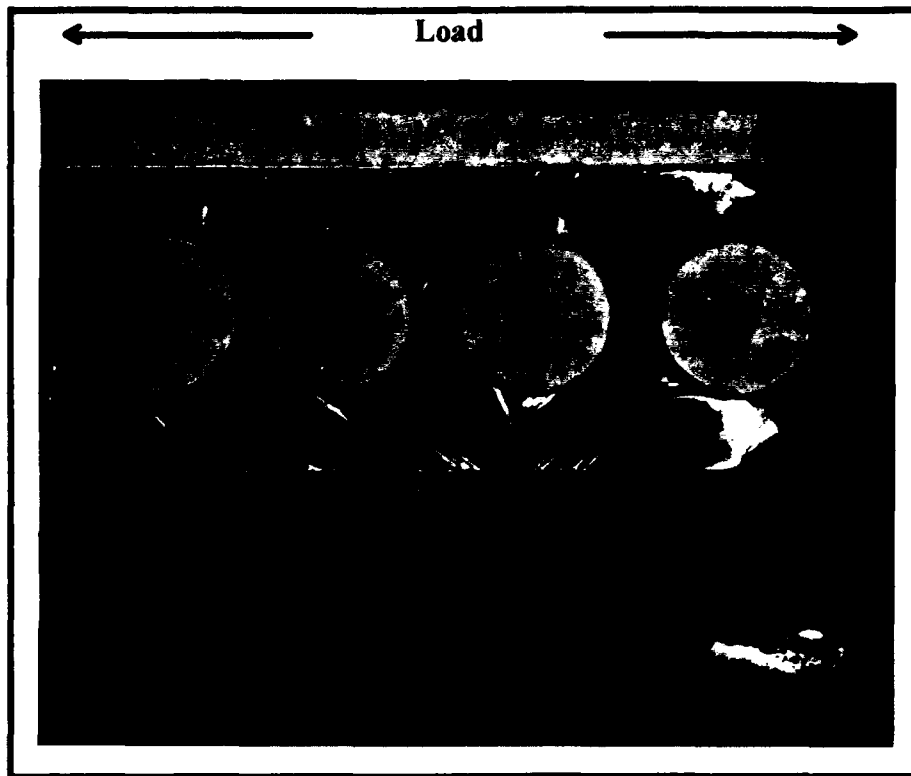
Figure 52. 600 TT RT: Matrix Plasticity and Necking Between Fibers (150 x)

Matrix plasticity was also evident on the unetched specimen edge. Figures 53 through 55 are a progression of photomicrographs showing slip bands which formed in the matrix near a 0° fiber. Since edge replicas were not taken on this portion of the specimen edge, the progression of damage is unknown. However, it appears that a combination of the rzc in the nearby 0° fiber and the gross plasticity within the matrix as a whole at the high strain level caused the slip band formation. From the photomicrographs, it is evident that the preferred slip planes are parallel to one another. Additionally, the 5000x photomicrograph displays the raised morphology of the slip bands.

Fractography for this specimen revealed the tensile-overload type of failure which characterizes a fiber-dominated fatigue failure. Although some cleavage type areas existed, the dominant surface morphology was the dimpled surface of ductile void coalescence. In these regions, matrix necking between the failed 0° fibers is clearly seen (Figs. 56 and 57).

82
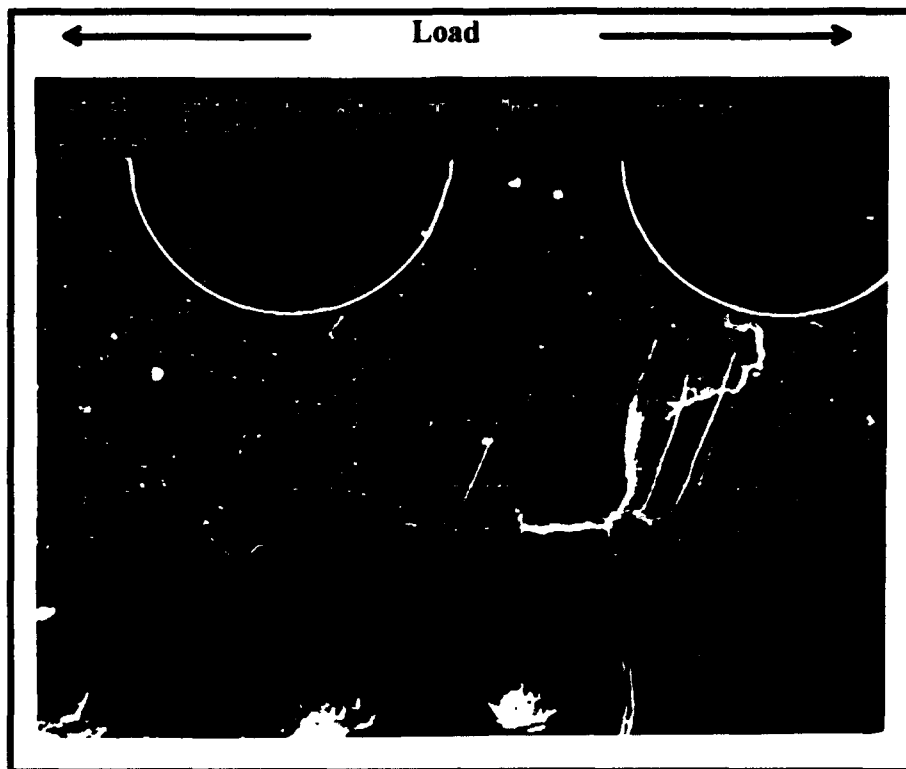
Figure 53. 600 TT RT: Slip Band Formation Near a Broken 0° Fiber (300x)
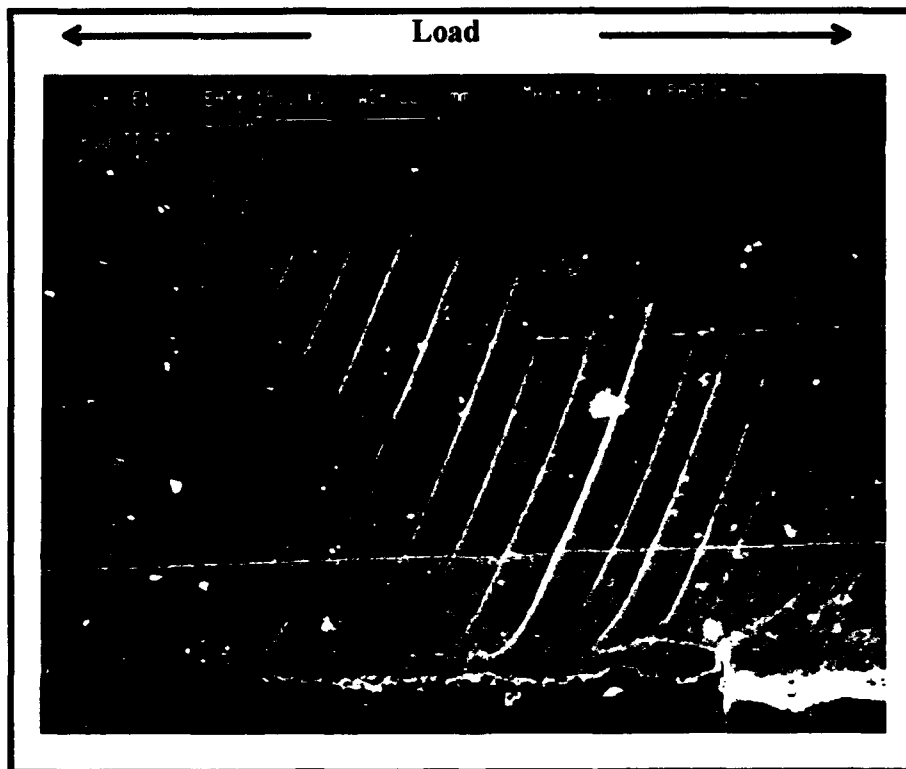
Figure 54. 600 TT RT: Close-up of Slip Bands (1000x)
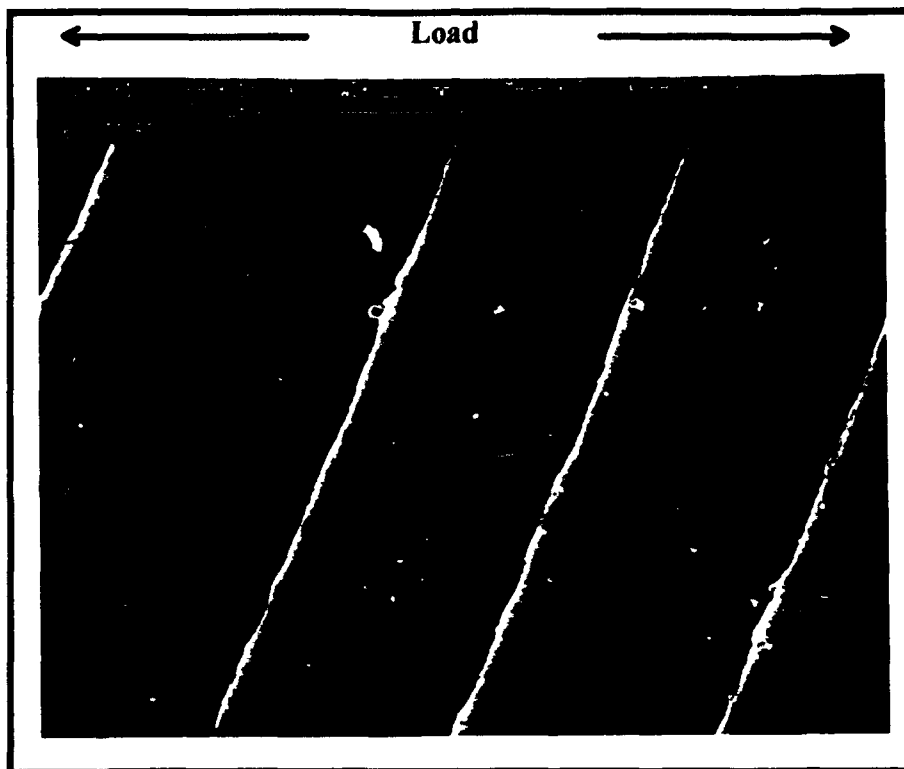
Figure 55. 600 TT RT: Close-up of Slip Bands (5000x)
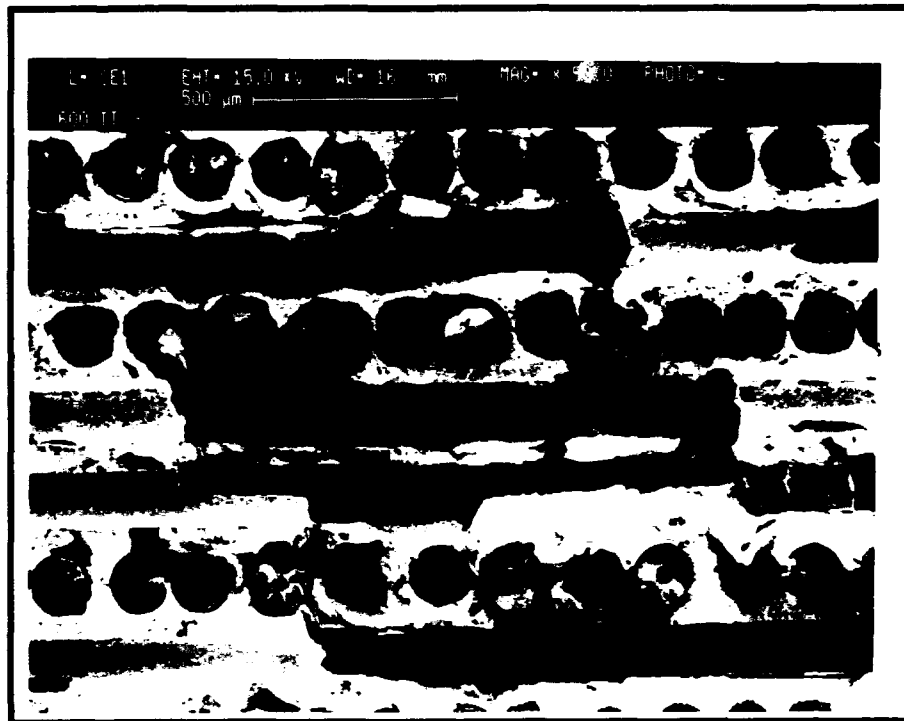
Figure 56. 600 TT RT: Fracture Surface (50x)

84

Figure 57. 600 TT RT: Ductile Void Coalescence and Necking (313x)

Thus, the replica, sectioned specimen, and failure surface evaluations support the conclusion that the Regime 1 failure was characterized by fiber failure and matrix plasticity.

Regime 2a Test: 450 MPa. Deformation Regime 2a was similar to that in Regime 1, with the exception that more matrix cracking, and less fiber breaking and matrix plasticity occurred.

Edge replica examination revealed that matrix plasticity began as early as the 105th cycle (26 percent of the fatigue life), and emanated from both 0° and 90° fibers. Several 0° fiber failures were evident in the cycle 10 and 105 edge replicas (0.02 and 26 percent of fatigue life, respectively). Matrix cracks had just begun at 31,664 cycles (78 percent of fatigue life), and existing 0° fiber breaks had opened up. At specimen failure, matrix cracks and the associated plasticity bridged up to five plys of the eight ply laminate.

Examination of the fracture surface reveals that a mixed mode failure occurred. The increased amount of flat, or cleavage, areas make it evident that much more matrix cracking occurred in this test than in the Regime 1 test. In addition, the multi-leveled fracture surface in conjunction with the many dimpled areas also reveal that some pre-failure fiber damage occurred during the specimen life (Figs. 58 and 59).

Figure 58. 450 TT RT: Fracture Surface (45x)
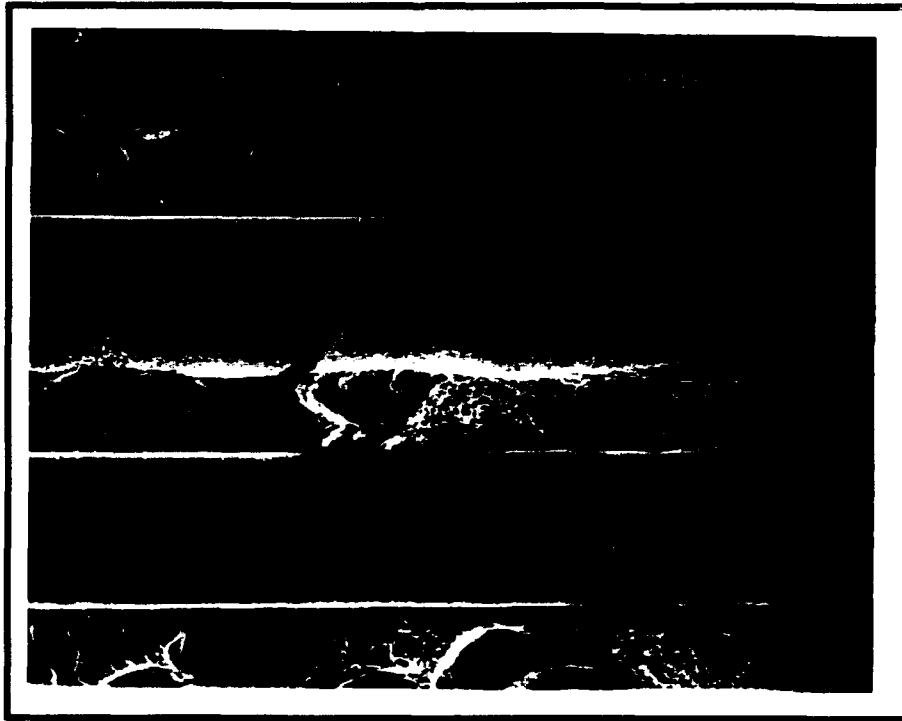
Figure 59. 450 TT RT: Mixed Mode Failure (150x)

Regime 2 Tests: 300 and 250 MPa. These tests were clearly in Regime 2 of the SN curve. With 646,253 and 1.9 million cycle fatigue lives respectively, the specimen failures were characterized by extensive matrix cracking, matrix plasticity, and very few fiber failures.

Edge replica evaluation for the 300 MPa test revealed that matrix cracking was just beginning at 10,000 cycles (1.5 percent of the fatigue life). By 106,000 cycles (16 percent of fatigue life), approximately fifty percent of the matrix cracks had grown to approximately 1/3 of a fiber diameter long, not reaching the adjacent ply. The remaining fifty percent of the matrix cracks bridged up to three plys. These cracks grew much longer by 200,000 cycles; some matrix cracks spanned all 8 plys of the specimen. Additionally, matrix plasticity around the 90° fibers was evident. The remainder of the specimen life was dominated primarily by existing matrix crack growth and plasticity.

Examination of the sectioned 300 MPa specimen also revealed extensive matrix cracking, matrix plasticity, and very limited fiber damage. As seen on the edge replicas, many of the matrix cracks spanned the entire thickness of the specimen, as seen in Fig. 60. Of particular interest in this photomicrograph is that the matrix crack grew *around* the 0° fibers, leaving them to carry the load which the damaged matrix could no longer support. Since many of these cracks spanned the entire specimen thickness as early as 30 percent of the fatigue life, it is clear that from that point forward, the fibers carried a significant portion of the specimen load. Also of note in this photomicrograph is that the crack grew *through* 90° fiber on the right hand side; not around it.

Edge replica evaluation for the 250 MPa test revealed that matrix cracking began at approximately 75,000 cycles (3.75 percent of fatigue life). At 590,000 cycles (29.5 percent of fatigue life) most of the cracks spanned the entire specimen thickness. At 832,000 cycles (41.6 percent of fatigue life) more matrix cracks existed. At 1.5 million cycles (75 percent of fatigue life) matrix plasticity and fiber failure had occurred.
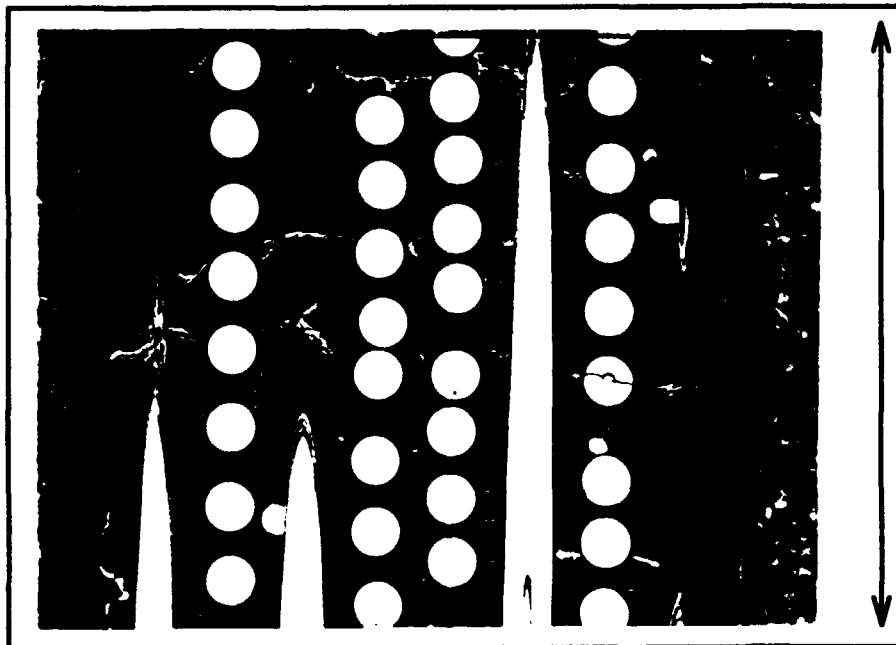
Figure 60. 300 TT RT: Matrix Crack Over Entire Specimen Thickness (50x)

Fractography also indicated matrix dominated failures for both tests. The fractures occurred along single 90° plies, with very little fiber pullout, no matrix necking, and no ductile void coalescence (Fig. 61). High magnification of the matrix regions revealed a combination of fatigue striations and highly crystallographic and faceted surfaces (Figs. 62 and 63). This fracture morphology is very similar to that found in the 175 MPa tension-compression (Regime 2) specimen.
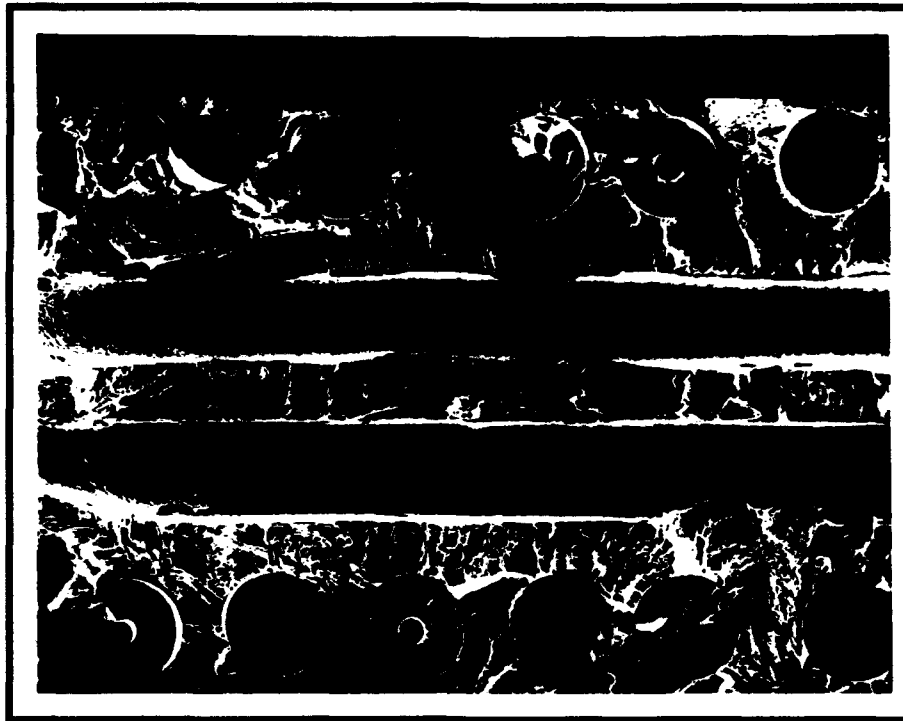
Figure 61. 300 TT RT: Planar, Brittle Cleavage Type Fracture Surface (100x)
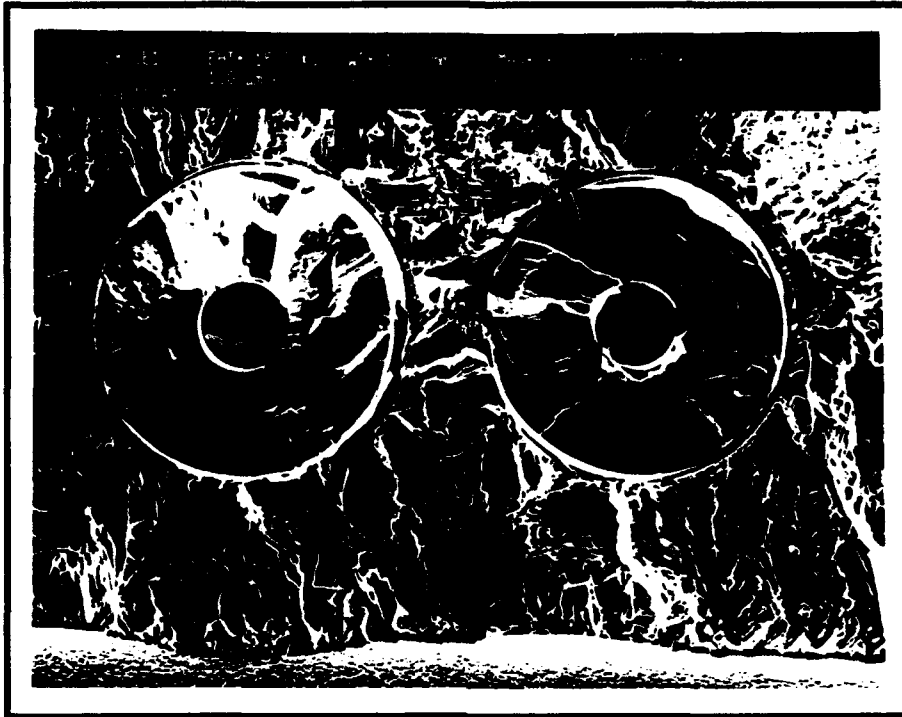
Figure 62. 300 TT RT: Crystallographic and Faceted Matrix Surface (300x)
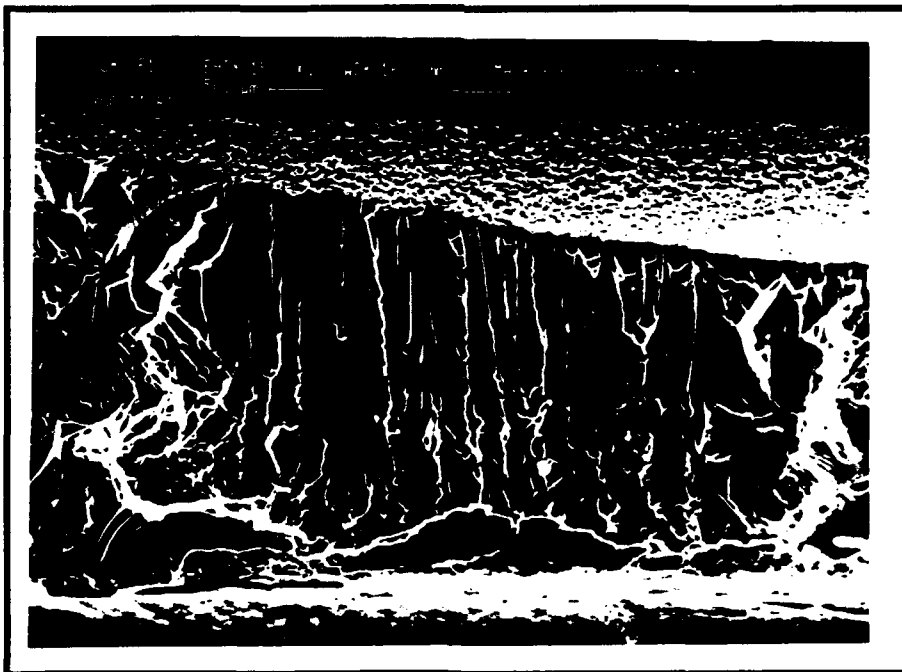
Figure 63. 300 TT RT: Fatigue Striations in Matrix Between Two 90° Fibers (650x)

Regime 3 Test: 200 MPa. As mentioned in the previous section, this specimen did not fail in over ten million cycles, thus it is clearly a Regime 3 test. Similar to the Regime 3 tests reported by Majumdar and Newaz (30), very few matrix cracks initiated, and those, were quickly arrested.

Rzcs and a small amount of matrix plasticity were evident in both the edge replica and specimen examinations. Figure 64 shows a rzc which has formed in the fiber-matrix interface of a 90° fiber. The rzc has nucleated a matrix crack and matrix plasticity in the form of slip bands. The matrix crack was quickly arrested, and hence no failure occurred.

TC HT Macro-mechanic Evaluation

With the exception of the first 300 MPa test, each of the above specimens failed in the center of the gauge length, or heat zone (Fig. 65). As mentioned previously, the
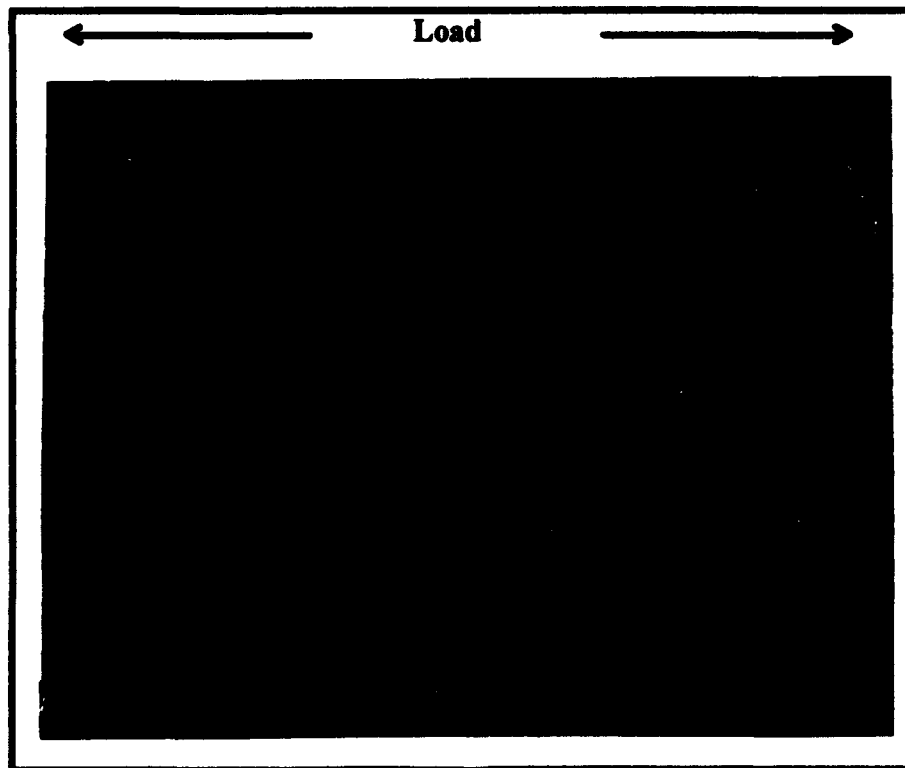
Figure 64. 200 TT RT: RZC Induced Matrix Plasticity (752x)
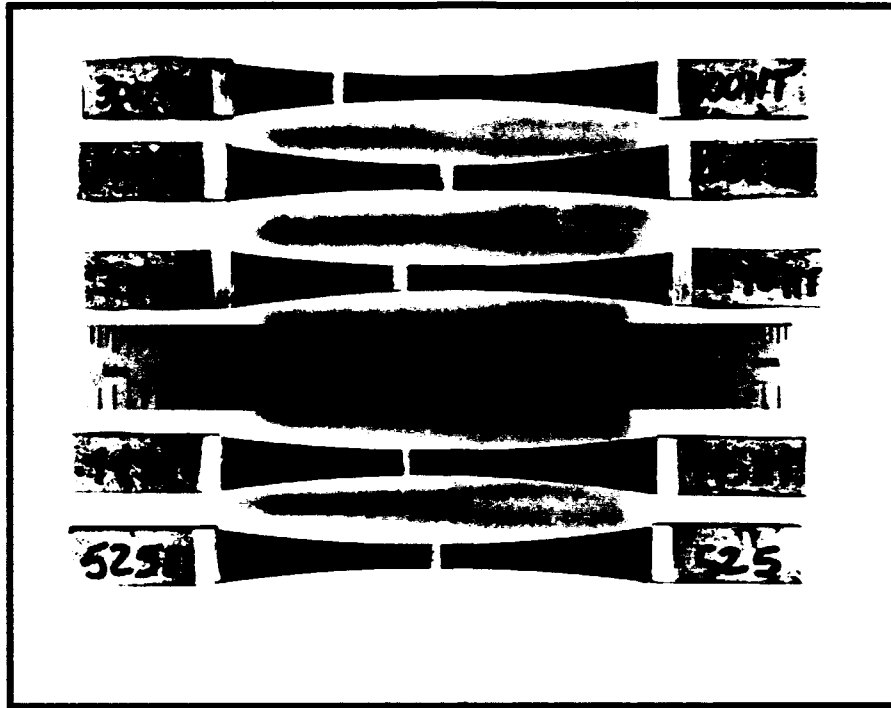
Figure 65. TC HT: Failed Dogbone Specimens

matrix cracking induced by the temperature gradient was alleviated by placing the heat lamps as close to the hydraulic grips as possible, heating the entire specimen. This method was successfully employed for the remaining four tests.

Stress, strain, fatigue life, modulus degradation, and dominant failure modes for the tension-compression high temperature tests with the dogbone specimens and buckling guides are summarized in Table 5, and the fatigue life data is plotted on a maximum applied stress basis in Fig. 66. Of significant interest in both of these is that the fatigue lives of the two lowest stress tests are significantly larger than the corresponding room temperature tests (although 370 MPa was not tested at room temperature, an approximate fatigue life can be estimated from the SN curve in Fig. 22). Although the comparisons of the room temperature and high temperature tests will not be discussed in this section, it may be useful to the reader to keep this in mind when reviewing the information presented here.

Table 5. TC HT: Macro-mechanic Results Summary

Max Stress (MPa)	Stress Range (MPa)	Max Strain (%)	Strain Range (%)	Regime of Failure	Cycles to Failure	Percent of Initial Strain at Failure $(\varepsilon_{fail}/\varepsilon_i)*100$	Percent of Initial Modulus at Failure $(E_f/E)*100$	Dominant Failure Modes
300	600	0.388	0.439	2	170,900	149.17	89.0	mc, mp
300	600			2	154,704	153.00	95.1	(diffused)
370	740	0.360	0.571	2	18,606	110.10	95.4	mc, mp (diffused)
445	900	0.600	0.697	2a	8,501	153.06	73.6	ff, mc (some), mp
525	1050	0.474	0.811	1	2,079	103.03	92.0	ff, mp
* mc = matrix cracking, mp = matrix plasticity, ff = fiber failure, db = debond								

The initial cycle for each of the high temperature tests revealed a knee in the stress-strain curve at average stress of 84 MPa, with a reduction in stiffness averaging 15.02 percent (Table 6). The knee occurred at a significantly lower stress level than the 180 MPa for the room temperature tests. This is expected, and can be attributed to the relaxation of the compressive residual stresses around the fibers due to the higher temperature implying fiber/matrix debonding at a lower stress level. Additionally, three of the five specimens exhibited a second knee at 350 MPa, resulting in a stiffness decrease averaging 23.26 percent. This knee also occurred at a significantly lower than the 542 MPa for the room temperature tests. Thus, it is clear that the elevated temperature hastens the onset of debonding and plasticity of the matrix.

Table 6. TC HT: Initial, Secondary, and Third Moduli During First Cycle

Maximum Stress*	Initial Modulus* (E_i) /Stress Value at Transition	Secondary Modulus, (Reduction from E_i)	Third Modulus /Stress Value at Transition, (Reduction from E_i)
300 Test 1	125.4/70	108.91 (13.14%)	N/A
300 Test 2	119.5/110	110.2 (7.78%)	N/A
370	136.4/90	104.5 (23.38%)	103.4/350 (24.19%)
445	131 7/60	113.1 (14.12%)	102.2/350 (22.39%)
525	133.2/90	111.0 (16.66%)	102.3/350 (23.9%)
Average	129.24/84	109.54 (15.02%)	102.6 (23.26%)
* All stresses are MPa, all moduli are GPa			
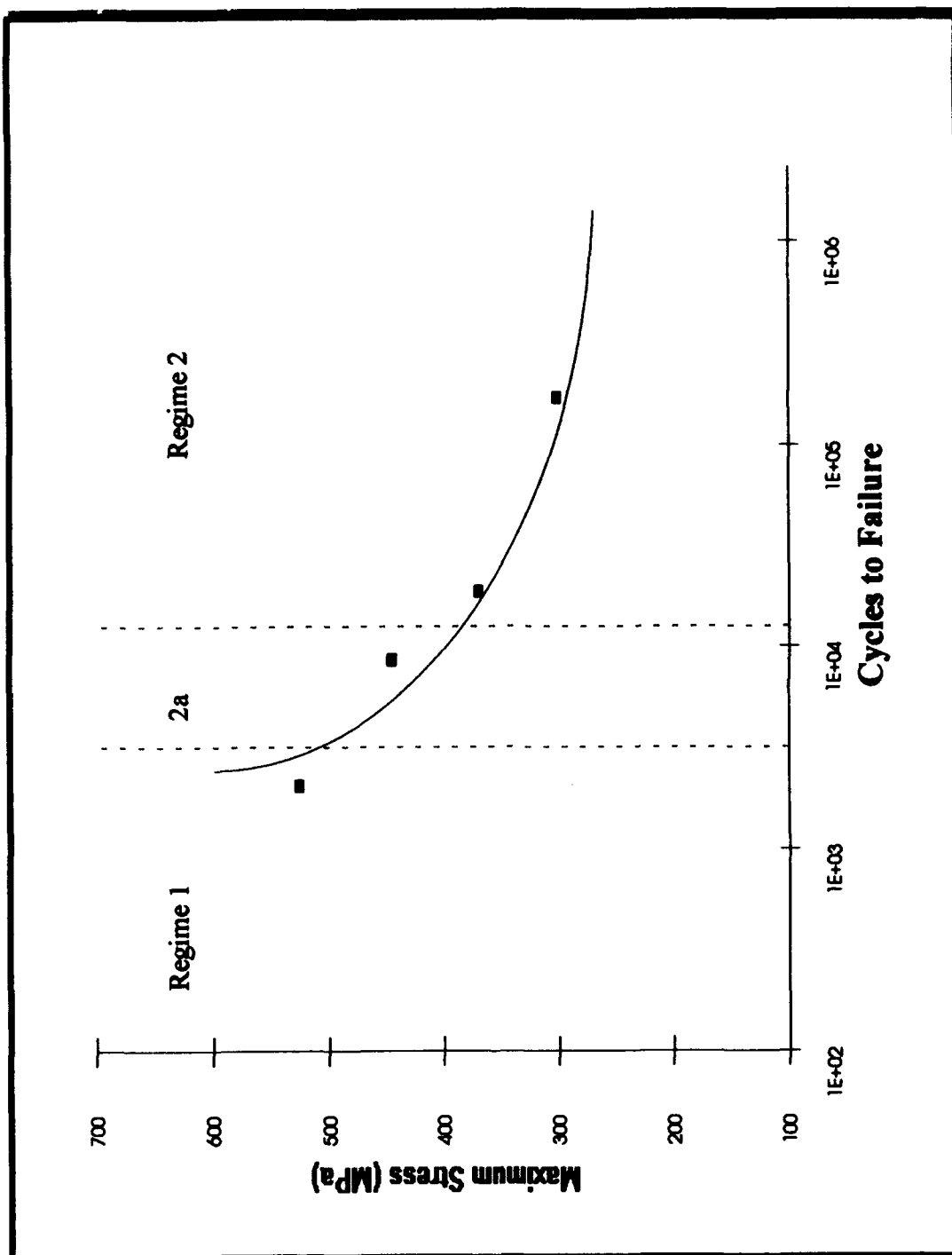
Figure 66. TC HT: SN Curve

94

The stiffness reduction and strain increase for each of the tests throughout the respective fatigue lives and normalized fatigue lives are found in Figs. 67 through 70. Several observations can be made from these figures. First, the two highest stress level tests, 525 and 445 MPa, behaved as expected: as the stress level was reduced, the amount of stiffness degradation increased due to the decreased prevalence of fiber failure and the increased prevalence of matrix cracking. This was seen both in the TC RT and TT RT test cases. However, the remaining two stress level tests did not follow such a pattern. The 370 and 300 MPa tests had much smaller stiffness reductions to only 95.4, 89.0 and 95.1 percent of the initial moduli, respectively. Additionally, the stiffness for the 300 MPa tests increased to 1.1 times the initial stiffness. This increase of stiffness resulting from extended exposure to the elevated temperatures at low stress levels has been reported by Sanders, and is possibly due to hydrogen diffusion within the matrix (44:95). It is clear that the mechanisms for specimen failure must differ between the two higher and lower stress levels.

Further illustrating this point is that the increase in strain behaved in a similar manner. The two highest stress levels behaved as expected. For instance, the 525 MPa specimen strain increased only slightly, as can be expected from a Regime 1 test dominated by fiber failure. The 445 MPa specimen strain increased more, indicating a combination of fiber and matrix damage. However, the two lowest stress levels, which in TC RT and TT RT tests had larger strain increases, showed only nominal increases before failure at high temperature

Clearly, the micro-mechanic mechanisms causing this drastic difference in behavior must be examined, especially in light of the extended fatigue lives of the specimens at the two lower stress levels.
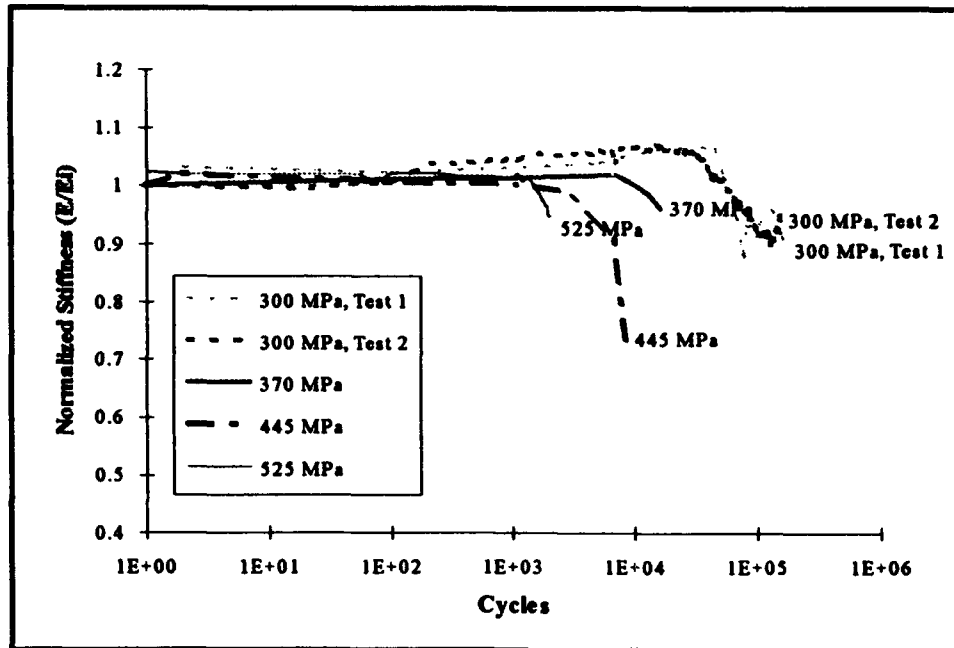
Figure 67. TC HT: Normalized Stiffness vs. Fatigue Cycles
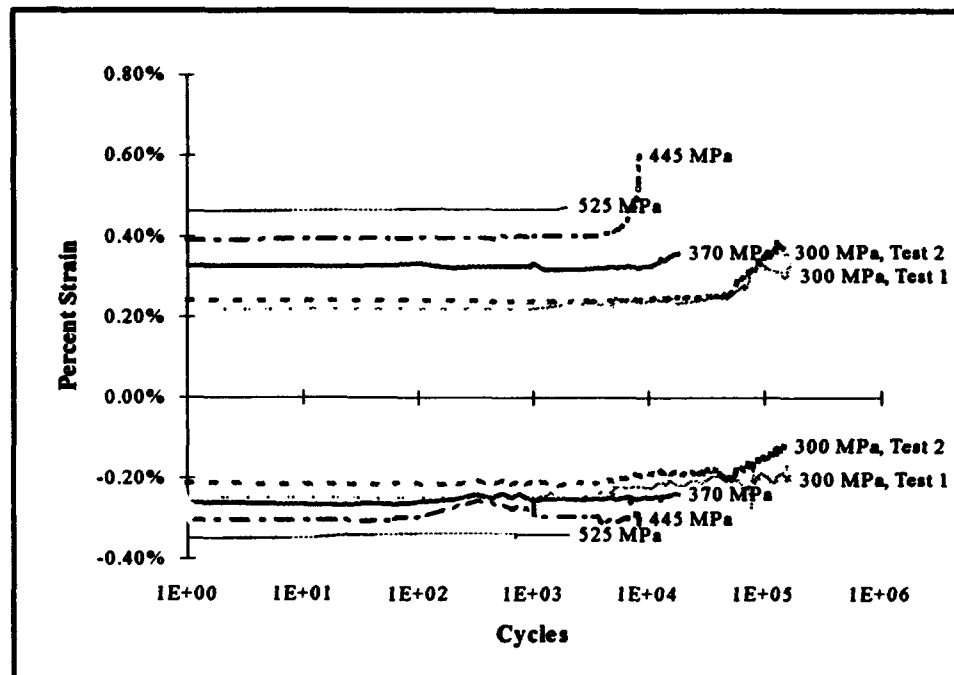
Figure 68. TC HT: Percent Strain vs. Fatigue Cycles

96
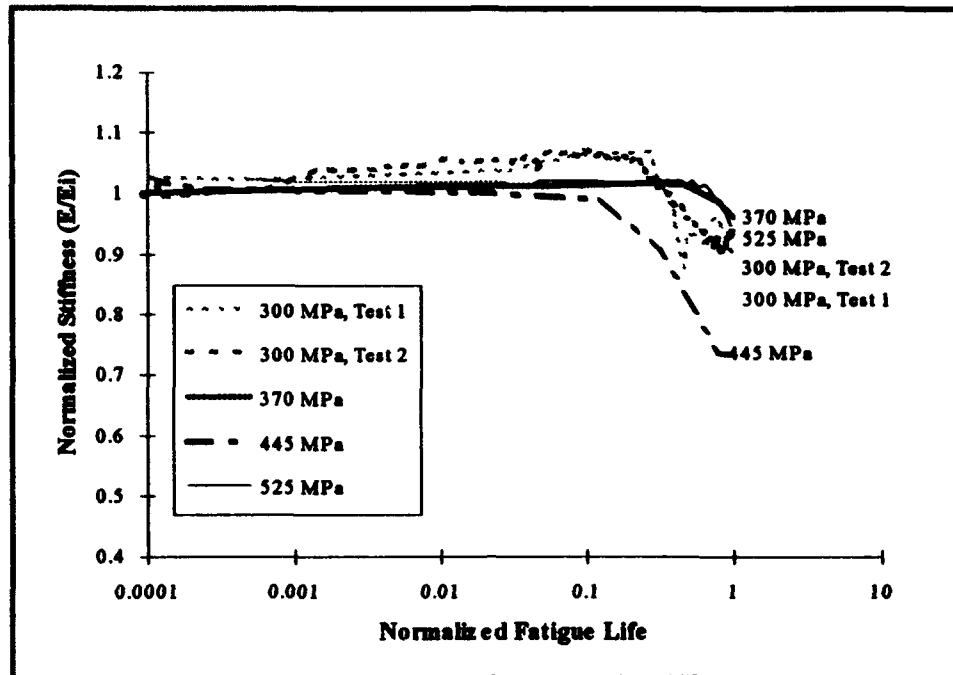
Figure 69. TC HT: Normalized Stiffness vs. Normalized Fatigue Life
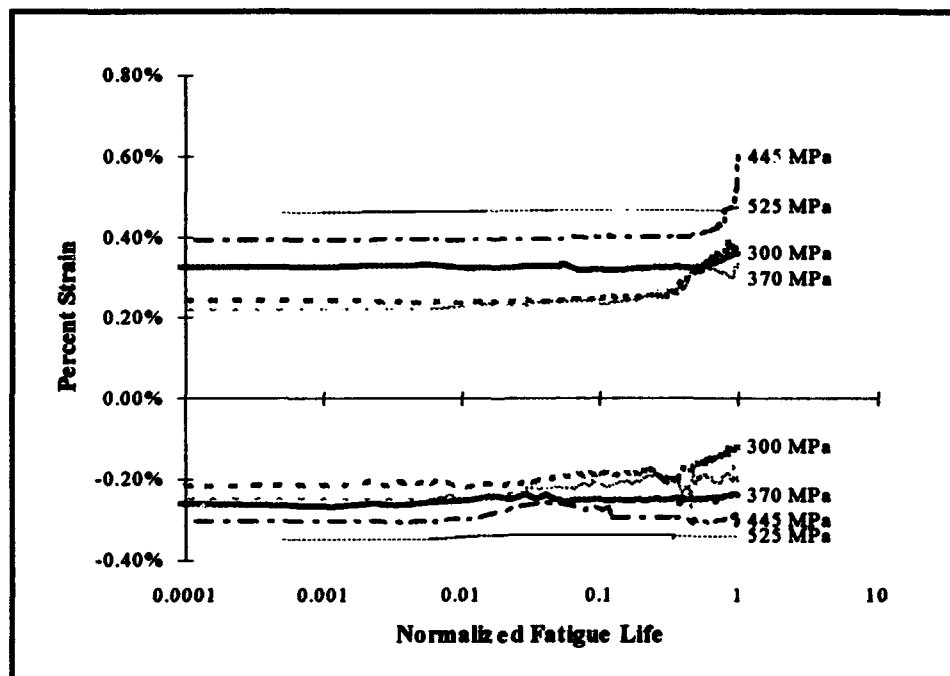
Figure 70. TC HT: Percent Strain vs. Normalized Fatigue Life

Regime 1 Test: 525 MPa. This highest stress level test was clearly a Regime 1 failure. With a short fatigue life of only 2,079 cycles, the micromechanic deformation was dominated by fiber failure and matrix plasticity.

The edge replica evaluation revealed debonding of the 90° fibers after the initial cycle. At 699 cycles, or 33 percent of the fatigue life, extensive 0° fiber breaks had occurred. At this time, no matrix cracks or matrix plasticity was evident.

Evaluation of the sectioned specimen confirmed that 0° fiber failure had occurred. Additionally, extensive 90° fiber-matrix debonding was discovered. Of particular interest is that this drastic debonding occurred mainly in the areas of the interface which were perpendicular to the applied load, indicating that the compressive portion of the fatigue load was the cause. This can be partially explained by the relaxation of the tensile residual stresses in the matrix surrounding the fibers. These residual stresses are present due to the coefficient of thermal expansion mismatch between the fiber and matrix and are partially relieved by heating the specimen to 427°C, as will be discussed in Chapter 5. For this reason, the matrix in the area surrounding these 90° fibers experiences a higher compressive load at elevated temperature than at room temperature. Thus, the 90° fiber-matrix interface is more highly stressed, causing more extreme debonding, often times not only between the rzc and the silicon/carbon layers, but also between these layers and the bulk SiC. In addition to this debonding, several of these fibers contained radial cracks, also due to the compressive loading. Figure 71 illustrates this debonding and radial fiber cracking. Slip bands can also be seen emanating from the debond.

Although matrix cracking did not seem to be the dominant damage mechanism, some did exist. These cracks emanated from rzcs in the 90° fiber matrix interface, never spanned more than two plys, and were always accompanied by extreme amounts of plasticity. The majority of this plasticity was diffused (seen as *areas* of white on the

etched specimens) indicating a very high density of dislocations, rather than highly defined as seen (as distinct slip bands) at room temperature. Additionally, approaching matrix cracks often caused debonding of the 0° fibers. A typical region containing matrix cracks, 0° debonding, and plasticity can be seen in Fig. 72. Transverse sections revealed that some debonding between the outer two silicon/carbon layers of the 0° fibers had occurred. No longitudinal cracks formed and no plasticity around the 0° fibers was evident.

Examination of the fracture surface revealed that fiber fracture occurred before matrix failure, or dominant matrix cracking. This can be seen in Fig. 73, where the matrix is covered with ductile void coalescence. Thus, it is concluded that this highest stress test failed predominantly due to fiber failure, although matrix plasticity and matrix cracking were definitely contributing factors.
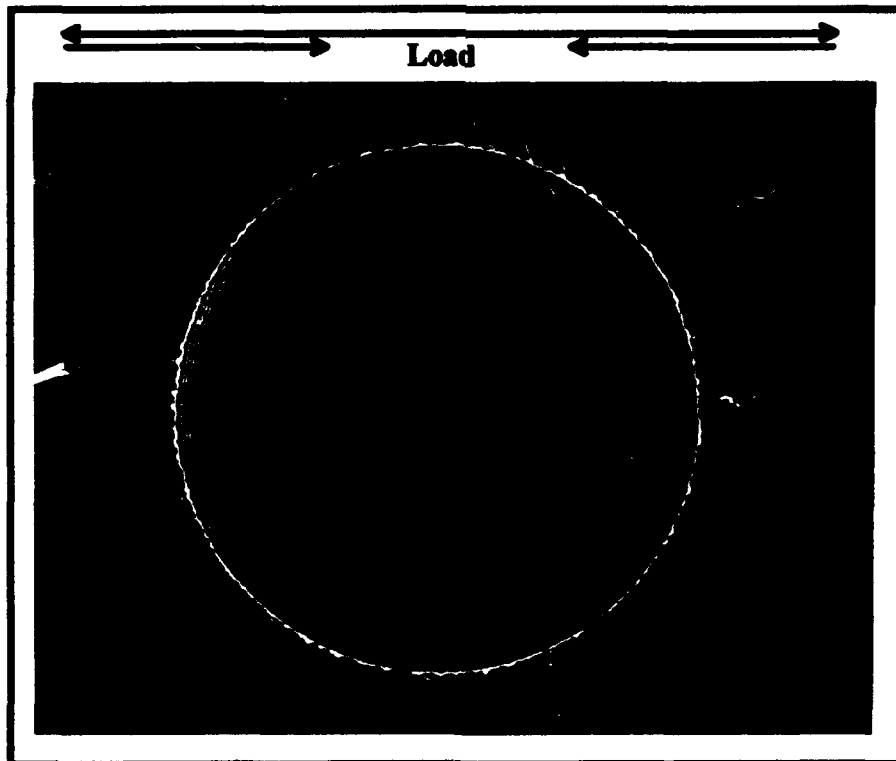
Figure 71. 525 TC HT: Extensive Debond and Radial Fiber Crack (500x)
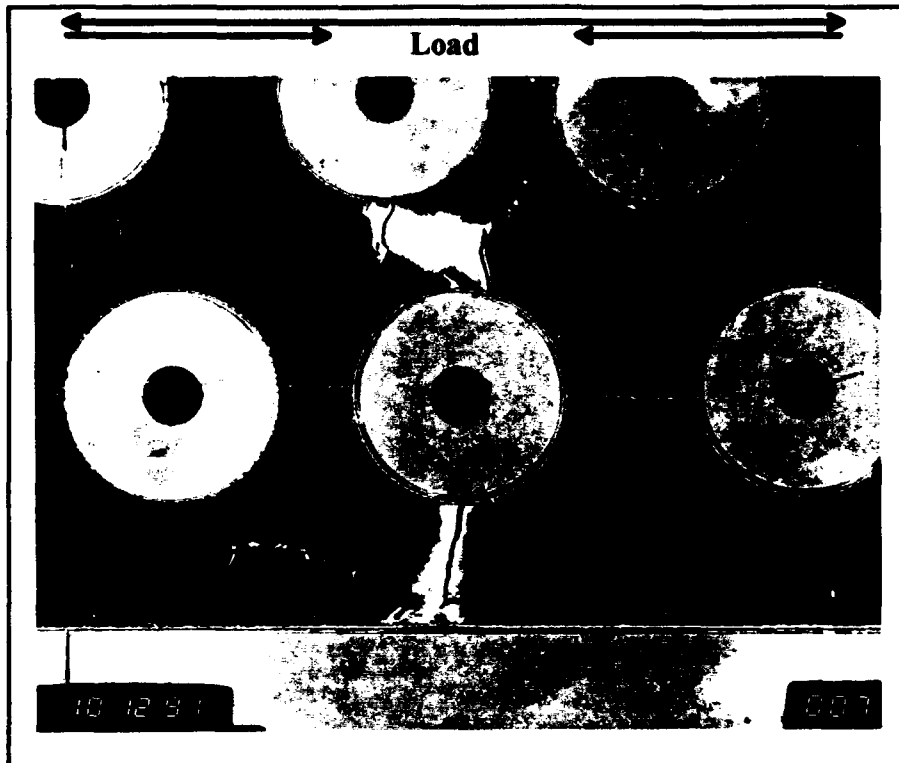
Figure 72. 525 TC HT: Matrix Cracking and Plasticity, Debonded 0° Fiber (200x)
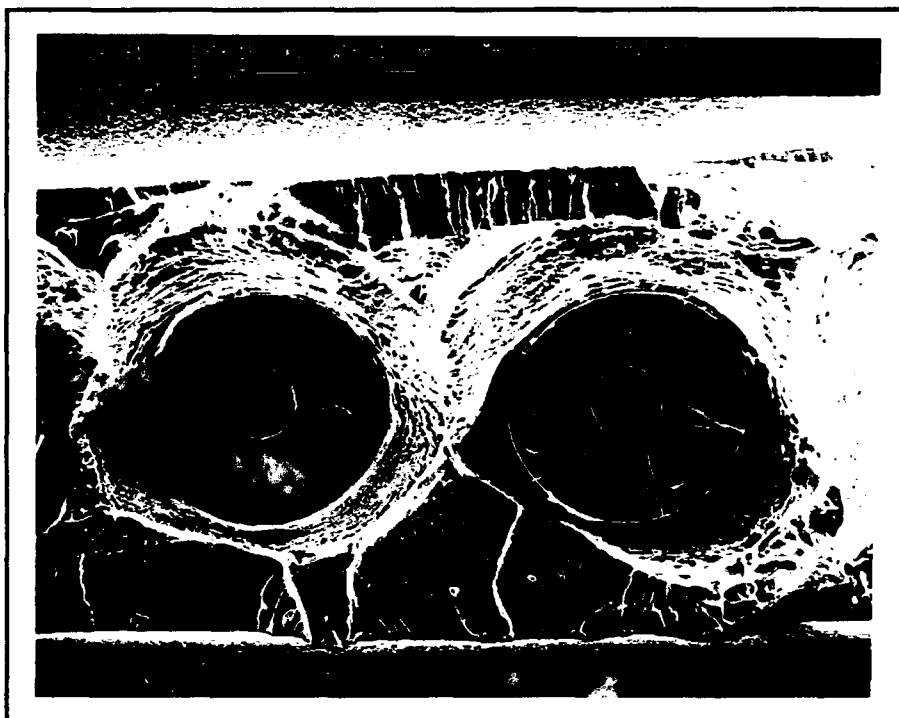
Figure 73. 525 TC HT: Matrix Necking and Ductile Void Coalescence (250x)

Regime 2a Test: 445 MPa. Deformation in the Regime 2a test displayed similar types of damage and plasticity as the Regime 1 test. However, considerably more matrix cracking was evident.

Edge replicas revealed that 2,360 cycles, or 31 percent of the fatigue life, many 0° fibers had broken. At 6,777 cycles, or 79.7 percent of the fatigue life, matrix cracks had grown from 90° fibers and spanned up to five plys. It is significant to note that although these cracks existed, their *occurrence* was not extensive. In other words, the cracks were long, but they were few and far between. Also, since they were not detected up to 2,360 cycles, but had grown up to five plys by 6,777 cycles, it is suggested that the matrix crack growth rate may be accelerated by the increased temperature.

Examination of sectioned specimens revealed a combination of fiber and matrix damage and plasticity. Again, the matrix cracks were long, but few and far between. Of particular interest is that matrix cracks were actually observed to initiate in the matrix *without* being nucleated at a rzc in a 90° fiber. This is significant since it was not seen in either the TC RT or TT RT tests, and indicates that the increase in temperature may reduce the criticality of the fiber-matrix rzc in matrix crack nucleation. Also of interest is that in some cases, an approaching crack, instead of growing around 0° or 90° fibers in its path, as seen in previous tests, actually grew *through* the fibers. As seen in the Regime 1 test, matrix plasticity was much more diffused than at room temperature. Figure 74 illustrates these deformation mechanisms.

Although the plasticity was predominantly very diffused, it was the most defined in the region between the 90° fibers, parallel to the load. The occurrence and extent of this plasticity was a function of the proximity of the adjacent 90° fiber; the closer the fibers, the more the plasticity. This indicates that the stress field in the matrix between two fibers is made more severe when the fibers are closely spaced. This effect is enhanced by the previously mentioned relaxation of the tensile residual stresses in the matrix at this
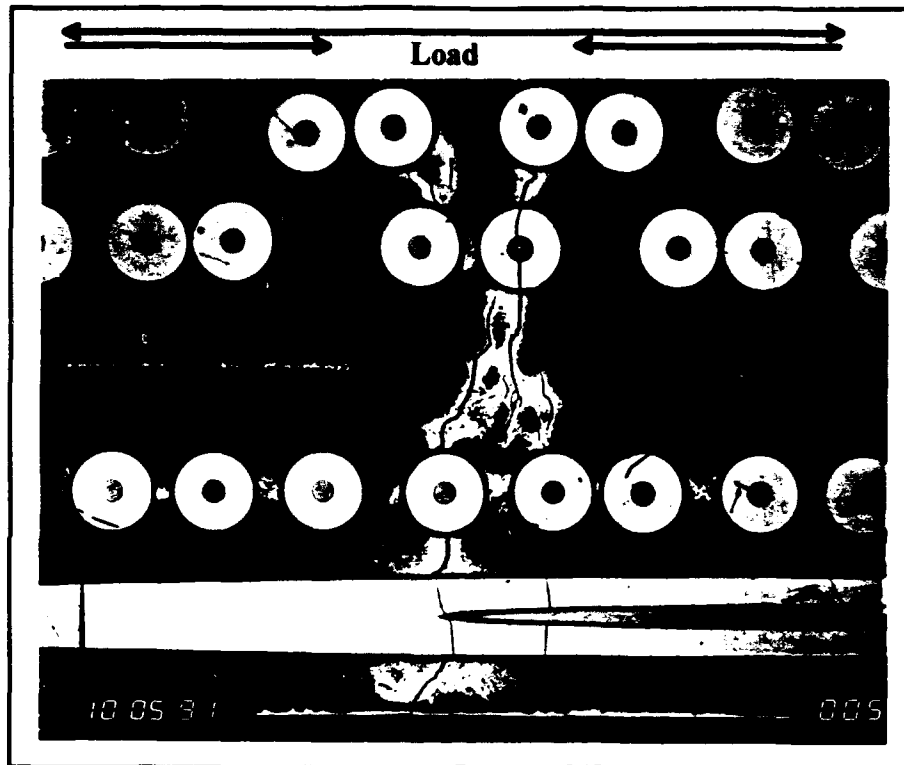
Figure 74. 445 TC HT: Diffused Plasticity, Matrix Cracking, Fiber Breaks (80x)

elevated temperature. Figure 75 shows one of the most defined areas of plasticity; although it is still very diffused, dislocations appear to be concentrated on preferred slip planes at equal angles from the load direction. Transverse sections revealed less 0° debonding than the Regime 1 test, and no longitudinal cracks existed.

The fracture surface indicated both fiber breaking and matrix cracking, since a combination of cleavage and ductile void coalescence areas existed. The cleavage type fracture surface was predominant, indicating that although the matrix cracks were few, final fracture occurred along the plane of one of these matrix cracks. Further supporting this is the fact that fatigue striations existed on the surface, appearing to emanate from the 90° fibers (Fig. 76).
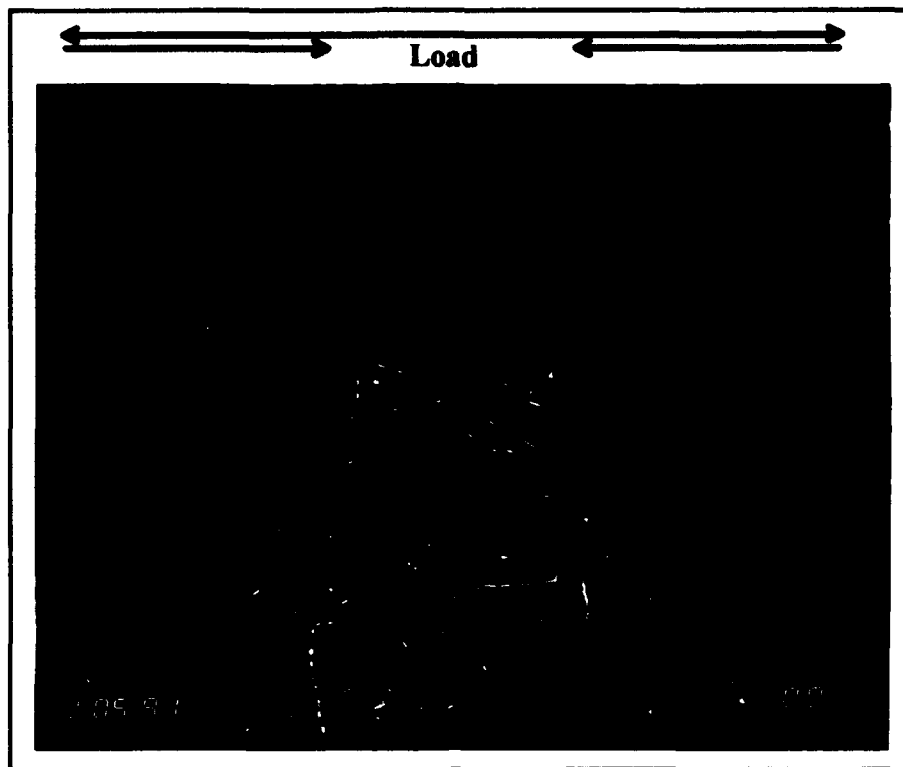
Figure 75. 445 TC HT: Diffused Slip Between Two 90° Fibers (400x)
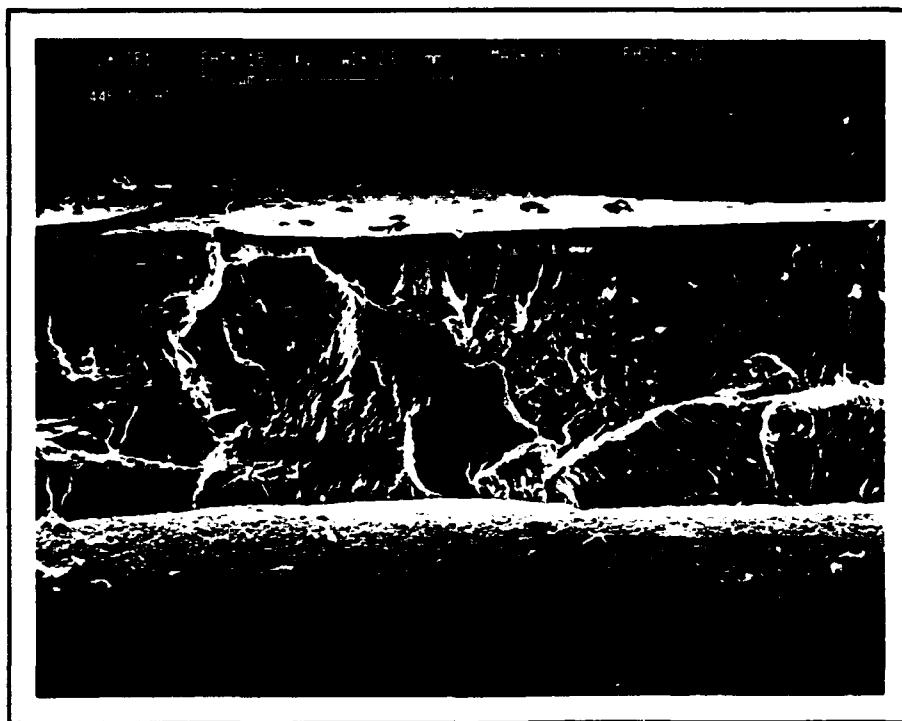
Figure 76. 445 TC HT: Striations on Fracture Surface Between 90° Fibers (500x)

Regime 2 Tests: 370 and 300 MPa. Both the 370 and 300 MPa tests were matrix dominated. Very little fiber failure occurred, and matrix plasticity was confined to areas of matrix cracking or closely spaced 90° fibers.

Edge replica evaluation revealed that the matrix cracks were long, but the amount of matrix cracking was not extensive. At 87.3 and 45.5 percent of the fatigue lives, respectively, matrix cracks spanned up to 7 plies.

Sectioned specimens also revealed that matrix cracking was not widespread, but those cracks which did exist were long, spanning the full specimen thickness in many locations. Matrix cracks appeared to grow perpendicular to the applied load; this differs from the room temperature tests in which matrix cracks most often grew at an initial 45° angle from the load. Figure 77 illustrates matrix cracks both bridging and penetrating fibers in their paths and the areas of plasticity near the cracks.
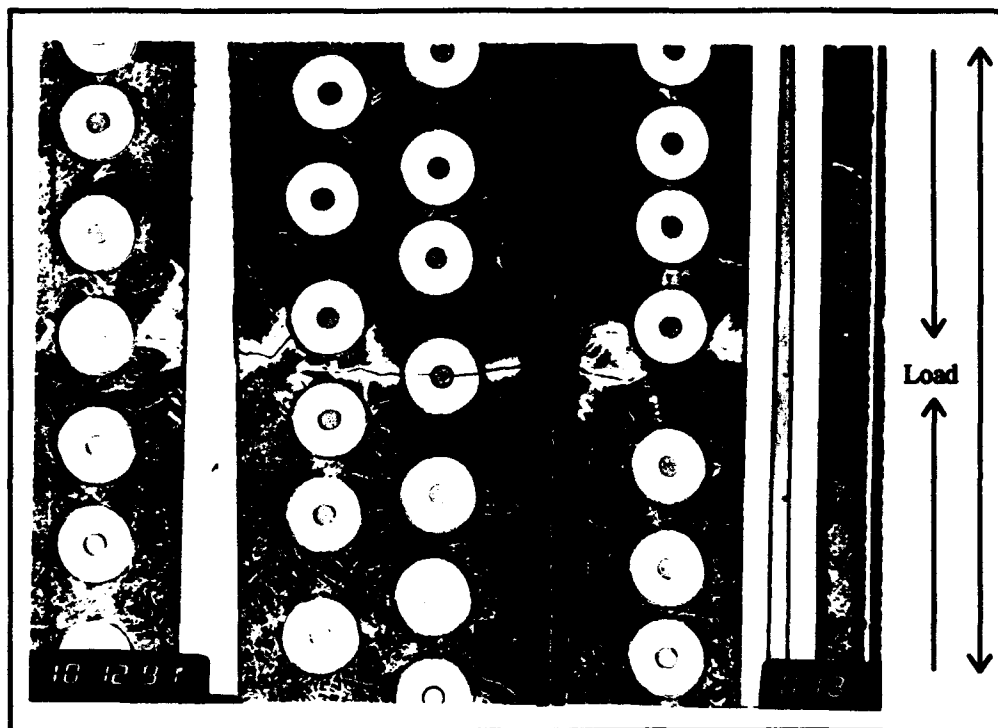
Figure 77. 370 TC HT: Crack Bridging, Radial Fiber Crack, Localized Plasticity (75x)

Examination of the fracture surfaces revealed extensive fatigue striations emanating from 90° fibers. These striations were less sharp than those observed at room temperature (Fig. 78), indicating the enhanced ductility of the matrix at high temperature. Figures 78 through 80 show the striations at increasingly higher magnification.

Thus, the dominant deformation mechanism for these Regime 2 elevated temperature tests is matrix cracking. The *occurrence* of this cracking is less than seen at room temperature, however, the *extent*, and the fatality of the existing cracks is more severe at higher temperature. Of utmost importance is that the *onset* of matrix cracking is considerably delayed by both the ductility of the matrix, and the diffusivity of the slip within the matrix at this higher temperature. These will be discussed in more detail in Chapter 5.
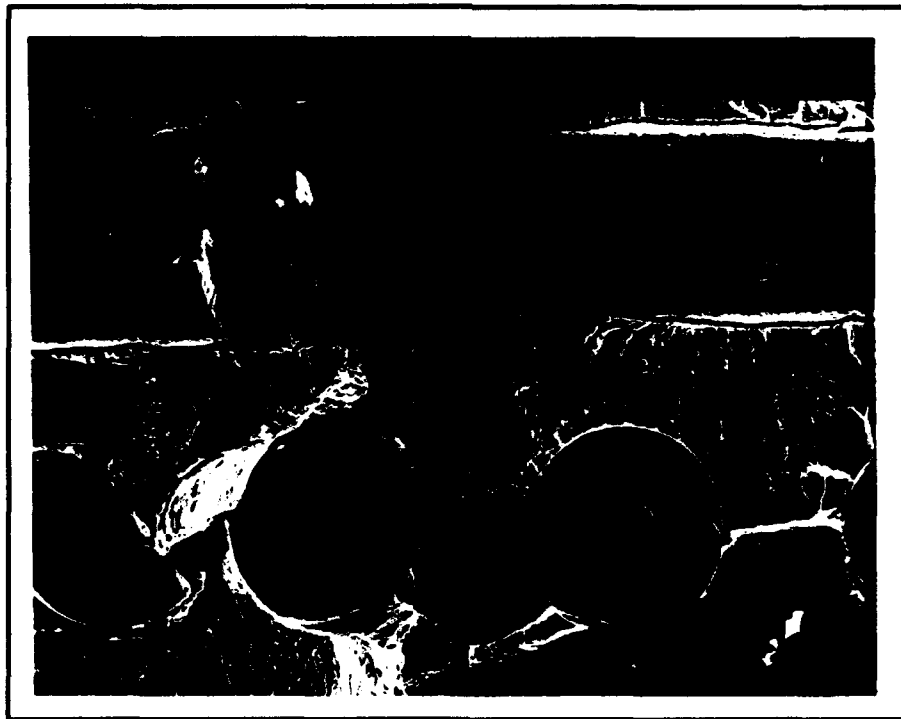
Figure 78. 300 TC HT: Fracture Surface (200x)
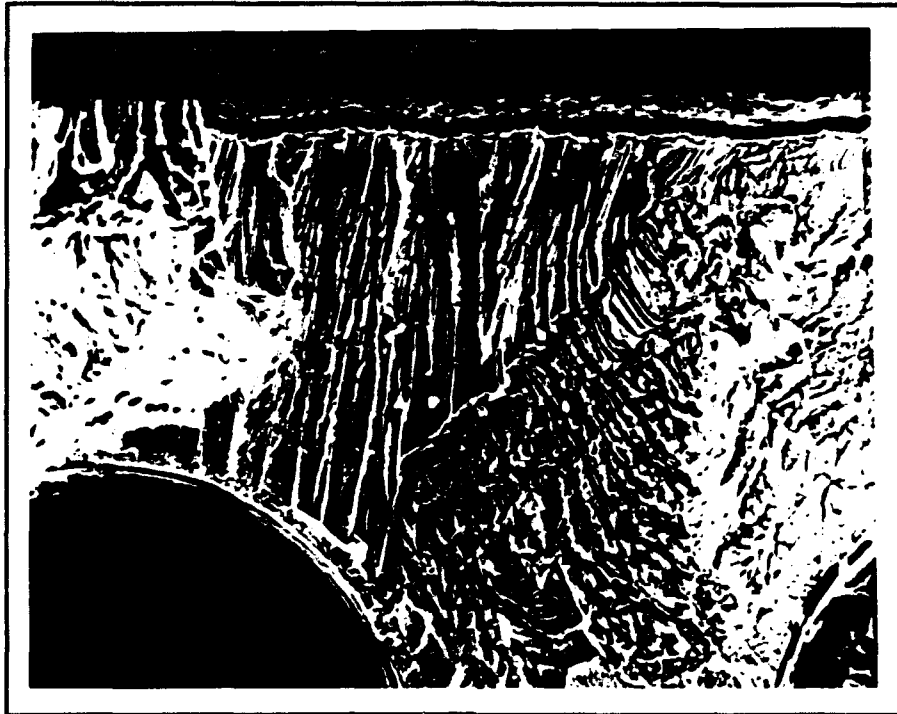
Figure 79. 300 TC HT: Fatigue Striations (662x)
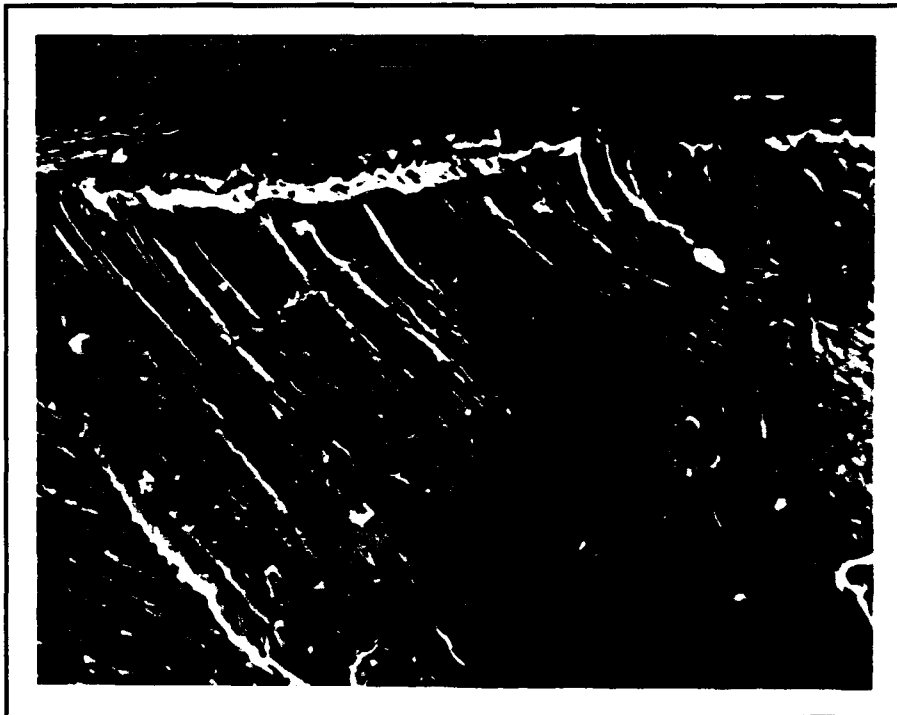
Figure 80. 300 TC HT: Close-up of Fatigue Striations (1,200x)

V. Analysis/Discussion

As previously mentioned, the apparent lack of techniques for performing tension-compression fatigue of MMCs has resulted in a significant gap in the full characterization of the damage mechanisms associated with this promising new class of engineering materials. This research, the first load-controlled fully-reversed fatigue testing to be performed on a MMC, seeks to extend the existing knowledge of fatigue damage mechanisms to include the tension-compression loading condition required for full characterization of the MMC damage mechanisms. This chapter will explain, in a detailed manner, the effects of tension-compression fatigue as compared with tension-tension fatigue at room temperature, and the effects of elevated isothermal temperature on the tension-compression fatigue loading condition. To accomplish this task, both the micromechanic and macromechanic evaluations for each of the three loading cases (*Chapter IV*) will be employed.

There is not, however, a clear cut manner in which to compare fatigue data collected under different R-ratios. The *maximum applied stress* criterion, found in much of the literature, works well for most tension-tension fatigue data. However, it completely ignores 50 percent (the compression portion) of the tension-compression fatigue cycle, and must therefore be used with discretion. The *applied stress range* criterion, in which the stress range is defined as the difference between the maximum stress and the minimum stress during the steady state strain portion of the fatigue life (Fig. 23), attempts to reconcile this shortcoming by accounting for the entire fatigue cycle, and is therefore applicable to the tension-compression fatigue loading case. Some authors, however, have suggested that fatigue life appears to be strain (not stress) dominated, and thus propose that a *strain range* criterion should be used to compare fatigue data performed under different loading conditions, or R-ratios (30:1).

107

Thus, comparisons will be made between TC RT and TT RT using the maximum stress, stress range, and strain range criteria. Advantages, shortcomings, and the applicability of each criterion will be discussed. Since the maximum stress, stress range, and strain range criteria yield similar comparisons between the TC RT and TC HT cases, this will be discussed in one section.

Additionally, because MMCs are multicomponent systems in which the dominant component (fiber or matrix) of failure changes with the loading condition, and because elevated temperatures change the initial stress state of the components in the high temperature tests, a *constituent stress* criterion which examines the micro stresses in both the fiber and the matrix individually, provides valuable insight into the deformation mechanisms active within each loading case, and may provide a common factor with which data obtained in different loading conditions can be compared. Since this information cannot be determined experimentally, an analytical technique must be employed. METCAN, the Metal Matrix Composite Analyzer, which was developed by Hopkins and Murthy (18) at NASA's Lewis Research Center, is used to model the constituent microstresses in the three loading cases: TC RT, TT RT, and TC HT.

TC RT vs. TT RT Comparison

Maximum Stress. Figure 81 compares the measured data from two cases: TC and TT at room temperature. It clearly shows that on a maximum applied stress basis, the TT fatigue lives were much longer than the TC fatigue lives. Thus, it is apparent that although the TC and TT specimens with equivalent maximum stresses underwent the same tensile load, the compressive load experienced by the TC specimens contributed to specimen failure. It definitely had a detrimental effect, since superimposition of compression reduced the fatigue life at a given maximum tensile stress.
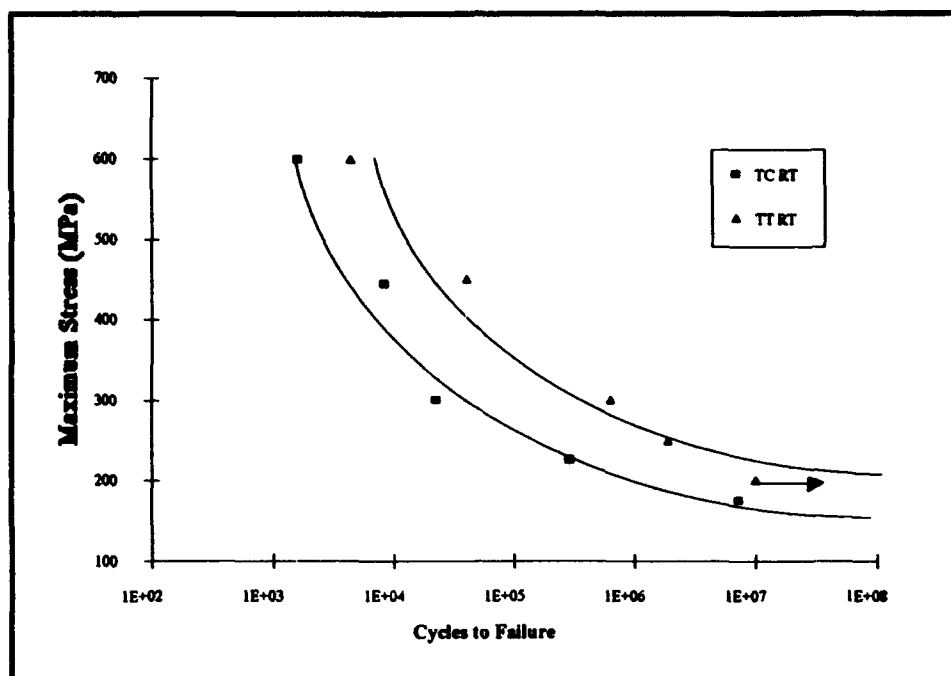
Figure 81. Maximum Stress SN Curve: TC RT vs. TT RT

The micro-mechanic evaluations revealed several different damage mechanisms which distinguished the TC case from the TT case. The fiber-matrix debonding was more extensive in TC than in TT. For example, almost every 0° fiber in the 600 MPa TC transversely sectioned specimen was severely debonded. The equivalent TT sectioned specimen revealed some 0° debonding, but not nearly as extensive, or as wide spread as in the TC case (Fig. 82). This indicates that the compressive loads of the TC fatigue cycle cause additional debonding of the 0° fibers.

In addition to the 0° debonding, the 90° debonding was also more extensive. In the TT case, the 90° debonding occurred primarily on the top and bottom of the fibers, along the load line (*longitudinal debonding*). In the TC case, longitudinal debonding was present, but in addition, *transverse debonding*, or debonding perpendicular to the load occurred frequently (Fig. 83).

109
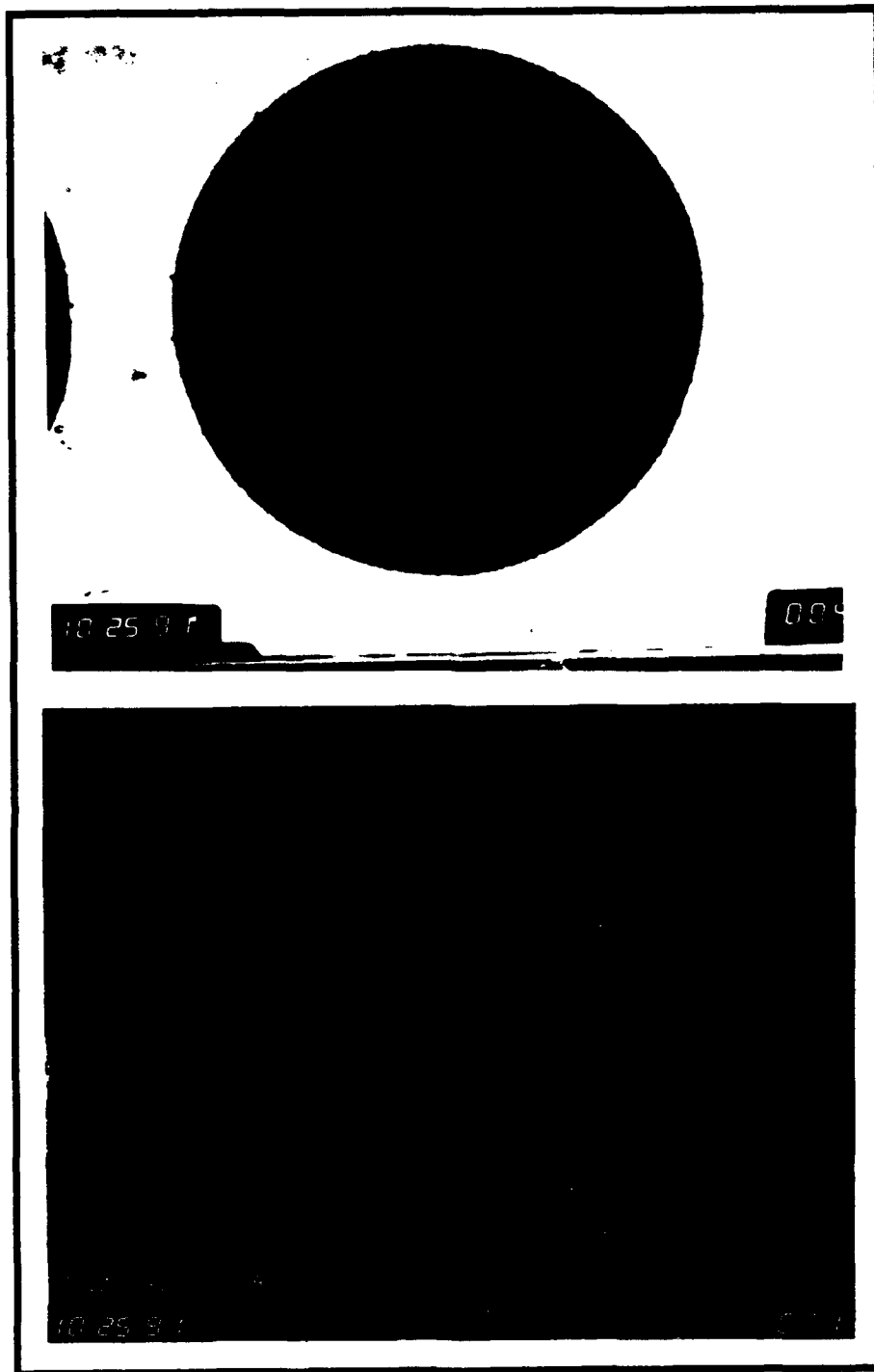
Figure 82. 600 TC RT (top) and 600 TT RT (bottom): 0° Debonding (500x)

Additional sites of matrix plasticity were also evident in the TC specimens. As mentioned in the micro-mechanic evaluation for TC RT, plasticity was found in the matrix

110

region directly above and below the 90° fibers, along the load line. Although this plasticity was not found to nucleate matrix cracks, it is an indication of the difference in the state of stress for the two load cases. These additional sites of 90° debonding and matrix plasticity are illustrated in Fig. 83.

Stress Range. Directly contrasting the maximum stress comparison, Fig. 84 clearly shows that on a stress *range* basis, the TC fatigue lives are much longer than the TT fatigue lives. Thus, it is evident that although additional deformation mechanisms exist within the TC load case, the compressive load comprising half of the load range in the TC case is not as detrimental as a load range comprised of tensile loads twice that value (i.e., the TT load case).

This difference can be explained, in part, by the tensile mean stresses present in the TT case. Mean stress is defined as the average of the maximum and minimum stress:

$$\sigma_m = \frac{\sigma_{max} + \sigma_{min}}{2} \qquad (4)$$
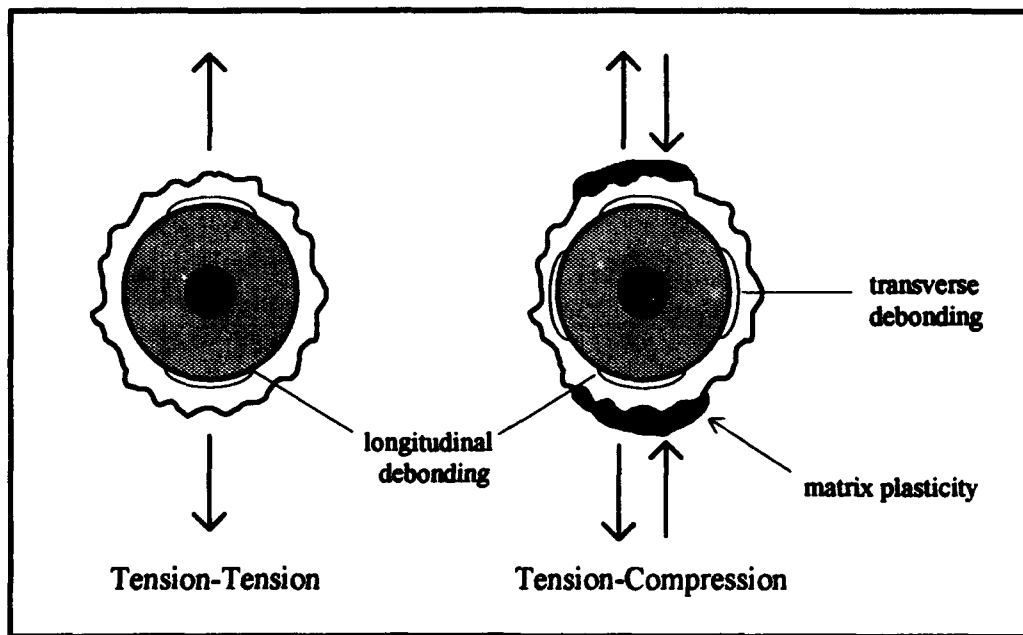
Figure 83. Debonding and Matrix Plasticity: TC RT vs. TC RT

111
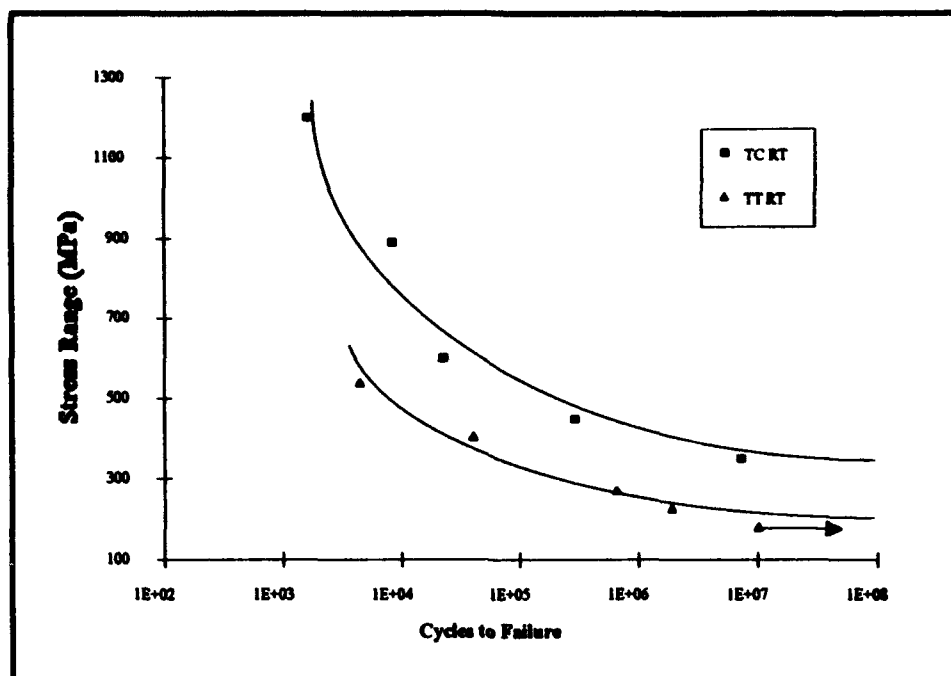
Figure 84. Stress Range SN Curve: TC RT vs. TT RT

Therefore, the TT specimens experienced a positive, or tensile mean stress, while the TC specimens experienced no mean stresses. As previously discussed (see Chapter 2), the mean stress can have a substantial influence on fatigue behavior, with tensile mean stresses being detrimental to fatigue life. Thus, the tensile mean stresses present in the TT tests appear to have had an adverse effect on the fatigue lives of these specimens as compared to the TC fatigue lives on a stress range basis.

Lerch and Halford (26), in their research of a $[\pm 30]_{8s}$ SCS-6/Ti-15-3 laminate under strain-controlled fully-reversed fatigue, also found that on a stress range basis, the TC fatigue lives were several orders of magnitude greater than load-controlled TT fatigue lives. They reported that this was due, in part, to the tensile mean stresses in the TT tests, and thus employed a modified Goodman equation in an attempt to correct for these stresses. They believed that this correction would yield a better comparison between the TT and TC data. Yet, the corrected data again resulted in TT fatigue lives lower than TC fatigue lives, by one order of magnitude.

112

A physical interpretation of the tensile mean stress is that any existing cracks in the TT specimen will remain open throughout the fatigue cycle. In contrast, cracks in the TC specimens with zero mean stresses will be subjected to closure for a significant portion of the fatigue cycle. Thus, fatigue crack growth would appear to be greater in the TT case, thereby reducing the TT fatigue life in comparison to the TC fatigue life at the same stress range. This can be illustrated by comparing the stiffness reduction of the 450 MPa TT and 225 MPa TC specimens, with comparable stress ranges of 405 and 450 MPa respectively. Figure 85 clearly shows that equivalent stress ranges in TC and TT do not yield similar stiffness responses or fatigue lives. This can be explained by the fact that the slow rate of matrix cracking which occupied 98.2 percent of the 225 TC RT fatigue life was maintained by the continual crack closure caused by the compressive portion of the fatigue cycle. The specimen eventually reached a saturation state during which minimal crack propagation occurred, and the stiffness plateaued. In contrast, matrix cracking was very
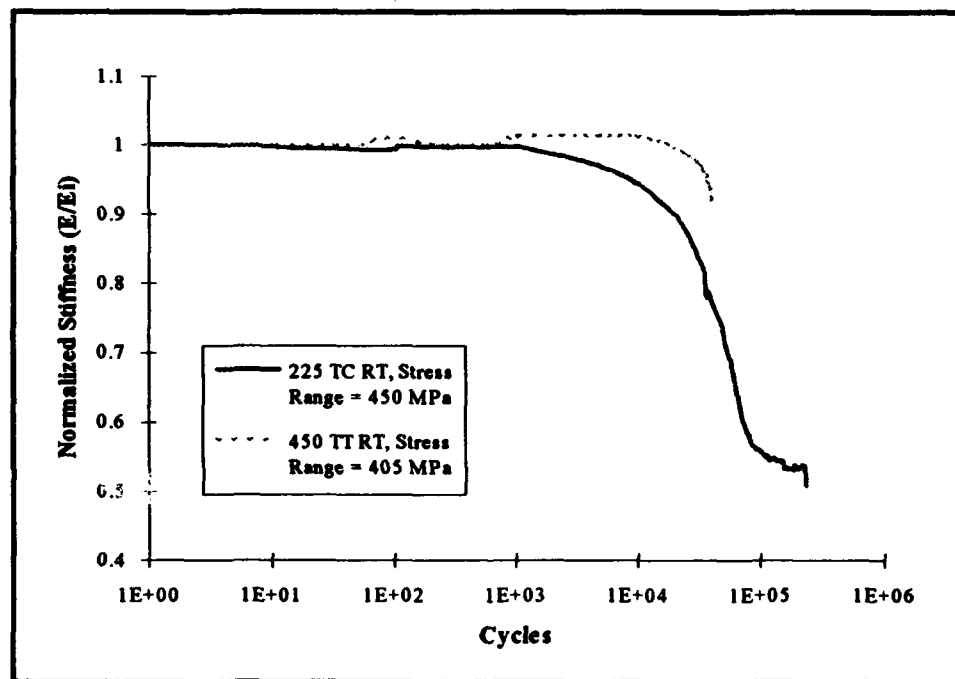
Figure 85. Stiffness Response Comparison: 225 TC RT vs. 450 TT RT

113

much accelerated in the 450 TT RT test, occupying only the final 22 percent of the fatigue life, and a stiffness plateau never occurred. Thus, it is apparent that the stress range criterion does not yield an accurate measure by which to compare data collected at R-ratios of 0.1 and -1.

Strain Range. Majumdar and Lerch (30) have reported that the strain range criterion, not the applied strange criterion discussed above, is a more fundamental parameter controlling the fatigue lives of MMCs. In their study of tension-tension fatigue of unidirectional SCS-6/Ti-15-3 laminates with 15, 35, and 41 percent volume fractions they found that on a strain range basis, the fatigue life data fell within a relatively narrow band, particularly at strain levels below 0.6 percent. Additionally, the matrix material agreed reasonably well at strain levels below 0.5 percent. Therefore, they concluded that MMC fatigue life is strain range controlled, especially in light of the well established fact that the fatigue life of metals is strain range controlled.

With this in mind, the TT and TC strain range fatigue life curves are plotted in Fig. 86. As can be seen, the data does not converge, as mentioned above, but yields a similar comparison as the stress range criterion. If, however, one considers only the portion of the strain range which places the matrix in tension, a better comparison can be made. This is due to the fact that if crack propagation is a dominant damage mechanism, its growth will be reduced in tension-compression, since the crack is forced into closure for approximately half of the cycle, or approximately half the strain range.

This crack closure can also be thought of on a crack-tip intensity (K) basis. Elber (6) introduced the idea of an effective stress intensity factor range (ΔK_{eff}), during which the fatigue crack is fully open, which he maintained that it is necessary for the fatigue crack growth to occur. He defined K_{open} as the stress intensity factor when the crack is
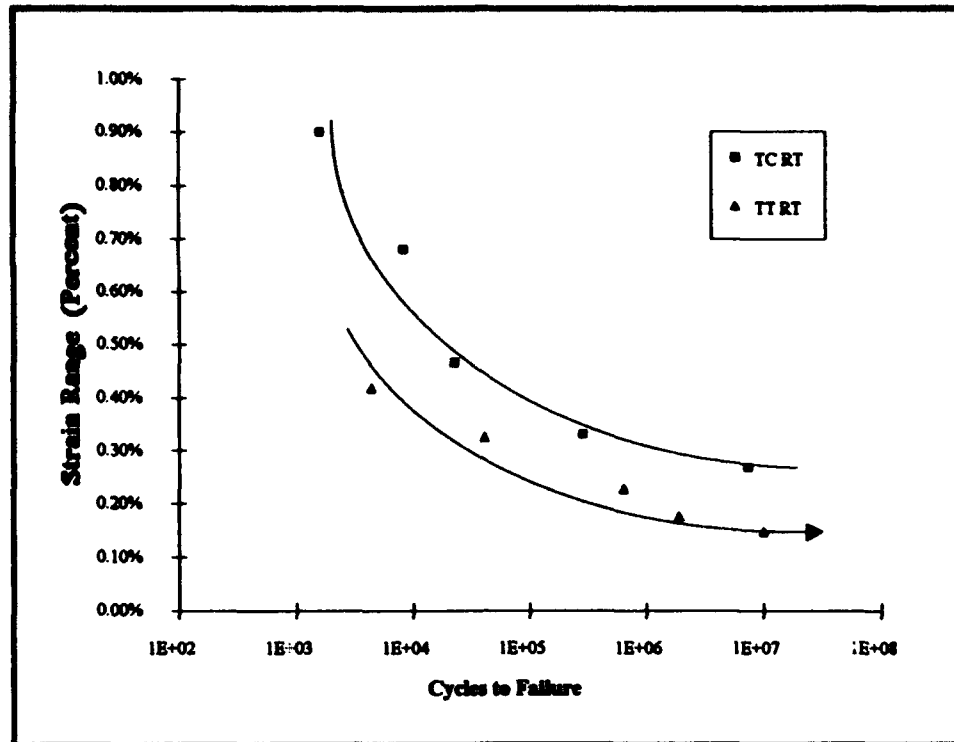
Figure 86. Strain Range SN Curve: TC RT vs. TT RT

fully open, further defining ΔK_{eff} as the difference between the K_{open} and the maximum stress intensity factor, K_{max}:

$$\Delta K_{eff} = K_{max} - K_{open} \qquad (5)$$

He concluded that the crack growth rate should be based on this effective stress intensity factor range:

$$\frac{da}{dN} = f(\Delta K_{eff}) \qquad (6)$$

Thus, although the quantitative values for the crack tip intensity values which occurred during the TC tests are unknown (these are obtainable only by performing further tests), a reasonable estimate is that K_{open} will not be reached while the specimen is loaded in compression. Thus, ΔK_{eff} can be estimated by dividing the ΔK by a factor of two. In the

115

same manner, the effective strain range, ε_{eff}, can be estimated by dividing the strain range observed during the steady state strain portion of the fatigue life, by a factor of two. The effective strain range for the TC tests, and the effective (also the full) strain range for the TT tests are plotted as a function of fatigue life in Fig. 87. It is clear that this yields a better comparison than the full strain range, stress range, or maximum stress criterions.

TC RT vs. TC HT Comparison

Previous studies have shown that both the stiffness and ultimate strength (UTS) of the [0/90]$_{2s}$ SCS-6/Ti-15-3 laminate decrease with an increase in temperature. Portner (40) reported a 7.58 percent decrease in stiffness and a 16.86 percent decrease in UTS (from 890 to 740 MPa) at 427° C. Majumdar (37) reported a 36.3 and 33.3 percent decrease in yield strength and UTS respectively for a unidirectional laminate of the same material at 538° C. With this in mind, one might expect that, for equivalent applied
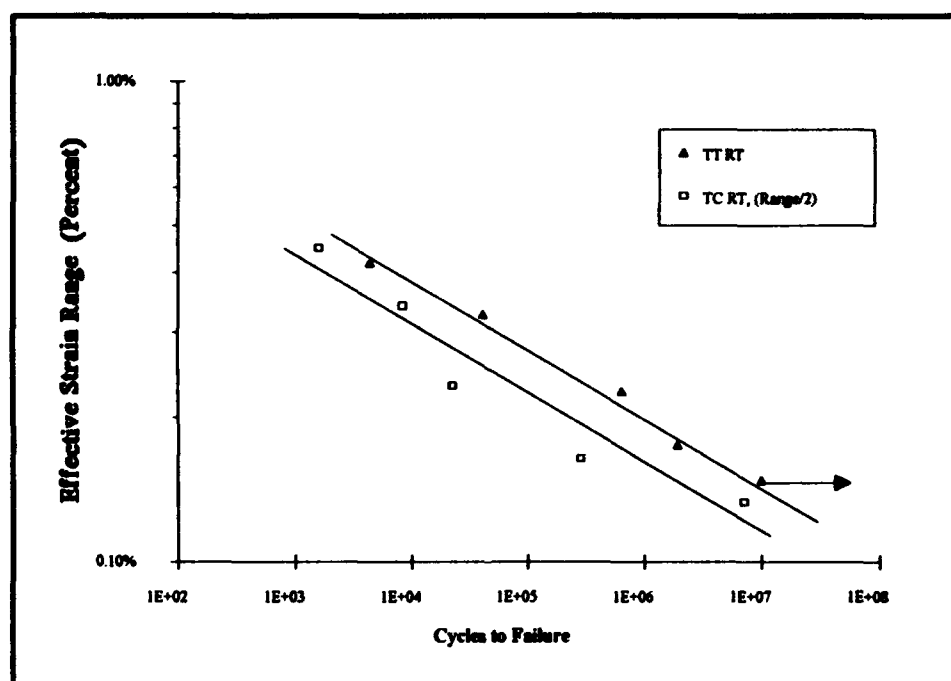
Figure 87. Effective Strain Range SN Curve: TC RT vs. TT RT

116

stresses, the fatigue lives at high temperature would be shorter than those at room temperature. However, in the high stress range, fatigue lives at both temperatures were found to be equivalent, and at intermediate stress levels, the fatigue lives diverge, the HT specimens actually having much *longer* fatigue lives than the RT specimens (Figs. 88 and 89). Thus, the elevated temperature has little effect on specimen failure in the fiber dominated region of the SN curve, but begins to take effect in the portion of the curve in which the matrix takes a more dominant role. This is expected, since the fibers are not affected by increases in temperature up to 1100°C (39). Also of interest is that on a strain *range basis*, the TC HT specimens had equivalent lives in the high strain range region, but at intermediate and small strain ranges, the TC HT specimens had longer fatigue lives (Fig. 90). This is an indication that the material can withstand larger strain ranges at elevated temperature before specimen failure occurs.
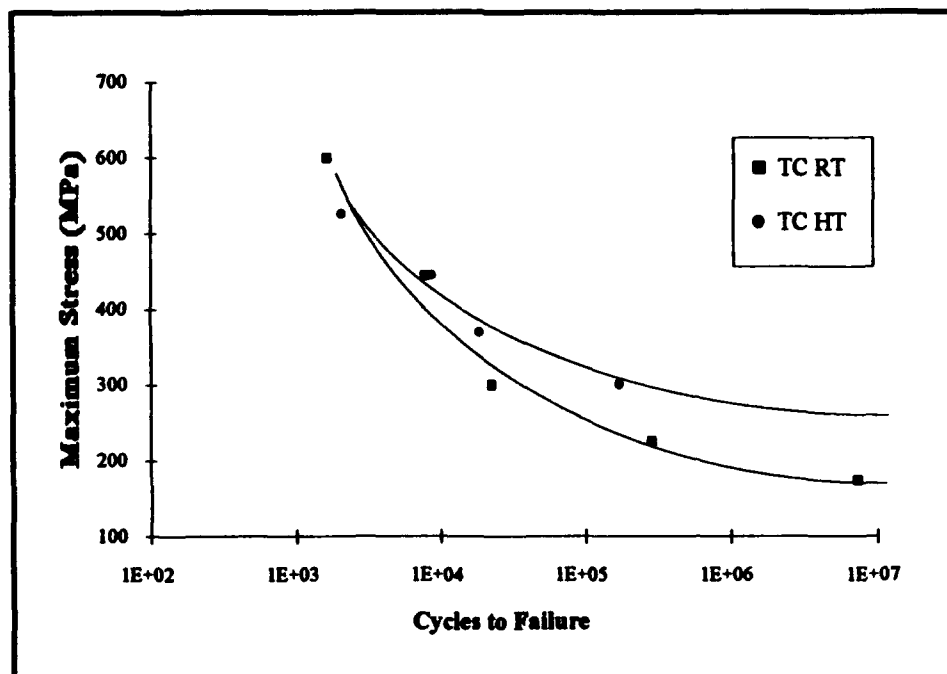
Figure 88. Maximum Stress SN Curve: TC RT vs. TC HT
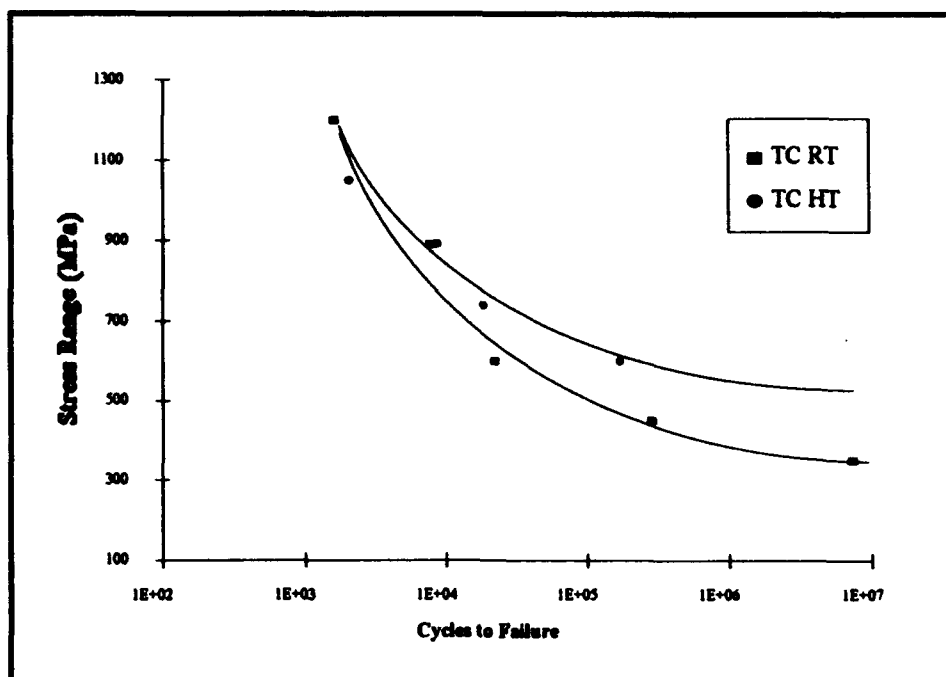
Figure 89. Stress Range SN Curve: TC RT vs. TC HT
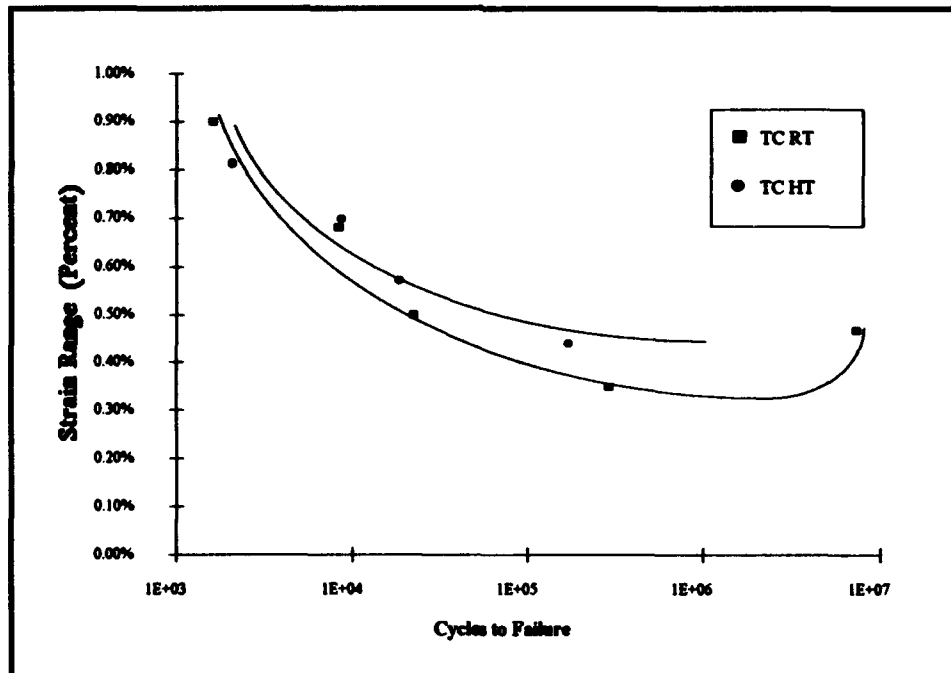
Figure 90. Strain Range SN Curve: TC RT vs. TC HT

118

To illustrate this point, the strain response of two tests which were found to be strongly influenced by fiber failure, the 445 MPa RT and HT tests, are plotted in Fig. 91. With nearly identical fatigue lives of 8,296 and 8,501 cycles respectively, the strain response for both the RT and HT specimens were nearly identical. Thus, it is evident that the increase in temperature had little effect on the fiber strength which dominated failure at this stress level. This is in accordance with research presented by Pollock and Johnson (39) in which the SCS-6 fiber strength and stiffness were found to be virtually unaffected by increased temperatures up to 1100° C. Therefore, it is concluded that the increase in temperature to 427° C does not influence the fatigue lives, or the stiffness and strain responses, of the specimens fatigued in the primarily fiber-dominated region of the SN curve. Figure 91 clearly demonstrates this theory.

Conversely, the effect of the increase in temperature strongly influenced the fatigue lives and strain responses of the matrix dominated tests, such as the 300 MPa tests. The
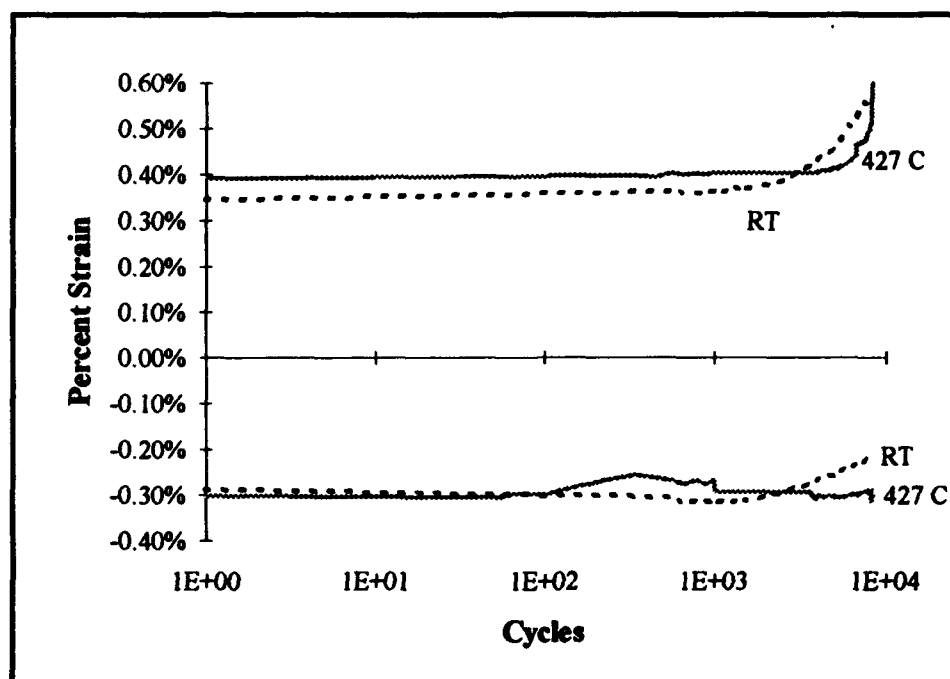
Figure 91. Percent Strain vs. Cycles: 445 TC RT and 445 TC HT

two HT specimens cycled at this stress level had fatigue lives of *6.93 and 7.66 times longer than* their RT counterpart. Additionally, significant differences can be observed between the RT and HT strain responses (Fig. 92). The RT specimen strain continually increased throughout the 22,297 cycle fatigue life, and the edge replica evaluation indicated that the matrix cracking began at approximately 1,000 cycles and continued for the remaining 95 percent of the fatigue life. In contrast, the HT specimen strain remained virtually constant throughout the first 50,000 cycles of the 170,900 cycle fatigue life, and edge replica evaluation indicates that the matrix cracking began at approximately 52,000 cycles, and continued for the remaining 70 percent of the fatigue life. Thus, it is strongly suggested that the onset of matrix cracking is delayed by the increase in temperature, and that once it begins, matrix cracking occupies less of the fatigue life than at room temperature.

However, to substantiate such a claim, one must examine the micro-mechanic
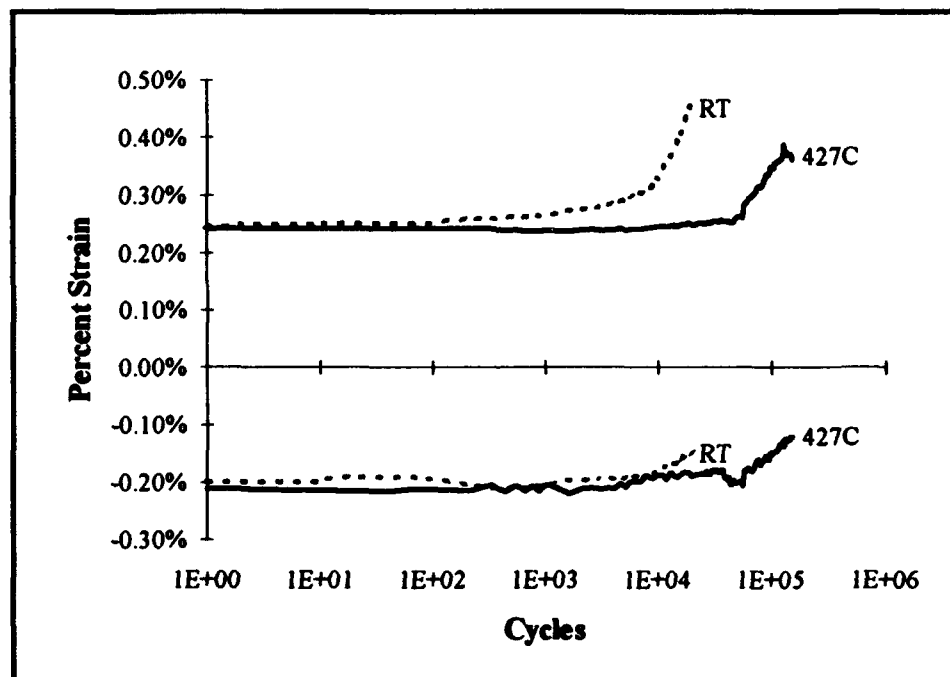
Figure 92. Percent Strain vs. Cycles: 300 TC RT and 300 TC HT

response of the material. Two major differences in the damage mechanisms were observed during the micro-mechanic evaluations. First, the *crack pitch*, defined as the average distance between matrix cracks (2:295), was extremely large at high temperature. The majority of these few matrix cracks, however, had grown to span the entire thickness of the specimen at failure. In contrast, the crack pitch was orders of magnitude smaller for the RT tests. Of the many matrix cracks which existed at failure, many spanned only one to two plys, with some bridging $0°$ fibers to span the full specimen thickness. These differences can be easily seen by comparing photomicrographs of the specimen edges after failure (Fig. 93).

The above observations lead to the conclusion that the titanium matrix and the fiber-matrix reaction zone become more ductile at the elevated temperature. This increased ductility was also reported by Majumdar (28:22) in his monotonic testing of a $[90]_8$ SCS-6/Ti-15-3 laminate. He reported that the fiber-matrix bond strength increases as a result of the ductility of the reaction zone. Lerch and Saltsman (27) also observed this phenomenon in their monotonic tension tests at $427°$ C. They reported that the increase in matrix ductility resulted in the almost total absence of matrix cracks.

The current research is the first report to document the effect of this increased ductility on the fatigue lives of SCS-6/Ti-15-3. The enhanced ductility of the brittle reaction zone is a significant finding, since the cracks emanating from these regions have been found in the current research, and in much of the literature, to be the primary cause of fatigue crack nucleation in titanium based MMCs. Thus, the increased ductility resulted in the delayed onset of matrix cracking, and the much larger crack pitch of the matrix cracks (i.e. cracks were few in number). These mechanisms resulted in enhanced fatigue life of the tested MMC under tension-compression fatigue condition at elevated temperature.
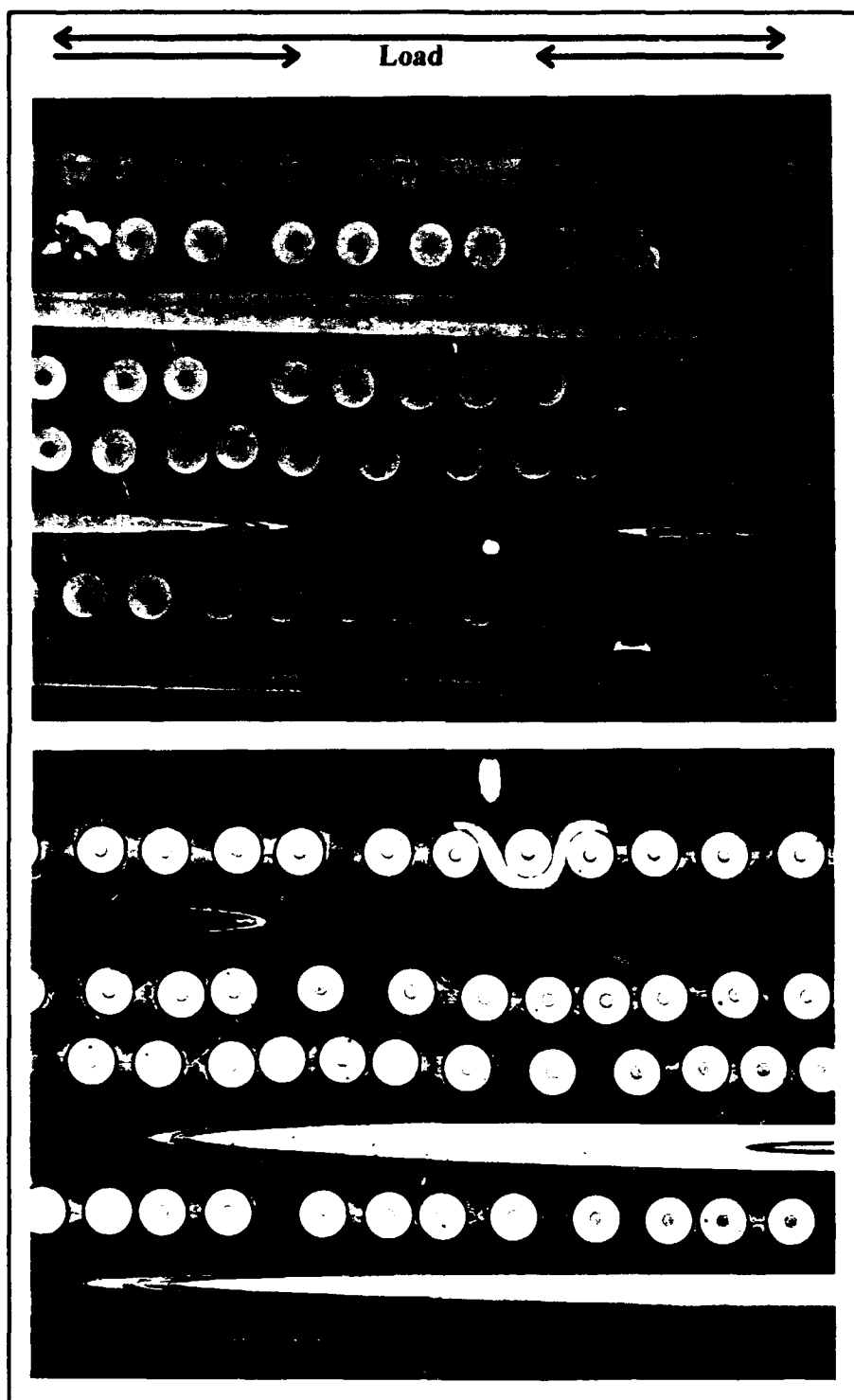
Figure 93. Matrix Cracking, 300 TC RT(top) and 300 TC HT (bottom)

In addition to the delayed onset and reduced occurrence of matrix cracking, the extremely well defined planar slip which occurred often at room temperature became much more diffused at higher temperature (Fig. 94). This can be explained by the increased atomic mobility of the slip mechanism at higher temperature. At room temperature, the slip mechanism results from dislocation motion along an atomic lattice network. New dislocations which form in the vicinity move along these previously deformed paths since this requires a minimum amount of energy. Thus, under fatigue loading, the resulting slip band becomes very well defined due to the repetitive nature of the dislocation motion. In contrast, at higher temperatures, the atomic mobility is increased, and the dislocations are no longer confined to previously deformed lattices. This results in slip which is much less defined at high temperature. This transition from planar to diffused slip at elevated temperature was also observed by Newaz and Majumdar (37) in their elevated temperature monotonic testing of the [0/90]$_{2s}$ laminate. Figure 94 illustrates the difference in the planar and diffused slip seen at room and elevated temperatures, respectively. Note the very distinct slip bands emanating from the matrix crack in the TC RT photomicrograph, as compared to the white regions surrounding the matrix crack in the TC HT photomicrograph.
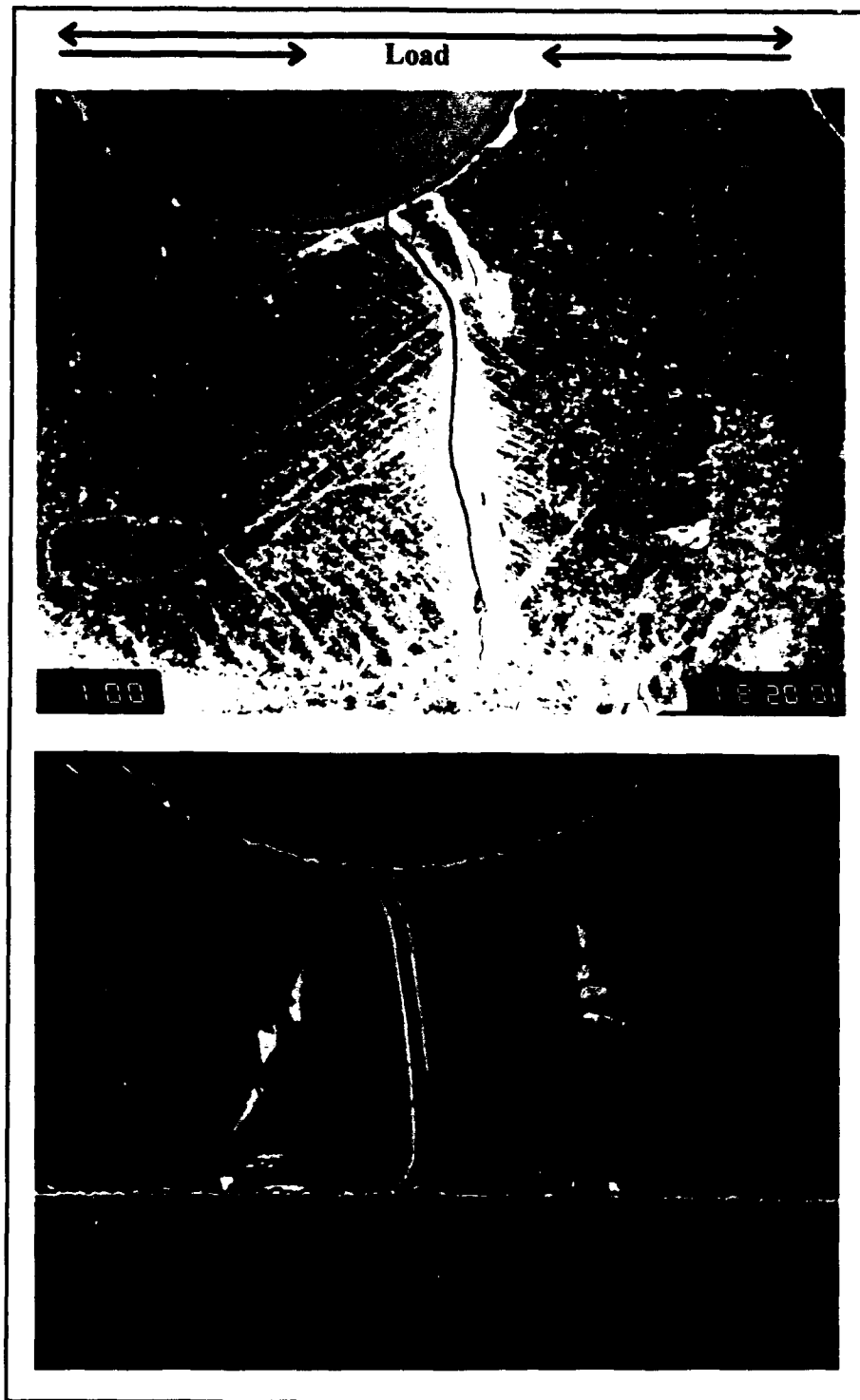
Figure 94. Planar vs. Diffused Slip, 445 TC RT (top) and 370 TC HT (bottom)

Overall Comparison: TC RT, TT RT, TC HT

The three load cases examined in this study represent three very distinctly different loading conditions, which in turn result in differences in the respective fatigue lives, or SN curves. On a maximum stress basis, the TT RT condition yielded the longest fatigue lives. The TC RT condition yielded the shortest fatigue lives, with the TC HT condition resulting in similar fatigue lives in the high stress range, but with longer lives in the intermediate stress range. The shorter fatigue lives of the TC specimens as compared to the TT specimens was found to be caused by the additional damage sites which resulted from the superposition of the compression portion of the load cycle.

However, on a stress range basis, the TC RT and TC HT specimens had much longer lives than the TT RT specimens. This was found to be due to the detrimental mean stress effects present in the TT RT load case. The strain range basis yields a similar comparison. The most promising comparison between the three cases is that of the effective strain range. The effective strain range vs fatigue life data, and the corresponding best fit line and fatigue scatterband are plotted in Fig. 95. The data, with the exception of two points, falls within the scatterband. Thus, it is suggested that the effective strain range is a good parameter for comparing fatigue lives under different loading conditions.

METCAN Analysis

METCAN is a FORTRAN computer code which was designed to perform both linear and nonlinear analysis of fiber reinforced metal matrix composites. The code uses a multi-cell model (MCM) composed of a unique set of micro mechanics equations developed by Hopkins and Chamis (17) for analyzing MMCs at high temperatures.
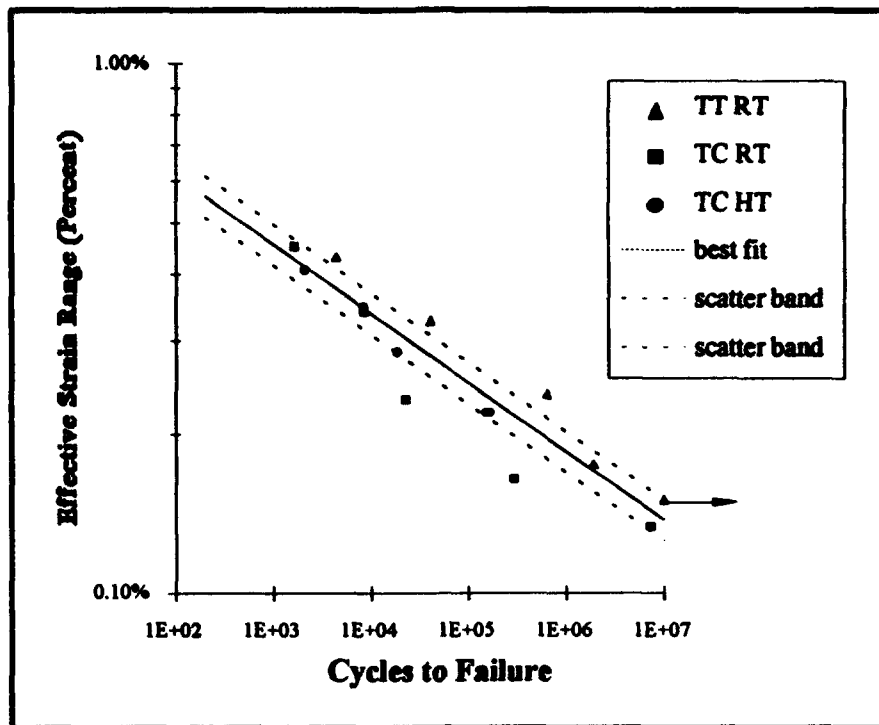
Figure 95. Effective Stress Range SN Curve: TC RT, TT RT, TC HT

The building block of the MCM is the unit cell, which is broken down into three sub regions in an effort to characterize the through-the-thickness non uniformity of structure and constituent material properties (Fig. 96). Using the complete set of micromechanic equations which can be found in (16), the program determines the microstresses for the fiber and matrix regions, which will be used in the following discussions.

Several assumptions are made in the code which are important to keep in mind. It is assumed that all fibers within a ply are continuous and parallel, that the properties of all fibers are identical, and that complete bonding exists between the fiber and matrix (17:4). Although these assumptions simplify the code, they contribute to differences in the predicted laminate properties as compared to the experimental values. For example, METCAN generated a Young's modulus of 150 GPa for the [0/90]$_{2s}$ laminate, a twelve percent difference from the experimental value of 133 GPa.
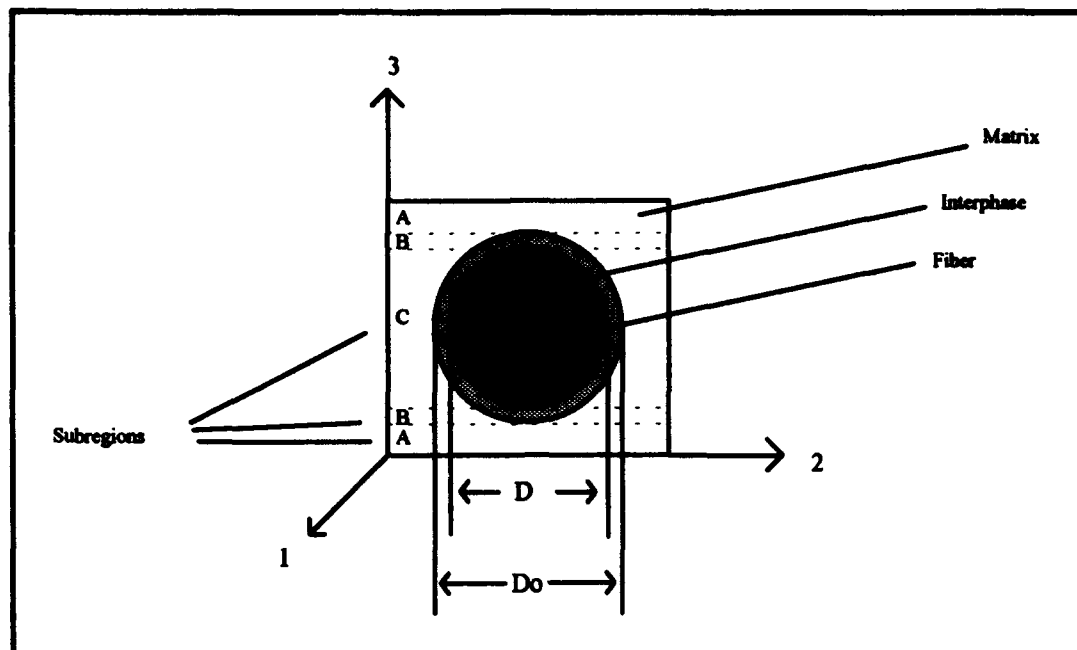
Figure 96. METCAN Unit Cell Model

Additionally, the initial stress state of the MMC before fatigue testing, must be understood. Most MMCs contain significant residual stresses due to the coefficient of thermal expansion (CTE) mismatch between the matrix metal and fiber, termed the "CTE mismatch-induced thermal stress" (50:101). In the SCS-6/Ti-15-3 MMC system, the matrix CTE is larger than that of the fiber. Thus, when the fiber and matrix are cooled from the stress-free fabrication temperature of 815° C (28, 45) to room temperature, the (theoretically) unrestrained constituents contract differently (Fig. 97). However, the fiber and matrix are bonded together, and thus, must contract the same amount (equilibrium state in Fig. 97). This results in a tensile residual stress state for the matrix material, and a compressive residual stress state for the fiber, both axially and radially. A consequence of these residual stresses is that micro-yielding may occur before macroscopic yield when the laminate is loaded mechanically (37). The residual stresses calculated by METCAN, using specified material properties which are found in the DATABANK file (Appendix C), are

127

presented in Table 7. The residual stresses for the 0° and 90° fibers and surrounding matrix are identical.

Table 7. Residual Stresses at Room Temperature

Stress*	Fiber	Matrix
Axial	- 410.65	137.62
Transverse	- 84.82	255.18
Through the Thickness	- 151.52	219.92
* Units of stress are MPa		

Fabrication @ Process Temperature

Constraint Free State
$\alpha_{matrix} > \alpha_{fiber}$
@ Room Temperature

Equilibrium State
@ Room Temperature

= matrix

= 0 degree fiber

90 degree fiber
in compression

matrix in tension
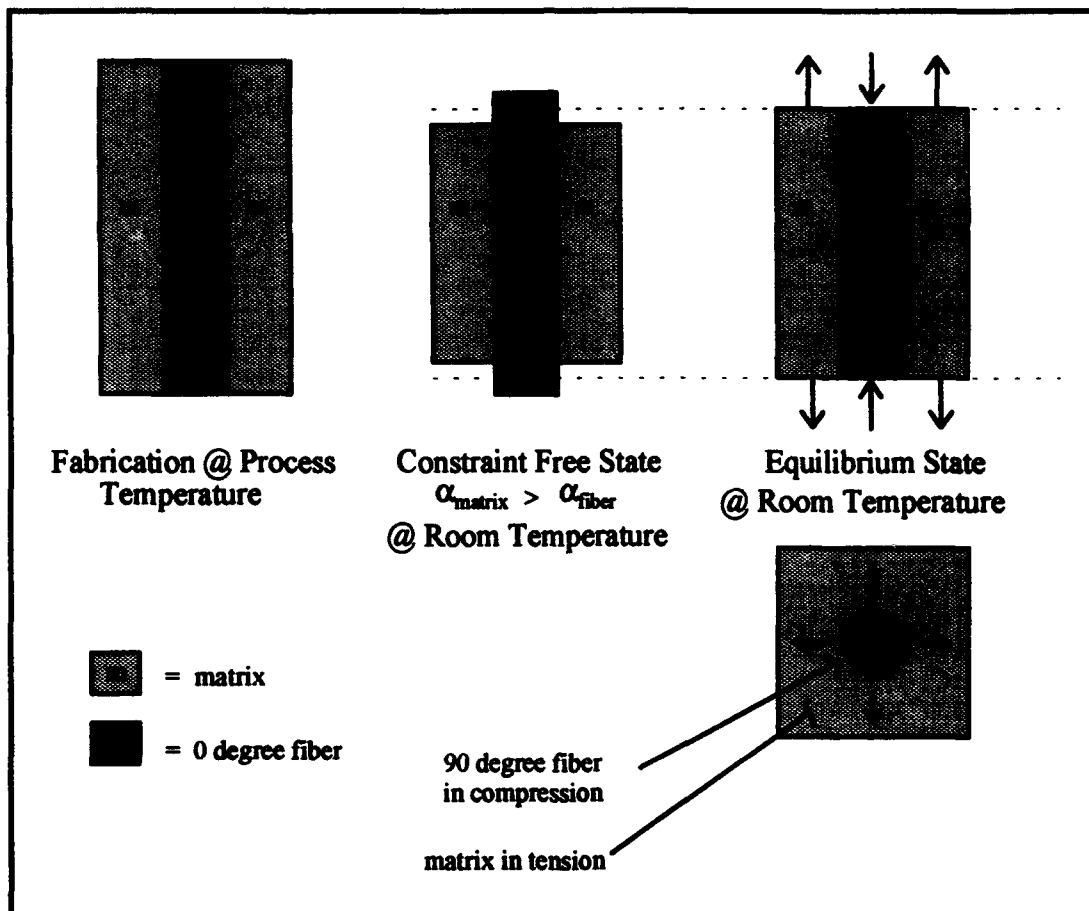
Figure 97. Residual Stresses Due to CTE Mismatch

TC RT vs. TT RT. Comparison of the fiber and matrix micro stresses for the TC RT and TT RT load cases result in similar comparisons as the actual experimental data. On a maximum fiber and matrix stress basis, the TT fatigue lives are longer than the TC (Figs. 98 and 99). Of particular interest, however, is that for the 600 TT and TC cases, the matrix stress is approximately 70 percent of the yield stress. Thus, as damage initiates and progresses within the specimen during fatigue cycling, it is clear that matrix stresses will eventually exceed the yield stress of the matrix.

A fiber and matrix stress range criterion again yields a similar comparison to the experimental results. Figures 100 and 101 clearly show that on a stress range basis, the TC specimens have longer lives than the TT specimens.
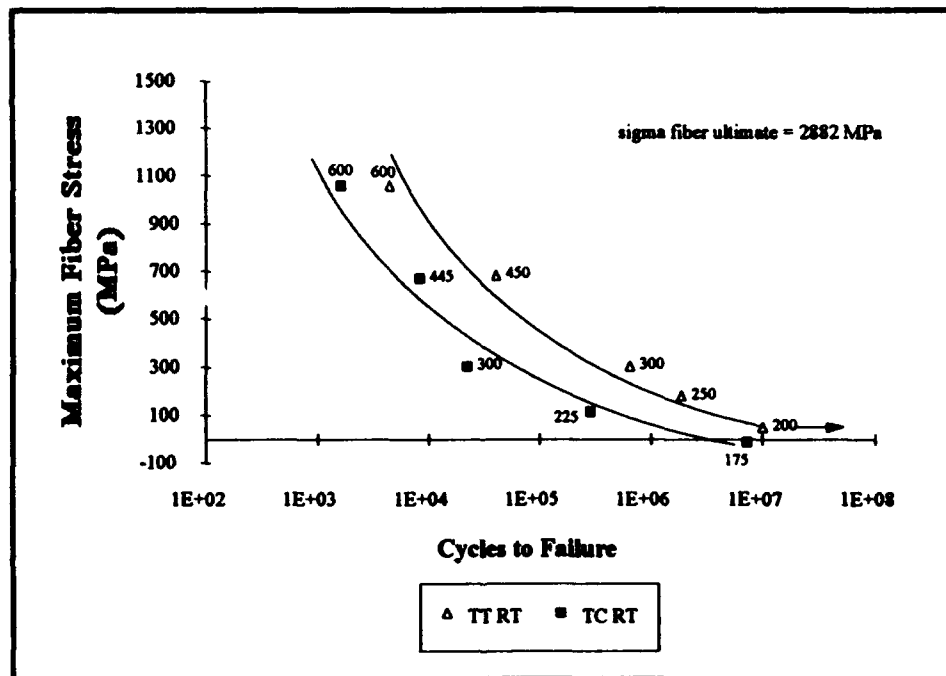
Figure 98. Maximum Fiber Stress vs. Fatigue Life: TC RT vs. TT RT
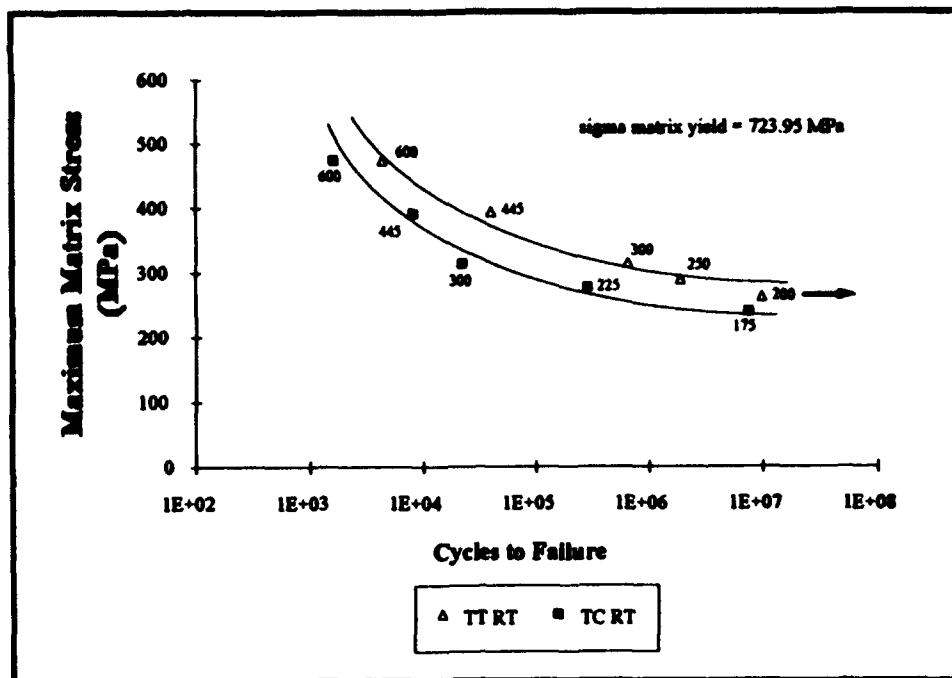
Figure 99. Maximum Matrix Stress vs. Fatigue Life: TC RT vs. TT RT
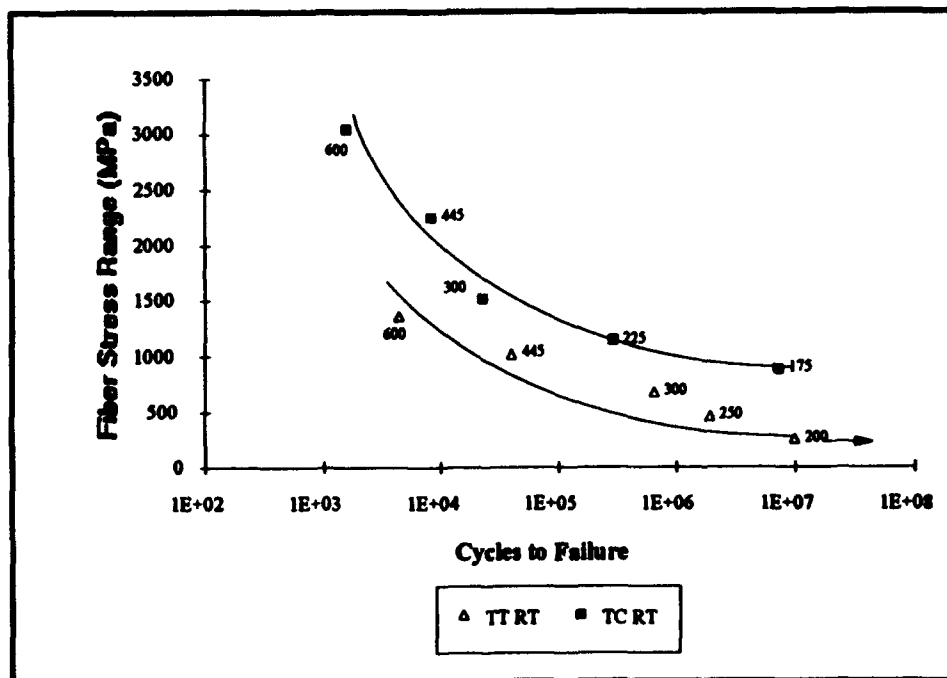
Figure 100. Fiber Stress Range vs. Fatigue Life: TC RT vs. TT RT

130
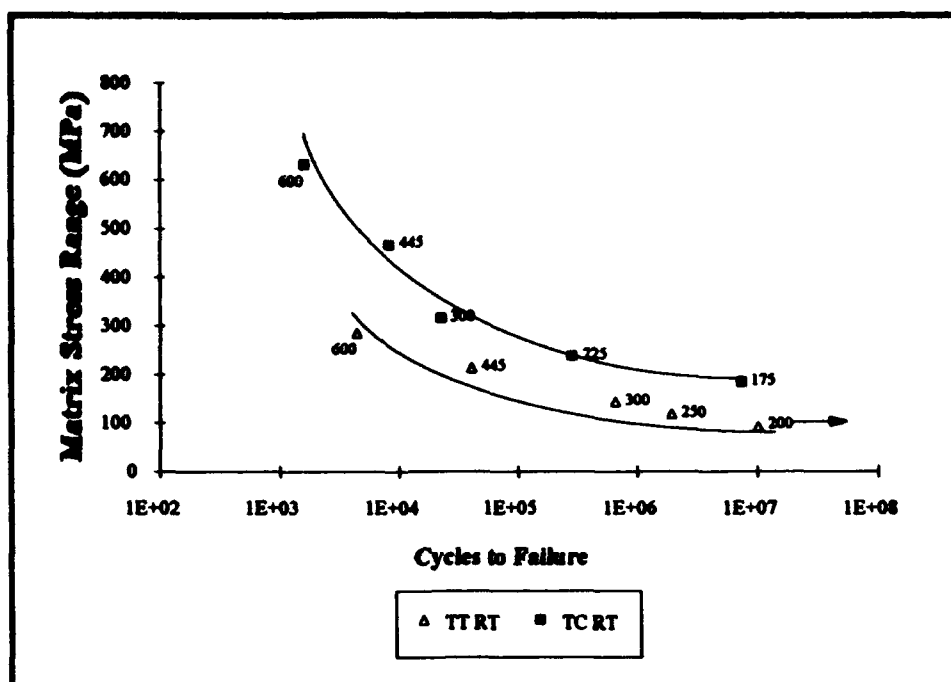
Figure 101. Matrix Stress Range vs. Fatigue Life: TC RT vs. TT RT

TC RT vs. TC HT. Constituent stress analysis for the RT and HT cases reveals the effect of the fiber and matrix residual stress relaxation due to the elevated test temperature. The residual stresses at 427° C and the percent decrease of these stresses from room temperature are tabulated in Table 8. The material property and sample input file are found in Appendix C.

The relaxation of the fiber compressive residual stresses at HT results in higher maximum fiber stresses for equivalent applied loads. This is shown in Fig. 102, in which

Table 8. Residual Stresses at 427° C

Stress*	Fiber (% reduction from RT)	Matrix (% reduction from RT)
Axial	-168.35 (59.01)	56.01 (59.30)
Transverse	- 37.77 (55.46)	109.53 (57.07)
Through the Thickness	- 65.35 (56.85)	94.80 (56.85)
*Stress units are MPa		

131

the maximum fiber stress is plotted as a function of specimen fatigue life. This increased fiber stress did not seem to effect the experimental results.

The relaxation of the tensile residual stresses on the matrix yields lower maximum matrix stresses for the HT specimens than for the RT specimens (Fig. 103). This may help to explain the longer fatigue lives of the HT specimens fatigued in the intermediate stress range.

On a fiber stress range basis, the RT and HT SN curves converge at the higher stress levels, but diverges at the intermediate to lower stress levels (Fig. 104). This is in direct correlation to the experimental data, indicating again that fatigue is dominated in the high stress regime of the SN curve.

On a matrix stress range basis, the two curves seem to converge in all regimes of failure (Fig. 105). Thus, it may be argued that since the matrix stress range is equivalent at RT and HT, the increased ductility, which is not modeled in the METCAN code, is the reason for the extended lives of the HT specimens at intermediate stress levels.
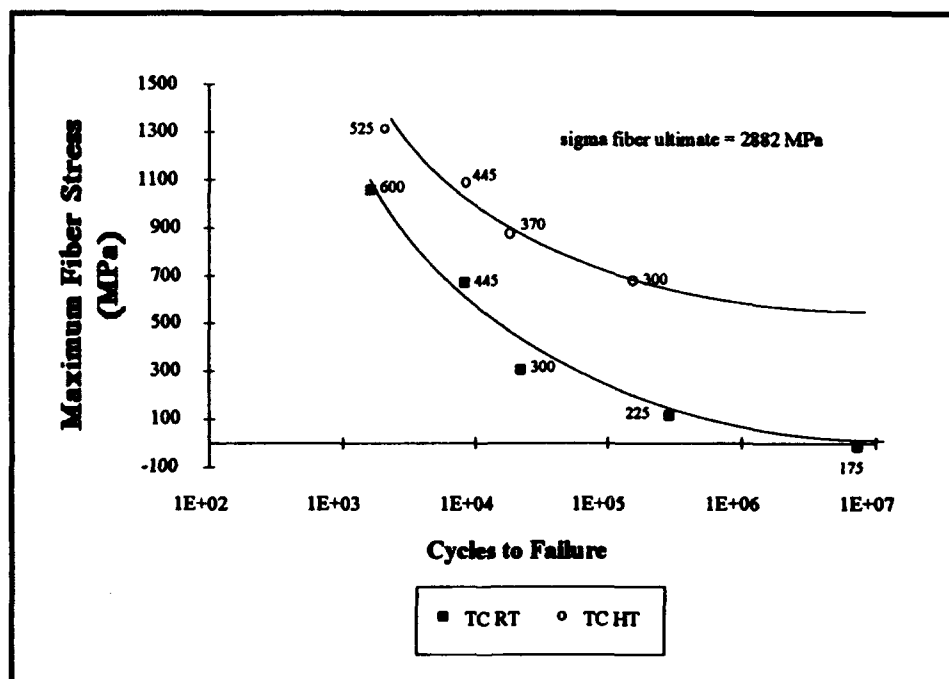
Figure 102. Maximum Fiber Stress vs. Fatigue Life: TC RT vs. TC HT

132
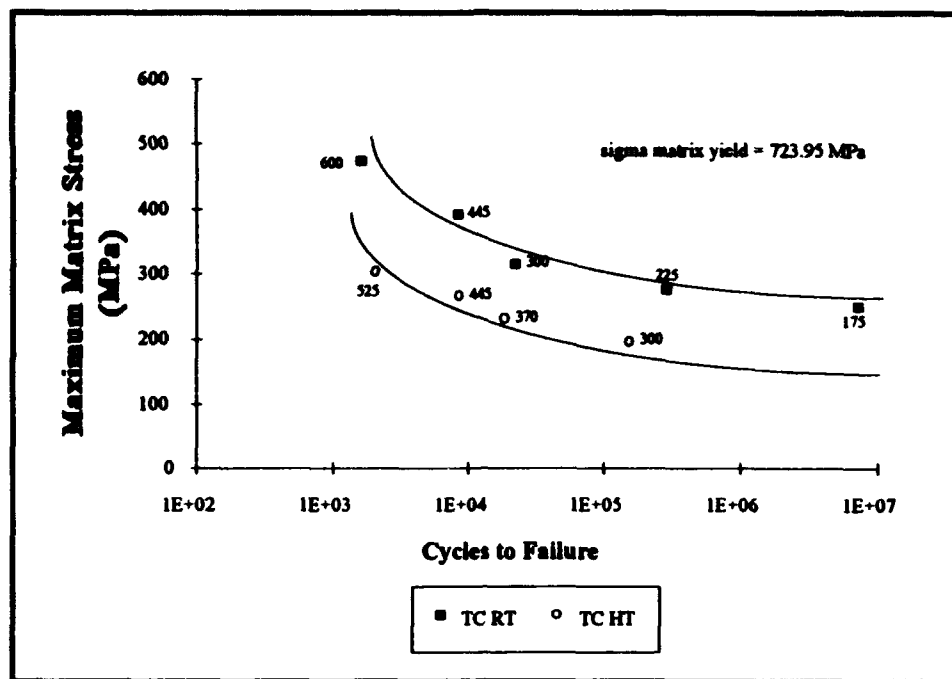
Figure 103. Maximum Matrix Stress vs. Fatigue Life: TC RT vs. TC HT
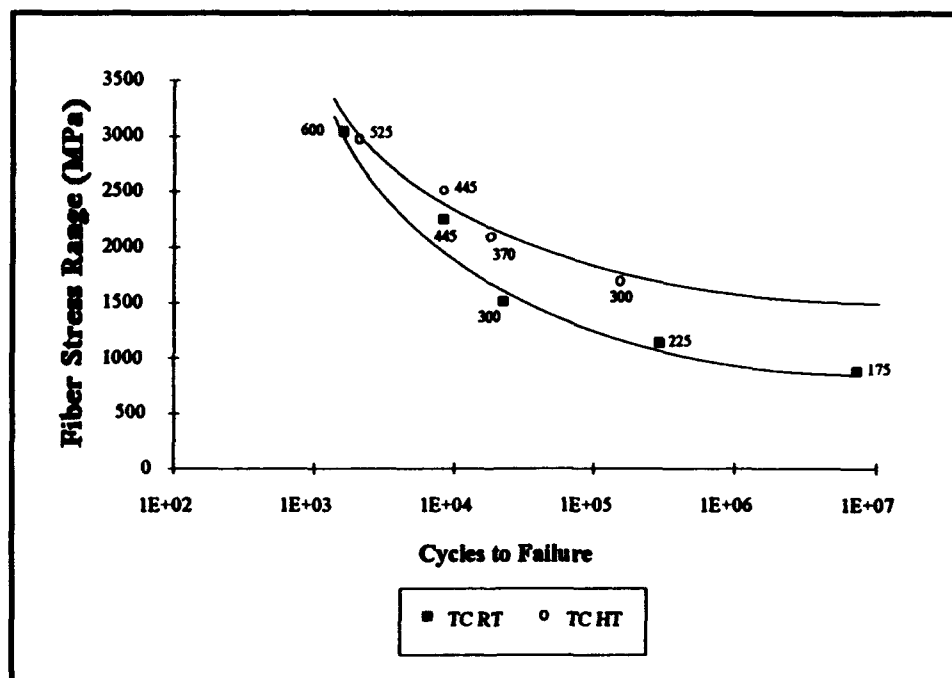
Figure 104. Fiber Stress Range vs. Fatigue Cycles: TC RT vs. TC HT
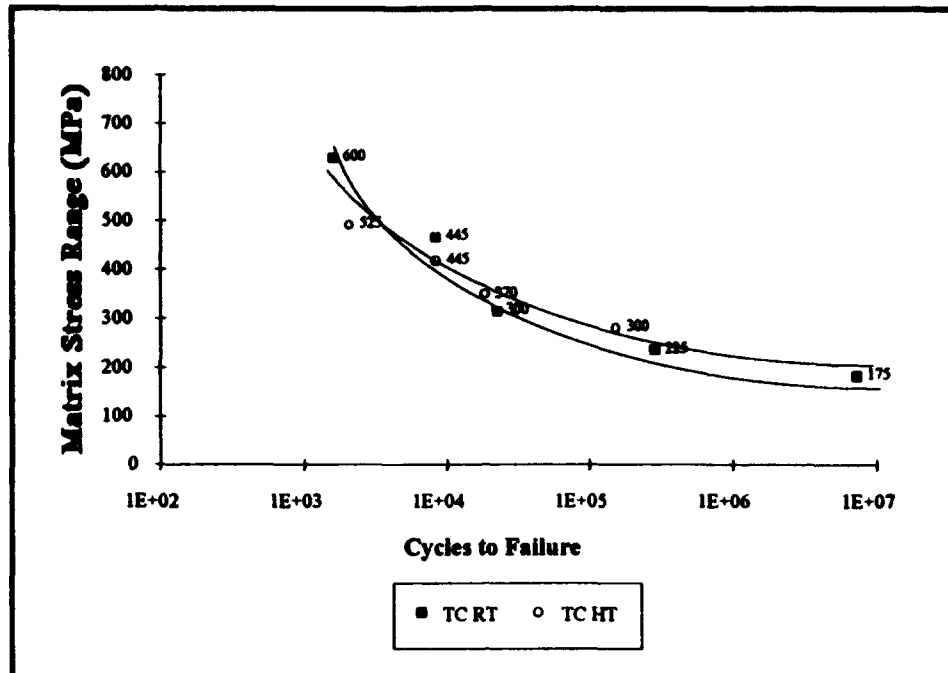
Figure 105. Matrix Stress Range vs. Fatigue Cycles: TC RT vs. TC HT

Comparisons of Results With Previous Studies

As mentioned earlier, there exists a lack of tension-compression data for MMCs in general, and also for SCS-6/Ti-15-3, thus, no comparison can be made of the current TC RT or TC HT data. However, more data exists for the more common tension-tension loading condition. Figure 106 compares fatigue life data of the present study with previous studies, plotted on a maximum stress basis, for both room temperature and high temperature (427° C) tension-tension fatigue at R-ratio = 0.1.

Several observations can be made from this figure. First, the agreement is excellent between Johnson *et al.*'s (21, 22) room temperature data and the current TT RT data. Furthermore, the current data is a significant addition to Johnson *et al.*'s, since their work spanned a very small portion of the SN curve in comparison to the current data, with fatigue lives from 5,000 to 40,000 cycles only. Additionally, Portner's (40) high

134
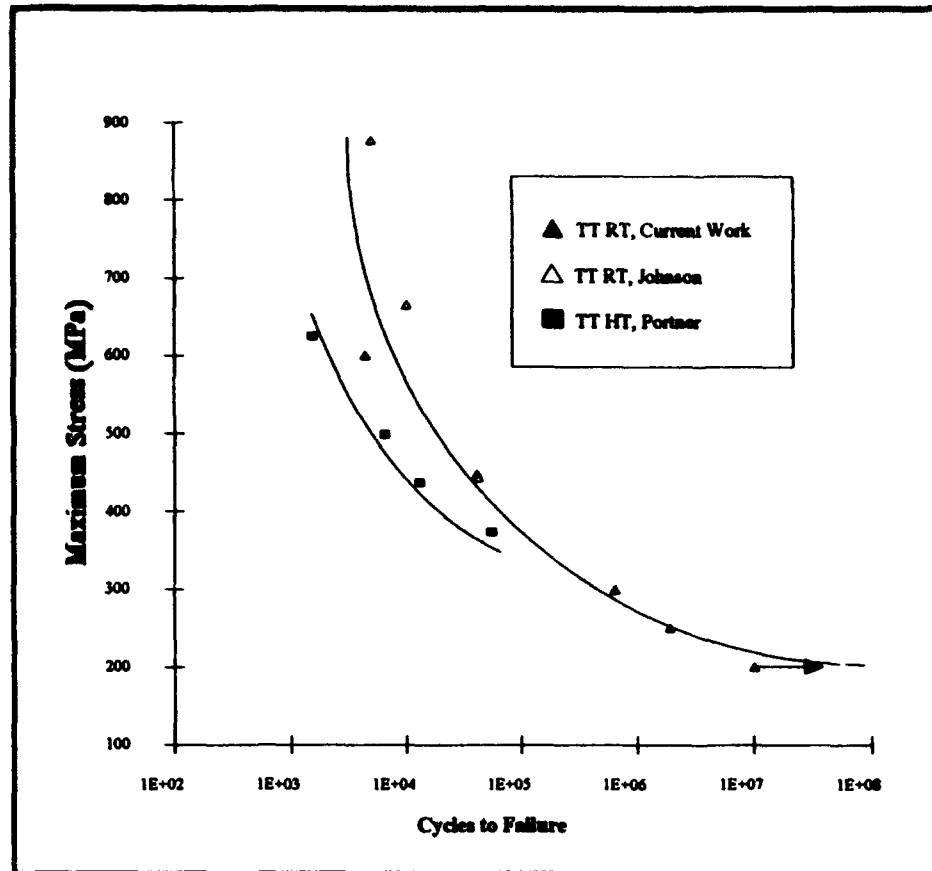
Figure 106. Maximum Stress Tension-Tension SN Curve

temperature data reveals fatigue lives shorter than the room temperature fatigue lives at equivalent stress levels. This is very interesting, as it indicates that the extension of fatigue life at elevated temperature (observed in the 370 and 300 MPa TC HT tests) does not occur in tension-tension loading.

The TC RT, TT RT, and TC HT fatigue life data from the current work are plotted together with neat (unreinforced) matrix, and unidirectional (volume fraction 0.15 and 0.35) fatigue life data (32) in Fig. 107. This figure indicates that the fatigue life data converges for the unidirectional laminates with different volume fractions. However, the cross-ply fatigue lives are much shorter in comparison to unidirectional laminate at any given strain range. It is obvious that the damage which is initiated by the 90° plies of the

135
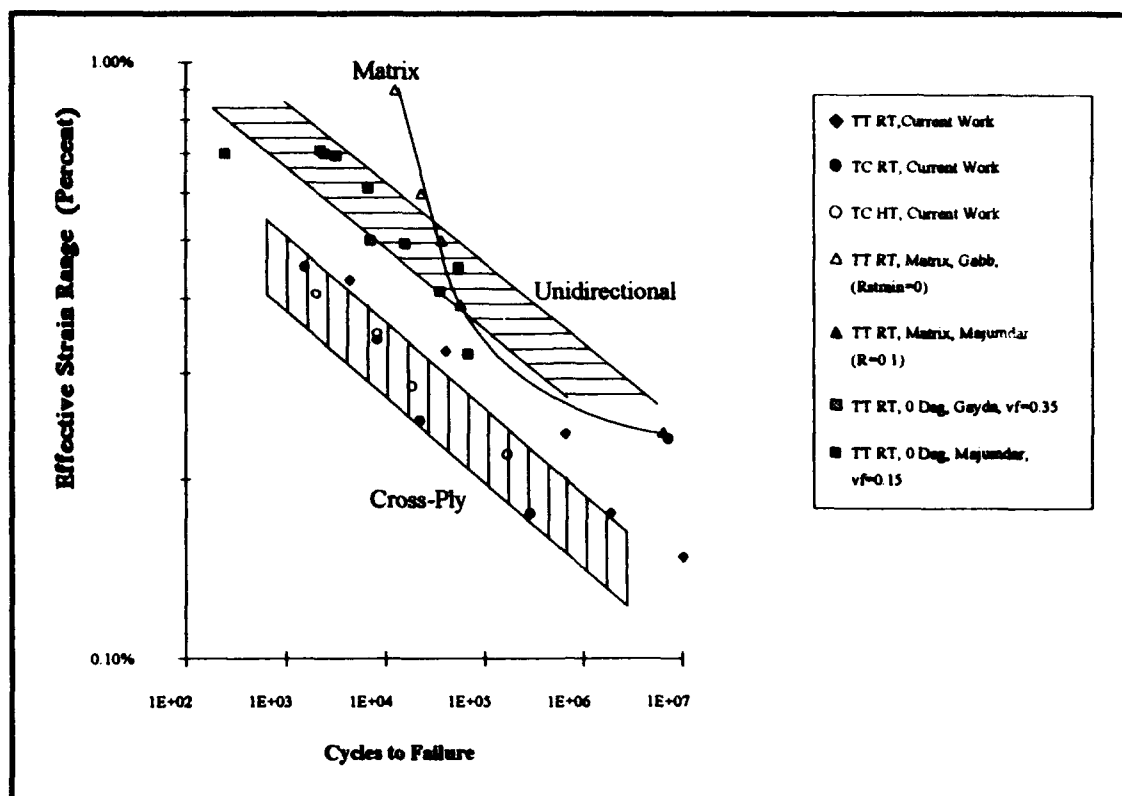
Figure 107. Effective Strain Range SN Curve

cross-ply laminate causes the shorter fatigue lives. It is also evident that for all strain ranges, the cross-ply laminate has shorter fatigue lives than the neat matrix. This again can be attributed to the presence of the 90° fibers.

VI. Conclusions and Recommendations

The purpose of this study was to extend the existing knowledge of fatigue damage mechanisms for the SCS-6/Ti-15-3 MMC under fatigue loading. Due to the complexities associated with tension-compression fatigue testing, very little data has been published for this load condition. This is the first known research to be performed on a MMC under load controlled, fully-reversed tension-compression fatigue.

The effects of the tension-compression fatigue condition were made based on the comparison with tension-tension fatigue data also performed in this study. It was found that on a maximum stress basis, the tension-compression specimens had shorter lives than the tension-tension specimens. This was due to additional damage and plasticity sites which existed only in the tension-compression load case. However, on a stress range basis, the tension-compression fatigue lives were longer than the tension-tension fatigue lives. This was found to be caused by the tensile mean stress effects. The most promising comparison of fatigue lives between the two cases was found to be based on the effective strain range, in which the strain range for the tension-compression case was divided by a factor of two and compared to the strain range of the tension-tension load case.

The effects of an isothermal elevated temperature of 427° C on the tension-compression fatigue of this MMC was also investigated. It was found that in the fiber dominated region of the SN curve, the fatigue lives at room and elevated temperature converged, but at intermediate stress ranges, the elevated temperature fatigue lives were actually longer than the room temperature fatigue lives. This behavior was caused by the increased ductility of the fiber-matrix reaction zone, which in turn delayed the onset of the matrix cracking which dominated this portion of the SN curve.

Several milestones were overcome just to perform the tension-compression fatigue tests, and thus are significant contributions to future of tension-compression testing:

137

- A dogbone specimen was designed which successfully failed in the gauge length.

- A buckling guide was designed for use in tension-compression fatigue which successfully prevented excessive buckling while also allowing the specimen to strain in an unrestricted manner. Although several buckling guide designs have been used successfully in monotonic tension, the AFIT Buckling Guide is the first of its type to be used in fatigue testing.

In addition to the tension-compression test results, the tension-tension results are also contributions to the published fatigue data. Most existing tension-tension fatigue data for the $[0/90]_{2s}$ laminate consists of fatigue lives only up to 40,000 cycles. However, structural design with this material will require a complete understanding of fatigue lives well in excess of this amount. The current research extended the tension-tension SN curve from 40,000 to nearly 2 million cycles.

Although this work has made significant contributions to the understanding of the behavior of the material under tension-compression fatigue both at room and high temperatures, it is only a small piece of a much larger picture. Much testing will be required to attain a complete characterization of this material system in fatigue loading conditions. For instance, to completely understand the effect of the R-ratio on the fatigue response of MMCs, it will require extensive testing at many different R-ratios. Additionally, the effect of elevated temperature of 427° C has been found to extend the tension-compression fatigue lives in the intermediate stress ranges; will this occur in tension-tension fatigue? If so, at what temperature will this effect stop? These and many other questions must be answered before MMCs can be fully utilized.

Appendix A: Euler Buckling Analysis

The critical Euler Buckling load is defined as:

$$P_{cr} = \frac{n^2 \cdot \pi^2 \cdot E \cdot I}{L^2}$$

where: $I(w,t) = \frac{w \cdot t^3}{12}$

$w = 1.27$ cm

$t = 0.1778$ cm

$n = 4$ (fixed-fixed boundary condition)

$E = 122$ GPa

Thus, the critical buckling length, to be compared to the specimen gage length, is:

$$L_{cr}(w,t) = \sqrt{\frac{n^2 \cdot \pi^2 \cdot E \cdot I(w,t)}{P_{cr}}}$$

This critical buckling length at various applied stresses is plotted below:
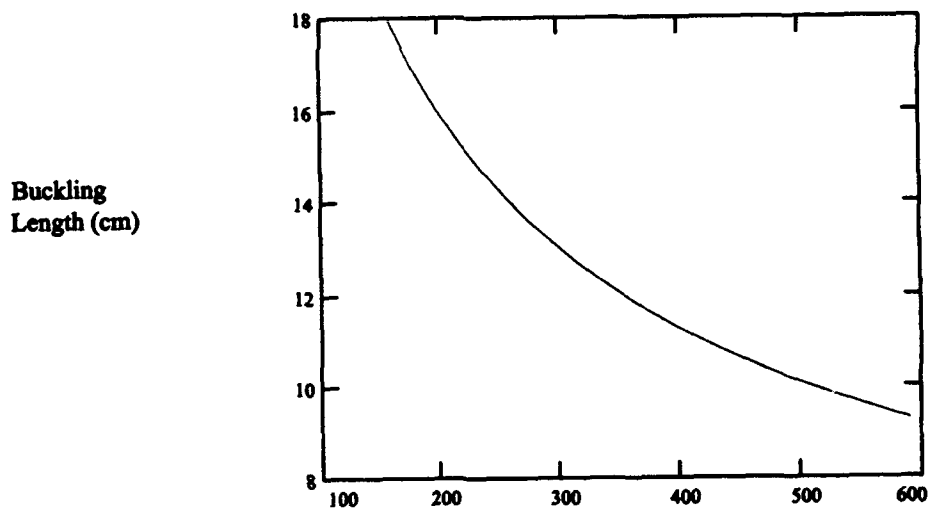
Buckling Length (cm) vs. Applied Stress (MPa)

The 2.54 cm (one inch) gage length used for the RT testing is well below the critical buckling length in all cases.

139

R= Radius of Curvature in mm:

$$b(m) = \left(a^2 + m^2\right)^{.5}$$

$$R(a,m) = \frac{\frac{b(m)}{2}}{\sin\left(\operatorname{atan}\left(\frac{a}{m}\right)\right)}$$

wg = reduced width

— wg = 5.08 mm (0.2")
· · wg = 7.62 mm (0.30")
— wg = 9.9 mm (0.39")
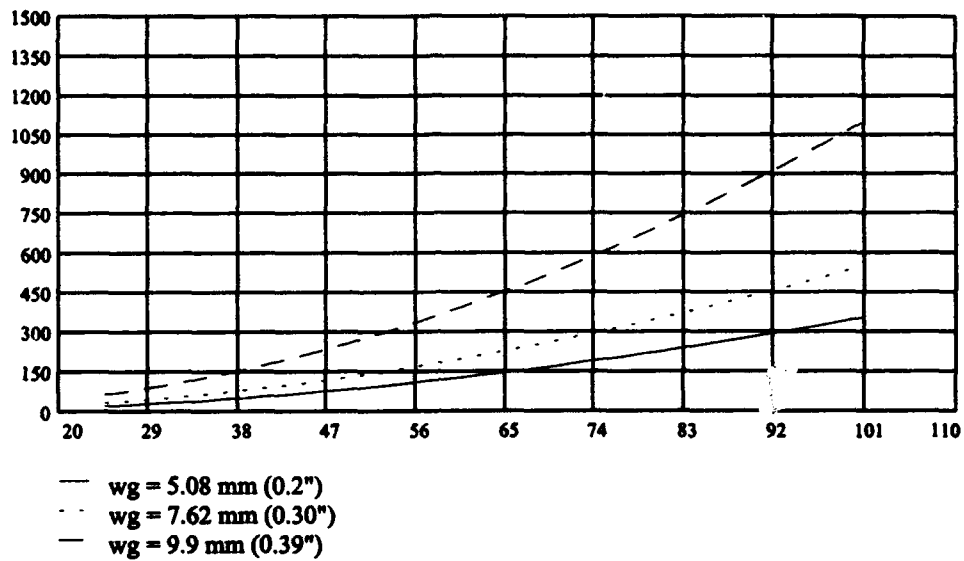
Shoulder Radius (mm) vs. Gage Length Between Grips (mm)

A reduced width of 5.08 mm (0.2") was chosen for the dogbone specimen which had 101.6 mm (4") between the grips:
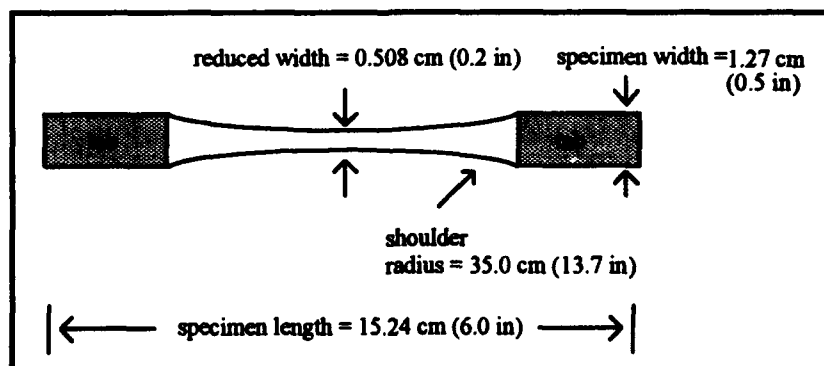
reduced width = 0.508 cm (0.2 in)   specimen width =1.27 cm (0.5 in)

shoulder
radius = 35.0 cm (13.7 in)

specimen length = 15.24 cm (6.0 in)

Room Temperature DATABANK.DAT File

```
SCS6   SILICON CARBIDE FIBER.   AUG 1993.
FP      1 0.551E-02 0.110E+00 0.487E+04
FE   0.573E+08 0.573E+08 0.250E+00 0.250E+00 0.238E+08 0.238E+08
FT   0.270E-05 0.270E-05 0.750E+00 0.750E+00 0.290E+00
FS   0.500E+06 0.650E+06 0.500E+06 0.650E+06 0.300E+06 0.300E+06
SIGF0       0.0         0.0         0.0         0.0         0.0         0.0     0.0
DOTF0       0.0         0.0         0.0         0.0         0.0         0.0     0.0
EXPONENTS +0.00 +0.00 +0.00 +0.00 +0.00 +0.00 +0.00 +0.00 +0.00 +0.00
EXPONENTS +0.00 +0.00 +0.00 +0.00 +0.00 +0.00 +0.00 +0.00 +0.00 +0.00
EXPONENTS +0.00 +0.00 +0.00 +0.00 +0.00 +0.00 +0.00 +0.00 +0.00 +0.00
EXPONENTS +0.00

TI15  TITANIUM MATRIX. AUG 1993.
MP  0.172E 00
ME  0.133E 08 0.360E 00 0.540E-05
MT  0.390E 00 0.120E 00
MS  0.130E 06 0.130E 06 0.910E 05 0.120E 00 0.120E 00 0.120E 00 0.120E 00
MV  0.019E 00 0.300E 04
SIGM0       0.0         0.0         0.0         0.0         0.0         0.0     0.0
SIGM0       0.0         0.0         0.0         0.0         0.0         0.0     0.0
SIGM0       0.0         0.0         0.0         0.0         0.0
DOTM0       0.0         0.0         0.0         0.0         0.0         0.0     0.0
DOTM0       0.0         0.0         0.0         0.0         0.0         0.0     0.0
DOTM0       0.0         0.0         0.0         0.0         0.0
EXPONENTS +0.00 +0.00 +0.00 +0.00 +0.00 +0.00 +0.00 +0.00 +0.00 +0.00
EXPONENTS +0.00 +0.00 +0.00 +0.00 +0.00 +0.00 +0.00 +0.00 +0.17 +0.00
EXPONENTS +0.00 +0.00 +0.00 +0.00 +0.00 +0.00 +0.00 +0.00 +0.00 +0.00
EXPONENTS +0.00
```

High Temperature DATABANK.DAT File

```
SCS6   SILICON CARBIDE FIBER.   AUG 1993.
FP      1 0.551E-02 0.110E+00 0.487E+04
FE   0.573E+08   573E+08 0.250E+00 0.250E+00 0.238E+08 0.238E+08
FT   0.270E-05 0.270E-05 0.750E+00 0.750E+00 0.290E+00
FS   0.500E+06 0.650E+06 0.500E+06 0.650E+06 0.300E+06 0.300E+06
SIGF0       0.0         0.0         0.0         0.0         0.0         0.0     0.0
DOTF0       0.0         0.0         0.0         0.0         0.0         0.0     0.0
EXPONENTS +0.00 +0.00 +0.00 +0.00 +0.00 +0.00 +0.00 +0.00 +0.00 +0.00
EXPONENTS +0.00 +0.00 +0.00 +0.00 +0.00 +0.00 +0.00 +0.00 +0.00 +0.00
EXPONENTS +0.00 +0.00 +0.00 +0.00 +0.00 +0.00 +0.00 +0.00 +0.00 +0.00
EXPONENTS +0.00

TI15  TITANIUM MATRIX. AUG 1993.
MP  0.172E 00
ME  0.109E 08 0.360E 00 0.540E-05
MT  0.390E 00 0.120E 00
MS  0.130E 06 0.130E 06 0.910E 05 0.120E 00 0.120E 00 0.120E 00 0.120E 00
MV  0.019E 00 0.300E 04
SIGM0       0.0         0.0         0.0         0.0         0.0         0.0     0.0
SIGM0       0.0         0.0         0.0         0.0         0.0         0.0     0.0
SIGM0       0.0         0.0         0.0         0.0         0.0
DOTM0       0.0         0.0         0.0         0.0         0.0         0.0     0.0
DOTM0       0.0         0.0         0.0         0.0         0.0         0.0     0.0
DOTM0       0.0         0.0         0.0         0.0         0.0
EXPONENTS +0.00 +0.00 +0.00 +0.00 +0.00 +0.00 +0.00 +0.00 +0.00 +0.00
EXPONENTS +0.00 +0.00 +0.00 +0.00 +0.00 +0.00 +0.00 +0.00 +0.17 +0.00
```

Sample TC HT Input File

```
SAMPLE INPUT DATA FOR METCAN, TENSION-COMPRESSION FATIGUE LOAD = 600 MPA
$ Note that all data is in English units: dimensions are in inches,
$  stresses are in ksi.  For further info, see user's manual.
$  No postprocessing file requested
$  Isothermal Loading
    POST        F
   LDDIST       F
$  Ply configuration details
      PLY       1       1   .0    0.00875
      PLY       2       1 90.0    0.00875
      PLY       3       1   .0    0.00875
      PLY       4       1 90.0    0.00875
      PLY       5       1 90.0    0.00875
      PLY       6       1   .0    0.00875
      PLY       7       1 90.0    0.00875
      PLY       8       1   .0    0.00875
$  Material Details found in DATABANK.DAT file
   MATCRD       1   .350     .0   SCS6TI15
$  No cyclic degradation effects
   CYCLES   .1E+01      1.
$  Output requests
      PRINT   MICRO  Output request for current microstresses    (Option 28)
      PRINT   LDSTEP Output request for load step details        (Option 29)
PRINTOPT      ALL
$ Note that "PRINTOPT" card is optional; Default is full print report
$  Interface details
INTRFACE          0    .05
$
$  Simplified Table Input;  NSEG = -5
   TMLOAD       -5
$ The first load step is merely the manufacturing cool down from 815 C,
$   or 1499 F, to room temperature of 75 F.  The first two numbers represent
$   the start time, end time, and the number of increments
    0.0 10800.         1
$ Process temperature
   1499.   1499.   1499.  1499.   1499.    1499.   1499.   1499.
$ Room temperature
   75.      75.     75.    75.     75.      75.     75.     75.
$ No mechanical loads
    0.0     0.0     0.0    0.0     0.0      0.0     0.0     0.0
    0.0     0.0     0.0    0.0     0.0      0.0     0.0     0.0
$ Second Load step: heat to testing temperature, no mechanical load
  10800.  14400.         1
   75.      75.     75.    75.     75.      75.     75.     75.
  800.     800.    800.   800.    800.     800.    800.    800.
    0.0     0.0     0.0    0.0     0.0      0.0     0.0     0.0
    0.0     0.0     0.0    0.0     0.0      0.0     0.0     0.0
$ Third Load step: apply full tension load, note that the load is Nx,
$   which is the (stress x laminate thickness), units = lb/in
  14400.  14800.         1
   800.    800.    800.   800.    800.     800.     800.    800.
   800.    800.    800.   800.    800.     800.     800.    800.
    0.      0.      0.     0.0     0.0      0.0      0.0     0.0
  6091.     0.      0.     0.0     0.0      0.0      0.0     0.0
$ Fourth Load step: apply full compression load
  14800.  15200.         1
   800.    800.    800.   800.    800.     800.     800.    800.
   800.    800.    800.   800.    800.     800.     800.    800.
  6091.     0.      0.     0.0     0.0      0.0      0.0     0.0
 -6091.     0.      0.     0.0     0.0      0.0      0.0     0.0
$  Fifth Load step: bring load back to zero
  15200.  15600.         1
   800.    800.    800.   800.    800.     800.     800.    800.
   800.    800.    800.   800.    800.     800.     800.    800.
 -6091.     0.      0.     0.0     0.0      0.0      0.0     0.0
    0.0     0.0     0.0    0.0     0.0      0.0      0.0     0.0
```

142

Sample TC RT Input File

```
SAMPLE INPUT DATA FOR METCAN, TC RT, Stress = 600 MPa
$  No postprocessing file requested
    POST        F
  LDDIST        F
$  Ply configuration details
    PLY         1       1    .0    0.00875
    PLY         2       1  90.0    0.00875
    PLY         3       1    .0    0.00875
    PLY         4       1  90.0    0.00875
    PLY         5       1  90.0    0.00875
    PLY         6       1    .0    0.00875
    PLY         7       1  90.0    0.00875
    PLY         8       1    .0    0.00875
$  Material Details
  MATCRD        1   .350     .0    SCS6TI15
$  No cyclic degradation effects
  CYCLES  .1E+01      1.
$  Output requests
    PRINT   MICRO  Output request for current microstresses   (Option 28)
    PRINT   LDSTEP Output request for load step details       (Option 29)
PRINTOPT      ALL
$  Interface details
INTRFACE        0    .05
$  Simplified Table Input;  NSEG = -4
  TMLOAD       -4
    0.0 10800.          1
   1499.   1499.   1499.  1499.  1499.  1499.  1499.  1499.
    75.     75.     75.    75.    75.    75.    75.    75.
    0.0     0.0     0.0    0.0    0.0    0.0    0.0    0.0
    0.0     0.0     0.0    0.0    0.0    0.0    0.0    0.0
 10800.  14400.          1
    75.     75.     75.    75.    75.    75.    75.    75.
    75.     75.     75.    75.    75.    75.    75.    75.
    0.      0.      0.     0.0    0.0    0.0    0.0    0.0
  6091.     0.      0.     0.0    0.0    0.0    0.0    0.0
 14400.  14800.          1
    75.     75.     75.    75.    75.    75.    75.    75.
    75.     75.     75.    75.    75.    75.    75.    75.
  6091.     0.      0.     0.0    0.0    0.0    0.0    0.0
 -6091.     0.      0.     0.0    0.0    0.0    0.0    0.0
 14800.  15200.          1
    75.     75.     75.    75.    75.    75.    75.    75.
    75.     75.     75.    75.    75.    75.    75.    75.
 -6091.     0.      0.     0.0    0.0    0.0    0.0    0.0
    0.0     0.0     0.0    0.0    0.0    0.0    0.0    0.0
```

Sample TC RT Input File

```
SAMPLE INPUT DATA FOR METCAN, TT RT, Stress = 600 MPa
$  No postprocessing file requested
     POST       F
   LDDIST       F
$  Ply configuration details
     PLY        1      1    .0   0.00875
     PLY        2      1  90.0   0.00875
     PLY        3      1    .0   0.00875
     PLY        4      1  90.0   0.00875
     PLY        5      1  90.0   0.00875
     PLY        6      1    .0   0.00875
     PLY        7      1  90.0   0.00875
     PLY        8      1    .0   0.00875
$  Material Details
   MATCRD        1   .350     .0   SCS6TI15
$  No cyclic degradation effects
   CYCLES  .1E+01       1.
$  Output requests
   PRINT    MICRO  Output request for current microstresses   (Option 28)
   PRINT    LDSTEP Output request for load step details       (Option 29)
PRINTOPT     ALL
$  Interface details
INTRFACE        0   .05
$  Simplified Table Input;  NSEG = 2
   TMLOAD      -6
     0.0 10800.        1
   1499.    1499.    1499.   1499.   1499.   1499.   1499.   1499.
     75.      75.      75.     75.     75.     75.     75.     75.
     0.0
     0.0
   10800.  10840.        1
     75.      75.      75.     75.     75.     75.     75.     75.
     75.      75.      75.     75.     75.     75.     75.     75.
      0.      0.       0.      0.0     0.0     0.0     0.0     0.0
    609.      0.       0.      0.0     0.0     0.0     0.0     0.0
   10840.  11200.        1
     75.      75.      75.     75.     75.     75.     75.     75.
     75.      75.      75.     75.     75.     75.     75.     75.
    609.      0.       0.      0.0     0.0     0.0     0.0     0.0
   6091.      0.       0.      0.0     0.0     0.0     0.0     0.0
   11200.  11560.        1
     75.      75.      75.     75.     75.     75.     75.     75.
     75.      75.      75.     75.     75.     75.     75.     75.
   6091.      0.       0.      0.0     0.0     0.0     0.0     0.0
    609.0     0.0      0.0     0.0     0.0     0.0     0.0     0.0
   11560.  11920.        1
     75.      75.      75.     75.     75.     75.     75.     75.
     75.      75.      75.     75.     75.     75.     75.     75.
    609.      0.       0.      0.0     0.0     0.0     0.0     0.0
   6091.0     0.0      0.0     0.0     0.0     0.0     0.0     0.0
   11920.  12280.        1
     75.      75.      75.     75.     75.     75.     75.     75.
     75.      75.      75.     75.     75.     75.     75.     75.
   6091.      0.       0.      0.0     0.0     0.0     0.0     0.0
    609.0     0.0      0.0     0.0     0.0     0.0     0.0     0.0
```

Bibliography

1. Adams, Donald F. "Test Methods for Composite Materials," Seminar Notes, Composite Materials Research Group, University of Wyoming. Lancaster: Technomic Publishing Company, March 1991.

2. Agarwal, Bhagwan D., and Lawrence J. Broutman. *Analysis and Performance of Fiber Composites*. New York: John Wiley & Sons, Inc., 1990.

3. Amateau, M.F, et al, *Mechanical Behavior, Proceedings of the International Conference on Mechanical Behavior of Materials, Vol. 2*, Society of Materials Science, Japan, 1972.

4. Baker, Capt Robert P. *Investigation of Fatigue Behavior in Notched Cross-Ply Titanium Metal Matrix Composite at Elevated Temperature*. MS Thesis, AFIT/GAE/ENY/92D-03. School of Engineering, Air Force Institute of Technology (AU), Wright-Patterson AFB OH, December 1992.

5. Bania, P.J., G. A. Lenning, and J. A. Hall. "Development and Properties of Ti-15V-3Cr-3Sn-3Al (Ti 15-3)," β-Titanium Alloys in the '80s, Boyer R.R., and Rosenberg, H.W., Eds. A publication of the Metalluricacal Society of AIME, 1984, pp 209-229.

6. Bannantine, Julie A. and others. *Fundamentals of Metal Fatigue Analysis*. New Jersey: Prentice Hall, 1990.

7. Boyer, R. R., W. J. Porter, E. R. Barta and D. Eylon. "Microstructure/Properties Relationships in Ti-15V-3Cr-3Al-3Sn High Strength Castings," The Minerals, Metals and Materials Society, 1991.

8. Broek, David. *Elementary Engineering Fracture Mechanics, Fourth Revised Edition*. Dordrecht: Kluwer Academic Press, 1991.

9. Chestnutt, C. G., et al, ASTM STP 600, 1976.

10. Cooke, C. M., John T. Cammett, Daniel Eylon, and Paul R. Smith. "Edge Preparation of Titanium Matrix Composite Specimens for Mechanical Testing," Microstructural Science, Volume 10, Elsevier Science Publishing Co., 1982.

11. Davidson, David L., "Fatigue Crack Growth Mechanisms and Mechanics in Metallic and Intermetallic Alloys and Partially Stabilized Zirconia," Presented at the Engineering Foundation International Conference, Santa Barbara, California, January 13-18, 1991.

12. Forsyth, P. J. E. *The Physical Basis of Metal Fatigue*. New York: American Elsevier Publishing Company, Inc., 1969.

13. Fuchs, Henry O. *Metal Fatigue in Engineering*. New York: John Wiley and Sons, 1980.

14. Gadya, John, and Timothy P. Gabb. "Effect of Heating Mode and Specimen Geometry on Fatigue Properties of a Metal Matrix Composite," NASA Conference Publication 1051, HITEMP Review, October, 1990, pp 31-1-8.

15. Gayda, John, and Timothy P. Gabb, "Isothermal Fatigue Behavior of a $[90]_8$ SiC/Ti-15-3 Composite at 426°C," NASA Technical Memorandum 103686, January 1991.

16. Hertzberg, Richard W. *Deformation and Fracture Mechanics of Engineering Materials*. New York: John Wiley & Sons, 1976.

17. Hopkins, Dale A., and Christos C. Chamis, "A unique set of Micromechanics Equations for High Temperature Metal Matrix Composites." NASA TM-87154, November 1985.

18. Hopkins, Dale A., and D.L. Murthey. *User's Guide for Metal Matrix Composite Analyzer* (ver. 3). NASA Lewis Research Center, 1991.

19. Hudson, C. Michael and Thomas P. Rich. *Case Histories Involving Fatigue and Fracture Mechanics*. Philadelphia: ASTM Publications: 1985.

20. Irving, P.E., and C.J. Beevers, *Materials Science and Engineering*, 14, 1974.

21. Johnson, W.S., "Fatigue Testing and Damage Development in Continuous Fiber Reinforced Metal Matrix Composites," *Metal Matrix Composites: Testing, Analysis, and Failure Modes, ASTM STP 1032*, W. S. Johnson, Ed., American Society for Testing and Materials, Philadelphia, 1989, pp. 194-221.

22. Johnson, W.S., Lubowinski, S.J, and Highsmith, A.L., "Mechanical Characterization of Unnotched SCS_6/Ti-15-3 Metal Matrix Composites at Room Temperature," *Thermal and Mechanical Behavior of Metal Matrix and Ceramic Matrix Composites, ASTM STP 1080*, J.M. Kennedy, H.H. Moeller, and W.S. Johnson, Eds., American Society for Testing and Materials, Philadelphia, 1990, pp. 193-218

23. Kantzos, Peter, Jack Telesman, and Louis Ghosn, "Fatigue Crack Growth in a Unidirectional SCS_6/Ti-15-3 Composite," *Composite Materials: Fatiuge and Fracture (Third Volume), ASTM STP 1110*, T.K. O'Brien, Ed., American Society for Testing and Materials, Philadelphia, 1991, pp. 711-731.

24. Lerch, Bradley A., "Fatigue Behavior of SiC/Ti-15-3 Laminates," NASA Conference Publication 1051, HITEMP Review, October, 1990, pp 35-1-8.

25. Lerch, Bradley A., "Matrix Plasticity in SiC/Ti-15-3 Composite" NASA TM 103760, July 1991.

26. Lerch, Bradley A., and Gary R. Halford. "Fully Reversed Fatigue of a Ti-MMC," Conference Proceedings of the 17th Annual Conference on Composites, Materials, and Structures (Restricted Sessions), January 1993.

27. Lerch, Bradley A., and James F. Saltsman. "Tensile Deformation and Damage in SiC Reinforced Ti-15V-3Cr-3Al-3Sn," NASA TM 103620. NASA Lewis Research Center, 1990.

28. Majumdar, Bhaskar. S. and Golam M. Newaz. Inelastic Deformation of Metal Matrix Composites: Plasticity and Damage Mechanisms, Part I and II, NASA Contractor Report 189096, December 1992.

29. Majumdar, Bhaskar S., and Golam M. Newaz. "Inelastic Deformation of Metal Matrix Composites: Compression and Fatigue," Submitted for publication. Battelle Memorial Institute, Columbus, Ohio 43201.

30. Majumdar, Bhaskar S., and Bradley A. Lerch. "Fatigue Mechanisms in a Ti-Based Fiber-Reinforced MMC and Approaches to Life Prediction." Submitted to Titanium Matrix Composites Workshop, La Jolla, California, June 1993.

31. Majumdar, Bhaskar S., and Golam M. Newaz. "Mechanisms of Fatigue Damage and Failure of a SCS_6/Ti-15-3 Composite." ASM/TMS Proceedings of Mechanisms and Mechanics of a Composite Fracture," Pittsburgh, PA, October 1993.

32. Majumdar, Bhaskar S., and Golam M. Newaz. "Isothermal Fatigue Mechanisms in Ti-Based Metal Matrix Composites" Final Report to NASA Lewis Research Center HITEMP Office, Contract Number NAS3-26494, April 1993.

33. Majumdar, Bhaskar S., and Golam M. Newaz. "Inelastic Deformation of MMCs: Thermo-Mechanical Fatigue (TMF)," Submitted for Publication.

34. Mall, Shankar M., and Barry Portner. "Characterization of Fatigue Behavior in Cross-Ply Laminate of SCS-6/Ti-15-3 Metal Matrix Composite at Elevated Temperature" Submitted for publication in Journal of Engineering Materials and Technology, Air Force Institute of Technology, Wright-Patterson AFB OH, 1991.

35. Mall, Shankar M., and D.G. Hanson. "Thermomechanical Fatigue Behavior of a Cross-Ply SCS-6/β21-s Metal Matrix Composite," MD-Volume 40, Constitutive Behavior of High-Temperature Composites, ASME 1992.

36. Mittnick, M. A., and J. McElman, "Continuouis Silicon Carbide Fiber Reinforced Metal Matrix Composites," Proceedings of 3rd Technical Conference on Composite Materials at Seattle, WA, September 26-29, 1988, pp. 395-403.

37. Newaz, G. M., and B. S. Majumdar. "A Comparison of Mechanical Response of MMC At Room and Elevated Temperatures," Submitted for publication. Battelle Memorial Institute, Columbus, Ohio 43201.

38. Paris, P. C. "Fatigue - An Interdisciplinary Approach," Proceedings 10th Sagamore Conference, Syracuse University Press, Syracuse, N.Y., 1964.

39. Pollock, W. C., and W. Steven Johnson, "Characterization of Unnotched SCS-6/Ti-15-3 Metal Matrix Composites at 650° C," NASA Technical Memorandum 102699, September 1990.

40. Portner, Barry D. *Investigation of Fatigue Damage Mechanisms in a Metal Matrix Composite Under Elevated Temperature*. MS Thesis, AFIT/GAE/ENY/90D-20. School of Engineering, Air Force Institute of Technology (AU), Wright-Patterson AFB OH, December 1990.

41. Robinson, J.L., and C.J. Beevers, 2nd International Conference on Titanium, Cambridge, England, 1972.

42. Rosenberg, H. W. "Ti-15-3: A New Cold-Formable Sheet Titanium Alloy,"*Journal of Metals*, Vol. 35, No. 11, November 1983, pp 30-34.

43. Rotam, A., and H. G. Nelson. "Failure of a Laminated Composite Under Tension-Compression Fatigue Loading." Composites Scienc and Technology, 1989.

44. Sanders, Brian. Characterization of Fatiuge Damage in a Metal Matrix Composite (SCS-6/Ti-15-3) at Elevated Temperature. Doctoral Dissertation, AFIT/DS/ENY/92J. School of Engineering, Air Force Institute of Technology (AU), Wright-Patterson AFB OH, January 1992.

45. Santhosh, U., Ahmad, J., and Nagar, A., "Non-Linear Micromechanics Analysis Prediction of the Behavior of Titanium Alloy Matrix Composites," *Fracture and Damage*, ASME, Vol 27, 1992.

46. Skelton, R. P. *Fatigue at High Temperature*. London: Applied Science Publishers, 1983.

47. Smith, William F. *Principles of Materials Science and Engineering*. New York: McGraw-Hill Publishing Company, 1990.

48. Suresh, S. *Fatigue of Materials*. Cambridge: Cambridge University Press, 1991.

49. Talreja, Ramesh. *Fatigue of Composite Materials*. Lancaster: Technomic Publishing Company, 1987.

50. Taya, Minoru and Richard J. Arsenault. *Metal Matrix Composites: Thermomechanical Behavior.* Oxford: Pergamon Press, 1989.

51. Verrilli, Michael J., and Timothy P.Gabb. "High Temperature TC Fatigue Behavior of a Tungsten Copper Composite," Fourth Symposium on Composite Materials: Fatigue and Fracture, ASTM Conference Proceedings, March 1991.

52. Wagner, I., G. Lutijenig, and R. I. Jaffee. "Optimization of Bi-Modal Microstructure and Texture in Ti-6Al-4V," The Minerals, Metals and Materials Society, 1991.

53. Wiebull, W. *Fatigue Testing and the Analysis of Results.* New York: Pergamon Press, 1961.

54. Worthem, Dennis W. "Flat Tensile Specimen Design for Advanced Composites." NASA Contractor Report 185261, November, 1990.

55. Yuen, A, S. et al, *Met. Trans.,* 5, 1974.

Captain Elizabeth A. Boyum was born 19 July 1967 at Columbus AFB, Mississippi. She graduated from SHAPE American High School, in Mons, Belgium, in 1985. That summer she entered the United States Air Force Academy where she majored in Engineering Mechanics. Upon her graduation from USAFA in May, 1989, she began her first assignment as a structural engineer in the Armament Directorate at Eglin AFB, Florida. During her time there, she was involved in air-to-ground missile airframe design, analysis, and flight testing. Following her assignment at Eglin, she entered the Air Force Institute of Technology School of Engineering in May 1992.

Permanent Address: 105 Southfork Way
                                     Folsom, CA 95630

REPORT DOCUMENTATION PAGE

1. AGENCY USE ONLY (leave blank)	2. REPORT DATE December 1993	3. REPORT TYPE AND DATES COVERED Master's Thesis

4. TITLE AND SUBTITLE INVESTIGATION OF TENSION-COMPRESSION FATIGUE BEHAVIOR OF A CROSS-PLY METAL MATRIX COMPOSITE AT ROOM AND ELEVATED TEMPERATURES	5. FUNDING NUMBERS
6. AUTHOR(S) Elizabeth A. Boyum, Captain, USAF	

7. PERFORMING ORGANIZATION NAME(S) AND ADDRESS(ES) Air Force Institute of Technology, WPAFB, OH 45433	8. PERFORMING ORGANIZATION REPORT NUMBER AFIT/GAE/ENY/93D-6

9. SPONSORING / MONITORING AGENCY NAME(S) AND ADDRESS(ES) Mr. Ted Fecke WRDC/POTC Wright-Patterson AFB OH, 45433	10. SPONSORING / MONITORING AGENCY REPORT NUMBER

11. SUPPLEMENTARY NOTES

12a. DISTRIBUTION / AVAILABILITY STATEMENT Approved for public release; distribution unlimited	12b. DISTRIBUTION CODE

13. ABSTRACT (Maximum 200 words)

This research, the first load-controlled tension-compression fatigue testing to be performed on a MMC, extends the existing knowledge of MMC fatigue damage mechanisms to include the tension-compression loading condition. To accomplish this, a $[0/90]_{2s}$ SCS-6/Ti-15-3 laminate was subjected to tension-tension fatigue at room temperature, and tension-compression fatigue at both room temperature and 427°C. Stress and strain data was taken to evaluate the macro-mechanic behavior of the material. Microscopy and fractography were performed to characterize the damage on a micro-mechanic level. On a maximum applied stress basis, the room temperature tension-tension specimens had longer fatigue lives than the room temperature tension-compression specimens. The room and high temperature tension-compression fatigue lives were nearly identical in the fiber-dominated high stress region of the SN curve. However, the increased ductility and diffused plasticity of the titanium matrix at 427°C delayed the onset and severity of matrix cracking, and thus increased the elevated temperature fatigue lives in the matrix dominated region of the SN curve. In all cases, matrix damage initiated at reaction zone cracks which nucleated both matrix plasticity and matrix cracking.

14. SUBJECT TERMS Metal Matrix Composite, Elevated Temperature, Fatigue Testing, Compression, Fully-reversed, Titanium, Silicon Carbide			15. NUMBER OF PAGES 164
			16. PRICE CODE

17. SECURITY CLASSIFICATION OF REPORT Unclassified	18. SECURITY CLASSIFICATION OF THIS PAGE Unclassified	19. SECURITY CLASSIFICATION OF ABSTRACT Unclassified	20. LIMITATION OF ABSTRACT UL